Modeling and Simulation of Frost Damage of Concrete and its Combined Effect with Fatigue Loadings

コンクリートの凍害および凍害-疲労複合劣化モデルとシミュレーション

By

Fuyuan GONG

A thesis submitted in partial fulfilment of the requirements for the degree of Doctor of Philosophy in Engineering

Professor Tamon UEDA

Supervisor

English Engineering Program (e3)
Laboratory of Engineering for Maintenance Systems
Division of Engineering and Policy for Sustainable Environment
Graduate School of Engineering
Hokkaido University
Sapporo, Japan
September 2015

ACKNOLEDGEMENT

First and foremost, I would like to express my sincerest thanks and gratitude to my supervisor, Professor Ueda Tamon, for the continued support, guidance and suggestions during my doctor's study. Thank you for all the valuable lessons and technical knowledge you have taught me. You have not only been the advisor, but also mentor and friend to me. Your mentorship was and will be paramount in providing a well-rounded experience for both the academic part of my career and other aspect of my life.

I would like to express my thanks to Mrs. Werawan Manakul, the ex-program coordinator of the English Engineering Program for all the help and support to my study and life in Hokkaido University, so that I can fully concentrate on my study and research work.

I would also like to extend my sincere thanks to our research team especially to Prof. Zhang Dawei who extended his knowledge and valuable time in spite of the long distance. Thanks to Wang Yi and Wang Zhao and my senior Evdon Sicat who have been helpful and enthusiastic partners in our research. In addition, I would give my appreciations to Dr. Yasuhiko Sato and Dr. Hitoshi Furuuchi and all the members in this laboratory for their good cooperation and assistance on my study and living here.

Many thanks also goes to my examination committee members, Prof. Takufumi Sugiyama and Prof. Takashi Matsumoto for their vital comments and questions which further enhance the content of the study. Sincere appreciations are extended to Prof. Toyoharu Nawa and Prof. Hiroshi Yokota for their helpful discussions and suggestions.

Special thanks are given to my wife. The encouragement, patience, support and unconditional love by her made me through the hard time. I also thank our parents, for their faith in me and unending encouragement and support to me.

ABSTRACT

Frost damage mechanism under freezing and thawing cycles (FTC) is an important issue for service life evaluation of concrete structures in cold regions. Once frost damage happens, deterioration process like chloride ion, carbon dioxide migration and even the frost action itself will be largely accelerated, result in shorter service life. In addition, the frost damage is always coupled with external loads, and the combined effect will also affect the material degradation and structure performance significantly. The frost damage is thought caused by the internal pore pressures generated during FTC, which includes both physical cycles and mechanical cycles. While for external loading like fatigue, it can be simply regarded as the mechanical cycles. Although the two effects have different natures, the damage of both can be reflected by the micro cracks initiating and propagating, which will finally result in the increasing residual deformation and reduction in stiffness, strength and so on. Therefore, it is possible to model and simulate the combined effects together. In order to simulate the frost damage mechanism and the combined effect, the following steps have been conducted: (1) the thermodynamic model of moisture in pores, which tells the phase equilibrium and amount of ice formation; (2) the pore pressure model, which can quantitatively explain the material deformation during FTC under different environmental conditions; (3) the mesoscale model and simulation of pure FTC damage, which includes the mechanical interaction between the porous body and the ice-water system; (4) the macroscale mechanical property change due to ice strengthening effect at low temperatures; (5) the simulation of the combined FTC and mechanical loading.

For the moisture condition in the pores of concrete material, the phase diagram is a useful tool in physics to show the form of water and phase equilibrium. By adding the pore radius to the traditional phase diagram, a three-dimensional phase diagram for pore water can be obtained. The shift of triple point and the phase boundaries can be quantitatively adjusted according to pore radius based on thermodynamic analysis. Therefore, a clearer image of moisture in pores can be shown, which could be a convenient tool to get the overall moisture condition inside the material. As a practical application, the 3D phase diagram is used to determine the ice content at low temperatures.

Once ice forms in highly saturated concrete material, internal tensile stress will be generated and causes damage to the material. On one hand, each component (porous body, ice and liquid) should satisfy the compatibility of stress and strain, which has been discussed by the poromechanical theories. On the other hand, if some empty voids exist, the hydraulic pressure will release when liquid water escapes from the expanded area according to Darcy's law. Previous freeze-thaw tests on the saturated mortar with closed moisture condition showed a consistent tendency: as the number of freeze-thaw cycles (FTC) increases, the deformation changes from the expansion to the contraction. In order to make clear the physical and mechanical changes during this process, a more comprehensive hydraulic model is developed, which combines both the mechanisms mentioned above. The estimated strain behavior by this model is compared with experimental measurement, and also it has good potential and is more flexible to be applied to different cases such as different saturation degrees and cooling rates. The permeability change can be also considered in the proposed model as a reflection of frost damage level.

After achieving a more comprehensive internal pressure model, the mesoscale model using Rigid Body Spring Method (RBSM) is developed to simulate the deformation behaviors of concrete under FTC cycles. On one hand, the macroscopic material is divided into small rigid elements of mesoscale; on the other hand, the microscale internal pore pressures are regarded as average values in mesoscale based on poromechanical theories. The constitutive relation is also developed to reflect deformation

compatibility between porous body and ice-water system. The simulation results can show the internal cracking and residual deformation clearly, which are also found in a good agreement with previous experimental data.

Although the internal stresses generated during freeze-thaw process would cause serious damage and other durability problems to concrete structures, if just concerning the stage while the temperature is below 0°C, ice could reduce the stress concentration within the concrete by filling the capillary and gel pores and result in a significant increases in elastic modulus and strength, which is usually beneficial for concrete under external loads (either static or fatigue). In order to distinguish and simulate the strengthening effect induced by ice quantitatively, a theoretical model explaining the change of elastic properties has been developed based on the theories of multiphase composite media. The predicted elastic modulus is in a good agreement with experiment data.

The constitutive laws for the mortar and concrete under external fatigue loading is also developed based on RBSM, which is a simplification and modification of previous model. Finally different types of loading condition are simulated, which includes:

(1) Pure FTC deformation and damage. The mortar and mortar-aggregate interface are simulated under closed moisture condition with 30 cycles while the concrete is simulated under open moisture condition with 300 cycles. The simulation results can show the damage cumulating, permeability change due to damage, the deformation behavior (reversing from expansion to contraction in closed test while continuously increasing in open test), crack pattern and width and so on, which agree with the experimental data well.

(2) The static loading with ice strengthening effect at low temperatures. The ice strengthened elastic modulus from the multi-phase composite model is adopted in the RBSM simulation, and the compressive, uniaxial tensile and splitting tensile tests are simulated and compared with the strength change in experiments, which also show a satisfactory agreement.

(3) Pure fatigue test for mortar and concrete. The fatigue life by the simplified time-independent model is compared with the previous time-dependent model (in which the creep is also considered). And the fatigue simulation is extended from mortar to concrete which includes the effect of interface. The simulated concrete fatigue life matches previous experiments well.

(4) Fatigue test with different level of FTC damage. In which the FTC test (open moisture condition) is conducted first to obtain the internal micro cracking, then using the FTC damaged concrete, static test is simulated to obtain the residual strength while fatigue simulation is conducted to get the fatigue life. Both the residual strength and fatigue life show a significant reduction, which agree with experimental observations well.

Keywords: frost damage, ice content, hydraulic pressure, fatigue, combined effect, mesoscale simulation, RBSM

TABLE OF CONTENTS

CHAPTER 1

1. Introduction

1.1 Background

In cold regions, frost damage is a very common and serious deterioration problem for concrete structures. Frost damage is thought to be caused by the ice formation from the water inside the porous materials, like cement, mortar and concrete. The micro cracking caused by the frost action can reduce the strength and also the resistance to other deterioration factors, like chloride ion, carbon dioxide and frost action itself, starting from the surface (Fig. 1.1).

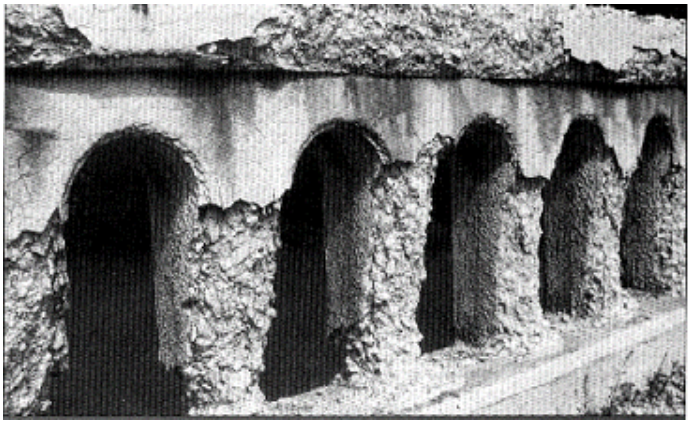

Fig. 1.1 Frost damage of the concrete structures

When the temperature falls down below the freezing point (usually lower than 0°C due to the super cooling effect (Gruebl, 1980)) of the porous water, ice initiates and cause tensile stress on the pore wall. This tensile stress is usually big enough to cause micro cracks inside the concrete materials. For the structures in the natural environment, the ice initiation usually starts from the surface of the concrete due to some nucleating germs like ice crystals, snow flacks, dust or the uneven parts of the surface (Kaufmann, 2002).

Fig. 1.2 Combined FTC damage and fatigue loading

In the real life, the concrete structures not only suffer the FTC damage, but the external loading is also always accompanied together, like the bridge deck and pavement. Due to FTC damage, the static strength of the material will be reduced significantly (Hasan et al., 2004), and also due to the micro

cracks induced by FTC, the crack initiation and propagation will be seriously accelerated and it will result in a significant reduction in the fatigue life (Hasan et al., 2008), such as the punching shear failure like Fig. 1.2.

Therefore, not only the pure FTC damage mechanism, but also the deterioration process under combined FTC and external loading are important to understand and predict the structure performance. Thus, after getting clear of the damage mechanism by each single effect, it will also be very beneficial to develop a numerical model which can simulate those effects under the same framework.

1.2 Statement of problems and objectives

Internal stress during FTC

Frost damage is an important issue for concrete structures, and has been studied for several decades. The deformation behavior and degradation of properties by frost action has been well studied at the material level. Kaufmann (2002) developed a qualitative sequential damage model, separating a freeze-thaw cycle into five phases and discussed in detail. Fagulund (2002) discussed the different effects between open and closed freeze-thaw tests (FTC test with open or closed moisture condition), and the effect of saturation degree. For the open test, the deformation measure by Hasan et al. (2004) up to 300 cycles showed a continually increasing behavior. This agrees with our common sense and can be explained easily by the existing models. However, recent closed tests up to 30 cycles by the authors showed different phenomenon: there was expansion during first few cycles, but converted to contraction as the number of cycle increased (Sicat et al, 2013). Although the damage of material would affect the measured deformation, this change of tendency can only be explained by the change of forces: from positive forces dominant to negative forces dominant. Thus, more comprehensive stress model is needed to explain this complex strain behavior.

The stress that causes frost damage is believed as the hydraulic pressure at the beginning. Powers (1949) developed the hydraulic pressure model based on Darcy's law, and according to that model, the maximum spacing factor of the entrained air can be determined so that the damage can be avoided. Recent studies discussed that, other than hydraulic pressure, the crystallization pressure is another mechanism (Scherer, 2005), because damage was observed even in partially saturated cases, in which the hydraulic pressure can be avoided. In addition, due to the thermodynamic equilibrium between three phases of moisture, there is always a cryosuction pressure in the unfrozen water. Sun and Scherer (2010a) also developed the mathematical way to calculate the overall stress and strain caused by crystallization and cryosuction pressures. Coussy and Monteiro's model (2008) was developed based on the poromechanics and was improved later (2009), which included hydraulic pressure and cryosuction. However, both Sun's and Coussy's models ignored the hydraulic flow and pressure release like Powers' model. Once the specimen is sealed, the internal forces are thought to be almost the same during each cycle. It is true for a few cycles because the permeability of cementitious materials is very small. But as the number of cycle increases, damage will accumulate and the liquid water can move more easily. Therefore, the pressure release should also be considered in this problem.

In this study, we will combine all the mechanisms mentioned above to obtain a more comprehensive, flexible but not too complex model to explain the measured strain behavior under closed FTC test. Crystallization pressure and cryosuction pressure are static pressures that only rely on the temperature and pore size distribution, while the hydraulic pressure is a dynamic pressure which depends on the permeability of the material. Previous studies have shown that there is no significant change in pore size distribution during the first few FTCs (Sun, 2010b), so it means the crystallization pressure and

cryosuction pressure are not responsible to this tendency change (expansion at the beginning but converted to contraction at last), and the main reason is the hydraulic pressure reduction due to the permeability increment caused by frost damage accumulation (Yang et al, 2006). The measured deformation in different cycles is used to verify the proposed model. And the application potential of this model is also discussed at last.

Mesoscale Simulation of FTC damage

After achieving a more flexible and comprehensive pressure model, the estimated internal forces will be introduced into Rigid Body Spring Model (RBSM), a discrete numerical model to simulate the deformation and damage (Kawai, 1977). Mesoscale analysis is relatively more precise to simulate each component (mortar, aggregate and their interfaces) in the concrete. In addition, this discrete model has advantages to show the cracking, which eventually causes failure. Previous researchers have used RBSM to simulate the concrete materials under static loads (Nagai et al, 2004; 2005), fatigue loads (Matsumoto et al, 2008) and also the mechanical properties of frost damaged concrete (Ueda et al, 2009). Due to its advantages in modeling of the cracks, the frost damage related durability problems such as moisture transport and chloride migration can be also simulated using RBSM (Wang et al, 2008). Frost damage also affects the resistance to other impacts like the mechanical loads and environmental impacts and may result in structural failure. Therefore, it is beneficial to develop a numerical model based on RBSM to simulate the degradation process of concrete under FTC.

In this study, based on the pore pressure model developed in the previous work, the constitutive laws for the concrete material (porous body) and the ice-water system will be developed, especially for the RBSM. And two types of experiments will be simulated and compared with test data; one is the mortar and mortar-aggregate interface in closed test up to 30 FTC and the other is the concrete cylinder in open test up to 300 FTC. Finally the results will be discussed in detail.

Ice strengthening effect under external loads

In the real life, the frost actions on the concrete structures are usually coupled with external mechanical loads, like the static load and fatigue load. If the saturation degree exceeds a critical value (Fagerlund, 2002), significant damage in the porous skeleton will occur due to several kinds of pore pressures (Powers, 1945; Scherer and Vallenza II, 2005; Coussy and Monteiro, 2008; Gong et al., 2015) during ice formation. This kind of internal damage will cumulated during large number of freeze-thaw cycles (FTCs) and result in gradually degradation in material properties (Hasan et al., 2004; Gong et al., 2013). As a result, for the concrete damaged by FTCs, the static strength and the fatigue life (testing at room temperature) under external mechanical loads will also be reduced (Ueda et al., 2009; Hasan et al., 2008). On the other hand, when ice fills up the pores at low temperature, the stress concentration can be reduced due to increased density and continuity of the porous material, thus result in higher elastic modulus and strength (Rostasy and Wiedemann, 1980; Lee et al., 1988a,b). The experiments under FTC and fatigue load simultaneously also shows a longer fatigue life compared to pure fatigue test in room temperature (Li et al., 2011), this may be also because that half of the fatigue life are during the freezing temperature, while the material is strengthened significantly by ice. Although there are some empirical equations describing the strengthening effect of ice (Okada and Iguro, 1978; Goto and Miura, 1979; Browne and Bamforth, 1981), a theoretical model is still absent. Thus, there are some practical meanings and necessity to establish a theoretical model which can be used to predict the strengthening effect under different conditions quantitatively.

The elastic modulus is an essential parameter for the analysis of concrete behavior strengthened by

ice, but there are few theories or models to predict the effective elastic modulus for concrete materials containing different phases of moisture. Yaman et al. (2002b) introduced several multi-phase composite models to predict the elastic moduli of dry and saturated concrete, and found them more effective than other meso-mechanical or semi-empirical methods. For the unsaturated concrete that composed by three phases (intrinsic concrete, water and dry pores), Wang and Li (2007) developed a decomposed method to change this three-phase problem into a two-stage equivalent problem, and each stage was based on Benveniste's (1987) two-phase composite theory. In this paper, similar but modified way of decomposition will be used based on Benveniste's model to predict the effective modulus of the concrete material with different amount of air, liquid water and ice.

The theoretical model can only predict the change of elastic constants due to ice formation, but it is difficult to show the change of strength directly. Therefore, a mesoscale discrete analysis is developed based on RBSM to simulate the strength and failure under static load (compression, uniaxial tension and splitting) with different environmental conditions. The loading process at freezing temperature is actually a coupled problem of internal freezing stress and external mechanical load, during which the crack initiation and propagation play an important role. Therefore, it is beneficial to develop a numerical model based on RBSM to simulate the concrete behavior under this combined effect.

In this study, based on the two-phase composite theory and the idea of decomposition, the theoretical model will be developed to predict the effective elastic modulus of concrete material containing different proportion of air, liquid water and ice, which is a general model that suitable for both concrete system and mortar system. Since in mesoscale analysis, the concrete is regarded composed by mortar, coarse aggregate and their interface, and the ice formation inside the coarse aggregate is negligible. Therefore the property change in mortar will be used as an input for RBSM analysis to simulate the strength of concrete. The constitutive laws for RBSM will also be developed accordingly for this combined problem. Finally, the predicted elastic modulus and strength (compressive, uniaxial tension and splitting) will be compared with experimental data and discussed in detail.

Combined effect of FTC and fatigue

For the combined effect of FTC damage and fatigue cycles. Previous studies usually show two kinds of combination. One is that the FTC and fatigue loading are applied simultaneously, like Li et al. (2011), during which the FTC damage will have negative impact on the fatigue life while the ice strengthening effect below 0ºC will increase the material's capacity and thus the fatigue life should become longer. Li et al.'s (2011) test was under closed moisture condition, and the expansive internal pressure may covert to contraction pressure after a few cycles if without additional water supple (Sicat et al., 2013; Gong et al., 2015), after which the FTC damage will not cumulate significantly. Therefore, in their experiment, the simultaneously combined effect showed a longer fatigue life compared to the pure fatigue in room temperature. On the contrary, Hasan et al. conducted the FTC test under the open moisture condition (with continuous water supply) and found continuous cumulated damage (2004). In addition, the residual elastic modulus, the static strength and fatigue life are also measured after different levels of FTC damage, which shows a serious reduction (Hasan et al., 2004; 2008). Therefore, in this study, in order to simulate a more clear degradation under the combined effect, the combination of Hasan's test will be used in the numerical analysis, that is, to simulate the static strength and fatigue life after each certain level of FTC damage.

1.3 Outline of the dissertation

Chapter 1 presents the background of the study on the damage of concrete under FTC, as well as the combined effect with external loads. The review of previous studies, the objectives of this work, and the outline of this dissertation are also shown.

Chaper 2 describes the phase equilibrium of the moisture inside the concrete material. Based on the thermodynamic theories, the chemical potential is introduced to determine the moisture phase transformation, which mainly depends on the relative humidity, temperature and the pore size. A 3D phase diagram is also presented to give a clearer image of the moisture condition in different size of pores under different environmental condition. Finally the amount of ice formation, unfrozen water and dry pores can be estimated quantitatively.

Chapter 3 mainly focus on the internal stress analysis during FTC. Based on the most well-accepted frost damage mechanisms, a more comprehensive hydraulic model is proposed which considering the poromechanical deformation and stress release by Darcy's law together. The total internal stress model is a combination of hydraulic, crystallization and cryosuction pressures, and the estimated deformation agree with experiment well. In addition, the damage cumulating in different FTC has also been considered as the permeability change, which will affect the total internal stress reciprocally.

Chapter 4 proposed a multi-phase composite model to estimate the macro mechanical properties of concrete material with the ice strengthening effect. The poromechanical theories have not taken the stress concentration in different shape of pores into consideration, which is actually a very important factor if external loads are applied. The effective elastic modulus of dry and water saturated concrete are estimated and compared with experimental data. And finally, the ice strengthening effect on the effective elastic modulus is also quantitatively analyzed.

Chapter 5 presents the mesoscale mechanical constitutive laws for RBSM analysis, based on theoretical derivations in Chapter 3 and Chapter 4. The constitutive laws are modified step by step: (1) the parallel spring system considering the deformation compatibility between porous body and ice-water system; (2) the ice strengthening effect on the stiffness and tensile strength change for the springs in RBSM; (3) the simplified and modified tension softening curve considering the cumulated damage during external fatigue cycles.

Chapter 6 shows the simulation cases and results using RBSM, which includes: (1) pure FTC deformation of mortar, mortar-aggregate interface and concrete with closed and open moisture conditions; (2) the static loading (compression, splitting tension and uniaxial tension) to the ice strengthened concrete at different low temperatures; (3) the combination of FTC damage and fatigue loads.

Chapter 7 summarizes the work done and significant findings in this study.

REFERENCES

Benveniste, Y. (1987). "A new approach to the application of Mori-Tanaka's theory in composite materials." *Mechanics of materials*, 6(2), 147-157.

Browne, R., and Bamforth, P. (1981) "The use of concrete for cryogenic storage: a summary of research, past and present." *Proc., Proceedings of the 1st International Conference on Cryogenic Concrete. London: The Concrete Society*, 135-166.

Coussy, O. and Monteiro, P.J.M., (2008). "Poroelastic model for concrete exposed to freezing temperatures." *Cement and Concrete Research*, 38, 40-48.

Coussy, O. and Monteiro, P.J.M., (2009). "Errata to "Poroelastic model for concrete exposed to freezing temperatures" [Cement and Concrete Research 38 (2008) 40–48]", *Cement and Concrete Research*, 39, 371-372.

Fagerlund, G. (2002). "Mechanical damage and fatigue effects associated with freeze-thaw of materials." M. J. Setzer, R. Auberg and H. J. Keck. Eds. *Proc. 2nd International RILSM Workshop on Frost Resistant of Concrete*, Essen 18-19 April 2002. Cachan Cedex: RILEM Publications S.A.R.L., 117-132.

Gong, F., Zhang, D., Sicat, E., and Ueda, T. (2013). "Empirical estimation of pore size distribution in cement, mortar, and concrete." *Journal of Materials in Civil Engineering*, 26(7).

Gong, F., Sicat, E., Zhang, D., and Ueda, T. (2015). "Stress Analysis for Concrete Materials under Multiple Freeze-Thaw Cycles." *Journal of Advanced Concrete Technology*, 13(3), 124-134.

Goto, Y., and Miura, T. (1979). "Experimental studies on properties of concrete cooled to about minus 160 °C." *Technology Reports*, 44(2), 357-385.

Gruebl, P. (1980). "Rapid ice formation in hardened cement paste, mortar and concrete due to supercooling." *Cement and Concrete Research*, 10, 334-345

Hasan, M., Okuyama, H., Sato, Y., and Ueda, T. (2004). "Stress-strain model of concrete damaged by freezing and thawing cycles." *Journal of Advanced Concrete Technology*, 2(1), 89-99.

Hasan, M., Ueda, T., and Sato, Y. (2008). "Stress-strain relationship of frost-damaged concrete subjected to fatigue loading." *Journal of Materials in Civil Engineering*, 20(1), 37-45.

Kaufmann, J. P. (2002). "A quantitative sequential frost deicing salt damage model based on experimental data." M. J. Setzer, R. Auberg and H. J. Keck. Eds. *Proc. 2nd International RILSM Workshop on Frost Resistant of Concrete*, Essen 18-19 April 2002. Cachan Cedex: RILEM Publications S.A.R.L., 197-204.

Kawai, T., (1977). "New element models in discrete structure analysis." *Journal of Society of Naval Architectures of Japan*, 141, 187-193.

Lee, G., Shih, T., and Chang, K. (1988a). "Mechanical properties of concrete at low temperature." *Journal of cold regions engineering*, 2(1), 13-24.

Lee, G., Shih, T., and Chang, K. (1988b). "Mechanical properties of high-strength concrete at low temperature." *Journal of cold regions engineering*, 2(4), 169-178.

Li, W., Jiang, Z., Yang, Z., Jiang, J., Sun, W., and Deng, Z. (2014). "Interactive Effect of Mechanical Fatigue Load and the Fatigue Effect of Freeze-Thaw on Combined Damage of Concrete." *Journal of Materials in Civil Engineering*.

Matsumoto, K., Sato, Y., Ueda, T., and Wang, L. (2008). "Mesoscopic analysis of mortar under high-stress creep and low-cycle fatigue loading." *Journal of Advanced Concrete Technology*, 6(2), 337-352.

Nagai, K., Sato, Y., and Ueda, T. (2004). "Mesoscopic simulation of failure of mortar and concrete by

2D RBSM." *Journal of Advanced Concrete Technology*, 2(3), 359-374.

Nagai, K., Sato, Y., and Ueda, T. (2005). "Mesoscopic simulation of failure of mortar and concrete by 3D RBSM." *Journal of Advanced Concrete Technology*, 3(3), 385-402.

Okada, T., and Iguro, M. (1978). "Bending behaviour of prestressed concrete beams under low temperature." *Special issue for J. Japan Prestressed Concrete Engrg. Assoc*, 20.

Powers, T. C. "A working hypothesis for further studies of frost resistance of concrete." *Proc., ACI journal Proceedings*, ACI.

Power, T. C., (1949). “The air requirement of frost-resistant concrete.” *Proc. Highway Res. Board*, 29, 184-211.

Rostasy, F., and Wiedemann, G. (1980). "Stress-strain-behaviour of concrete at extremely low temperature." *Cement and Concrete Research*, 10(4), 565-572.

Scherer, G.W. and Valenza II, J.J., (2005). “Mechanism of frost damage.” In: Skalny, J. and Young, F. Eds. *Materials Science of Concrete*, Vol. VII: American Ceramic Society, 209-246.

Sicat, E., Gong, F., Zhang, D., and Ueda, T. (2013). "Change of the Coefficient of Thermal Expansion of Mortar Due to Damage by Freeze Thaw Cycles." *Journal of Advanced Concrete Technology*, 11(12), 333-346.

Sun, Z. and Scherer, G.W., (2010a). “Effect of air voids on salt scaling and internal freezing.” *Cement and Concrete Research*, 40, 260-270.

Sun, Z. and Scherer, G.W., (2010b). “Pore size and shape in mortar by thermoporometry.” *Cement and Concrete Research*, 40, 740-751.

Ueda, T., Hasan, M., Nagai, K., Sato, Y., and Wang, L. (2009). "Mesoscale simulation of influence of frost damage on mechanical properties of concrete." *Journal of Materials in Civil Engineering*, 21(6), 244-252.

Wang, H., and Li, Q. (2007). "Prediction of elastic modulus and Poisson’s ratio for unsaturated concrete." *International Journal of Solids and Structures*, 44(5), 1370-1379.

Wang, L., Soda, M., and Ueda, T. (2008). "Simulation of chloride diffusivity for cracked concrete based on RBSM and truss network model." *Journal of Advanced Concrete Technology*, 6(1), 143-155.

Yaman, I., Hearn, N., and Aktan, H. (2002b). "Active and non-active porosity in concrete part I: experimental evidence." *Materials and Structures*, 35(2), 102-109.

Yang, Z., Weiss, W.J. and Olek, J., (2006). “Water transport in concrete damaged by tensile loading and freeze-thaw cycling.” *Journal of Materials in Civil Engineering*, 18 (3), 424-434.

CHAPTER 2

2. Phase equilibrium and ice formation

The moisture condition in cement-based materials is a key factor for frost action, which includes both the moisture transportation and the phase equilibrium. The moisture transportation can be explained and calculated by the potential difference, but since for the long-time estimation, the moisture condition (amount and phase) will always approach to the equilibrium condition, then it becomes quite beneficial to know the equilibrium condition if setting the certain environmental temperature and relative humidity. The phase equilibrium of free water (other than pore water) can be well explained by the traditional phase diagram. In which the equilibrium is controlled by two factors: temperature and pressure. The condition (T, p) in which the vapor, liquid and solid phase can stay together is called triple point. For free water, the triple point is (T_{tp}, p_{tp}) = (273.16K, 611.73Pa), or (T_{tp}, RH_{tp}) = (273.16K, 1). RH is relative humidity, which is defined as the ratio of the real vapor pressure to the saturated vapor pressure (p/p_s). Under the atmosphere, once the temperature falls below 0°C, all the liquid water should turn into ice; and if the relative humidity is less than 1, all the liquid water (or ice) should evaporate (or sublimate). But for pore water, it is common that only a part of liquid water would turn into ice below 0°C and also only a part of liquid water would evaporate when the relative humidity is less than 1. This is because the pore size can alter the phase equilibrium a lot. Therefore, for pore water, besides the temperature and pressure (or relative humidity), the pore radius could be the third controlling factor.

2.1 Chemical potential of each phase

In thermodynamics, chemical potential is a measure of potential that a substance has to produce in order to alter a system (Atkins and Paula, 2010). For the moisture transportation of liquid and vapor phase, moisture of a local place with higher chemical potential will move to the place that has lower one. And also for different phases, the phase with higher chemical potential will transform into the phase with lower one. Chemical potential is a relative concept and there is no absolute value. Therefore we choose the triple point of the phase diagram as a standard, that is, when the absolute temperature is 273K and relative humidity reaches 100%, the chemical potential of each phase is all equal to zero.

Vapor-liquid equilibrium

The expression of chemical potential of vapor phase is:

$$\mu_V = RT\ln(p/p_s) \tag{2.1}$$

where μ_V is the chemical potential of the vapor water (J/mol); R is the gas constant, which equals to 8.314J/mol·K. T is the absolute temperature (K). p_s is the saturated vapor pressure under the given temperature (Pa). p/p_s is the relative humidity (RH), which can be measured in experiment. Using Kelvin equation, the relationship between relative humidity and the negative pore water pressure should be:

$$P = P_0 + \frac{RT}{v_L}\ln(RH) \tag{2.2}$$

where v_L is the molar volume of the liquid phase (m^3/mol), P and P_0 are the absolute pressure of the liquid water and the atmospheric pressure (Pa), so P-P_0 is the negative water pressure (Pa). Since Kelvin equation represents the liquid-vapor equilibrium, the chemical potential of vapor and liquid phases

should always be the same if Kelvin equation is satisfied. So,

$$\mu_L = \mu_V = RT \ln \frac{p}{p_s} = (P - P_0) v_L \tag{2.3}$$

Since the negative water pressure is caused by the surface tension of the liquid-vapor interface, there is:

$$P - P_0 = -\frac{2\gamma_{LV} \cos\theta_{LV}}{r - \delta} \tag{2.4}$$

where γ_{LV}=0.072J/m^2, is the specific energy of the liquid/gas interface, δ is the thickness of the adsorbed film of water on the pore wall, which is approximately equal to 0.9 nm (Scherer, 2005), θ_{LV} is the contact angle of the liquid-vapor interface. So the chemical potential of the liquid phase should be:

$$\mu_L = -\frac{2\gamma_{LV} \cos\theta_{LV}}{r - \delta} \cdot v_L \tag{2.5}$$

For free water, $r \to \infty$, the chemical potential of liquid phase is always equal to zero. So if the relative humidity is less than 1, means $\mu_V < 0 = \mu_L$, the moisture will automatically transfer from liquid phase to vapor phase. But for pore water with the radius of r, if $\mu_V > \mu_L$, condensation will occur; if $\mu_V < \mu_L$, evaporation will occur.

Vapor-liquid-solid equilibrium

For pore water, the freezing point of liquid water depends on the pore radius. In Scherer's paper (2005), the shift of freezing point can be derived using thermodynamics of crystallization:

$$T = T_0 - \frac{\gamma_{CL} \kappa_{CL}}{\Delta S_{fv}} \tag{2.6}$$

where T_0 is the freezing point of free water, which is 0ºC, γ_{CL} is the specific energy of the crystal/liquid interface, and for ice, $\gamma_{CL} \approx 0.04$J/m^2. $\Delta S_{fv} \approx 1.2$J/(cm^3·K) is the molar entropy of fusion. κ_{CL} is the curvature of the liquid-crystal interface, which can be calculated as:

$$\kappa_{CL} = \frac{2\cos\theta_{CL}}{r - \delta} \tag{2.7}$$

where θ_{CL} is the contact angle of liquid-crystal interface, which can be assumed to be zero. At the same time, if an ice crystal is formed, the surface tension stress of the liquid-crystal interface would also generate a negative water pressure, which equals to (Scherer, 2005):

$$P = P_0 - \gamma_{CL} \kappa_{CL} \tag{2.8}$$

Since the negative pressure of the liquid water contact both ice crystal and vapor should be the same, which is (Scherer, 2005):

$$\gamma_{CL} \kappa_{CL} = \gamma_{LV} \kappa_{LV} \tag{2.9}$$

where, κ_{LV} is the curvature of the liquid-vapor interface, which is:

$$\kappa_{LV} = \frac{2\cos\theta_{LV}}{r - \delta} \tag{2.10}$$

Since the chemical potential of liquid and solid phases should also be the same if the equilibrium condition is satisfied, combine Eqs. (2.5), (2.6) and (2.9):

$$T - T_0 = -\frac{2\gamma_{CL} \cos\theta_{CL}}{(r - \delta)\Delta S_{fv}} = -\frac{2\gamma_{LV} \cos\theta_{LV}}{(r - \delta)\Delta S_{fv}} = \frac{\mu_L}{v_L} \cdot \frac{1}{\Delta S_{fv}} \tag{2.11}$$

Therefore, the chemical potential of solid phase should be:

$$\mu_C = \mu_L = \Delta S_{fv}(T - T_0)v_L \tag{2.12}$$

Thus, if in equilibrium condition, the chemical potential of vapor, liquid and solid phase could be:

$$\begin{cases} \mu_V = \mu_V(T, RH) = RT\ln(RH) \\ \mu_L = \mu_L(r) = -\dfrac{2\gamma_{LV}\cos(\theta)}{r-\delta}\cdot v_L \\ \mu_C = \mu_C(T) = \Delta S_{fv}\cdot v_L(T - T_0) \end{cases} \tag{2.13}$$

2.2 A 3D Phase diagram for pore water

Due to the tiny scale of pore space, the phase equilibrium would be affected by the surface energy of the liquid-solid and liquid-vapor interface. Thus, the triple point and also the boundary curves for every two phases will change. If adding the pore radius as the third parameter, the traditional 2D phase diagram will change to a 3D diagram; here use $1/r$ as the vertical axis, the schematic figure is shown as in Fig. 2.1 (a).

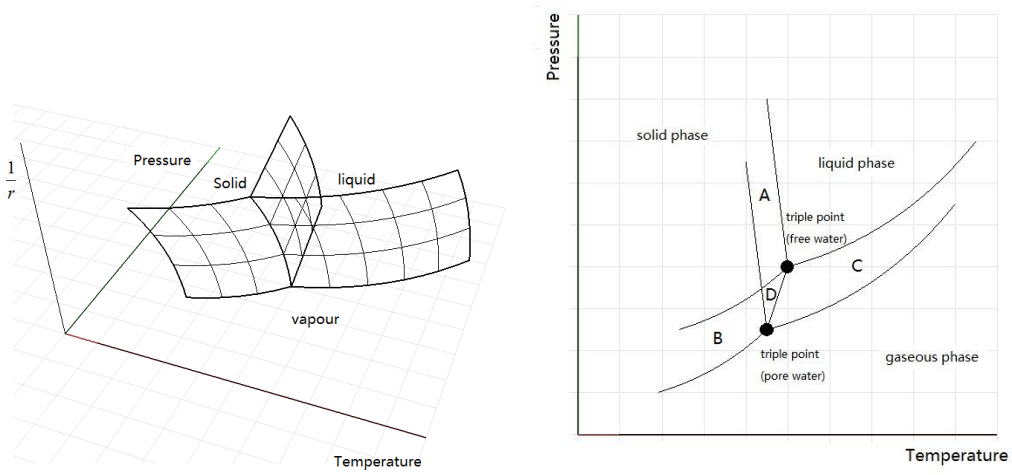

(a) (b)

Figure 2.1. Concept of the 3D phase diagram (a) 3D view (b) vertial view

Since the traditional phase diagram is for free water, that is, the pore size is infinite large ($r \to \infty$). Then as the pore size decreases, the triple point will move to lower temperature and lower water vapor pressure (Fig. 2.1 (b)). Thus, the critical line of every two phases will change to critical surfaces.

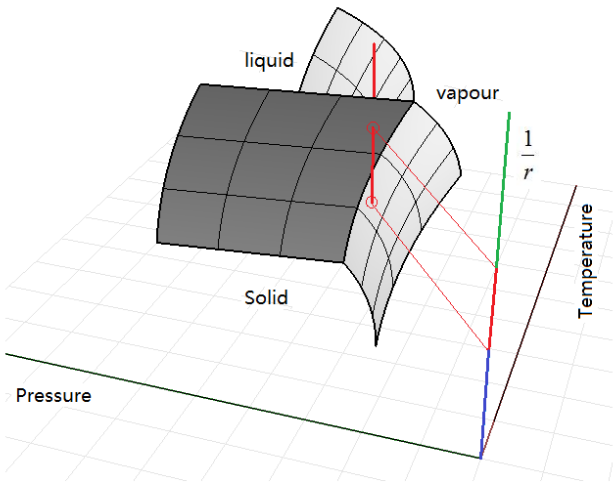

Figure 2.2. Phase of moisture in different size of pores

So even in the same environmental condition (P,T), different pores will have different water phases. For example, in Fig. 2.1 (b), if (P,T) is in A zone, ice will form in bigger pores while the water in small pores is still liquid; in B zone, bigger pores contains gas and smaller ones contains ice; in C zone, bigger pores contains gas and smaller ones contains liquid water. But if (P,T) is in D zone, since the vertical line will intersect with two critical surfaces, there will be three phases in different pores (see Fig. 2.2). The blue, red and green parts represent the range of pore radius, which will stay in gas, ice, and liquid water respectively.

Shift of triple point

For a given size of pore, the shift of the freezing temperature can be determined by Eq. (2.6). The equilibrium vapor pressure regarding pore radius can be derived by combining Eq. (2.2) and Eq. (2.4):

$$p = \exp(-\frac{2\gamma_{LV}\cos\theta_{LV}}{r_p - \delta}\cdot\frac{v_L}{RT})\cdot p_s(T) \tag{2.14}$$

where $p_s(T)$ is the function of saturated vapor pressure under different temperature. If the (p,T) condition in a pore with radius of r satisfy that three phase can stay together, means the temperature $T=T_0-\gamma_{CL}\cdot\kappa_{CL}/\Delta S_{fv}$, then the equilibrium vapor pressure should be:

$$p(r) = \exp(-\frac{2\gamma_{LV}\cos\theta_{LV}}{r-\delta}\cdot\frac{v_L}{R\cdot(T_0 - \frac{2\gamma_{CL}}{(r-\delta)\Delta S_{fv}})})\cdot p_s(T_0 - \frac{2\gamma_{CL}}{(r-\delta)\Delta S_{fv}}) \tag{2.15}$$

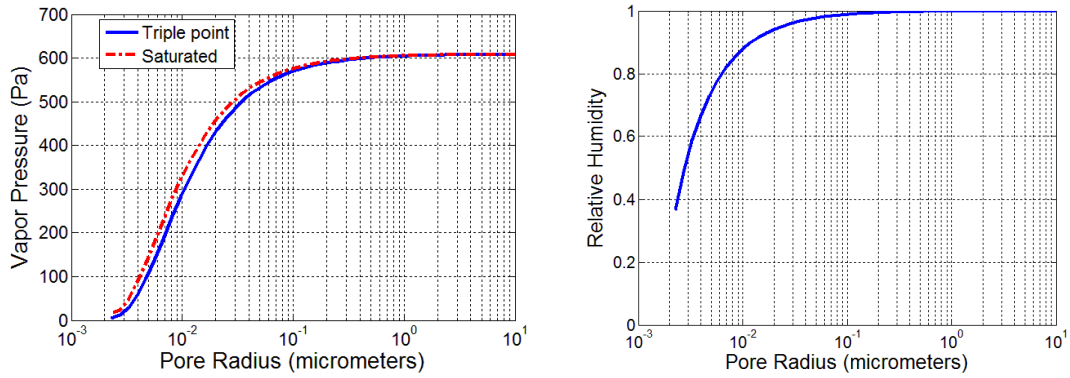

(a) (b)

Figure 2.3. Vapor pressure corresponding to pore radius (a) absolute vapor pressure of triple point and the ambient saturated vapor pressure under the corresponding temperature; (b) equilibrium relative humidity (the ratio of two curves in Fig. 2.3 (a))

From Fig. 2.3, it can be seen that the absolute change of vapor pressure due to pore size is not significant, but the ratio (relative humidity) is more significant. Besides, even the relative humidity of the ambient environment falls down to 0.6, the three phases of moisture can still co-exist in the pores smaller than 3.3nm.

Boundary of every two phases

In order to quantitatively determine the 3D phase diagram, other than the triple point change, the boundary curve between every two phases with different pore radius should also be derived. Since the boundary curve means the two phases can exit together stably, the chemical potential of two phases should also be the same.

1) Liquid-vapor boundary ($\mu_V = \mu_L$), then,

$$p = p_s(T) \cdot \exp(-\frac{2\gamma_{LV}\cos\theta_{LV}}{r-\delta} \cdot \frac{v_L}{RT}) \tag{2.16}$$

2) Solid-vapor boundary ($\mu_V = \mu_C$), then,

$$p = p_s(T) \cdot \exp(\Delta S_{fv} \cdot v_L (T - T_0) \cdot \frac{1}{RT}) \tag{2.17}$$

3) Solid-liquid boundary ($\mu_L = \mu_C$)

According to Scherer's paper (1999), it is necessary to impose a compressive stress on the ice if we want to prevent it from growing when temperature decreases.

$$p - p_{tp} = \int_T^{T_{tp}} \Delta S_{fv} dT \approx \Delta S_{fv}(T_{tp} - T) \tag{2.18}$$

In the real condition, the structure is usually under atmospheric pressure, so Eq. (2.18) is not often used, unless the materials is under high pressure, like underground or undersea structures. The phase equilibrium in high external pressure environment needs to be studied in the next study.

A more practical form

Actually the absolute vapor pressure is not convenient to use. In civil engineering, the relative humidity *RH* is more often used to describe the effect of vapor pressure. Thus, for practical use, the triple point and the phase boundaries can be rewritten using *RH* in place of *p*. Then the triple point and phase boundaries can be written as Eq. (2.19) and Eq. (2.20).

$$\begin{cases} T_{tp}(r) = T_0 - \dfrac{2\gamma_{CL}}{(r-\delta)\Delta S_{fv}} \\ RH_{tp}(r) = \exp(-\dfrac{2\gamma_{LV}\cos\theta_{LV}}{r-\delta} \cdot \dfrac{v_L}{R\cdot(T_0 - \dfrac{2\gamma_{CL}}{(r-\delta)\Delta S_{fv}})}) \end{cases} \tag{2.19}$$

$$\begin{cases} RH(r,T) = \exp(-\dfrac{2\gamma_{LV}\cos\theta_{LV}}{r-\delta} \cdot \dfrac{v_L}{RT}) & \text{liquid-vapor} \\ RH(r,T) = \exp(\Delta S_{fv} \cdot v_L (T - T_0) \cdot \dfrac{1}{RT}) & \text{solid-vapor} \end{cases} \tag{2.20}$$

Fig. 2.4 shows the calculated diagram. The relative humidity is chosen for convenience. The two surfaces in the 3D figure represent the critical radii of each phase under any given environmental condition (*T*, *RH*). The two surfaces divide the whole space into three parts, representing different phase of moisture respectively. The value of the contour figure is the logarithm of the pore radius, for example, -8.6 means $\log_{10}(r)$=-8.6. The horizontal contour means the critical radii of empty pores and pores occupied by moisture (liquid or solid), and the vertical contour represents the critical radii of the liquid-solid interface. It can be seen that how much pores are empty is mainly controlled by the relative humidity of the environment, while how much moisture will turn into ice is mainly determined by the temperature. So from this figure, if just using one parameter (*RH* for total moisture content and *T* for ice content) to calculate the critical radii, the calculation would be much more simple, and the accuracy could still be acceptable. The black line in both figures is the critical radii when vapour, liquid and solid phase could stay together stably.

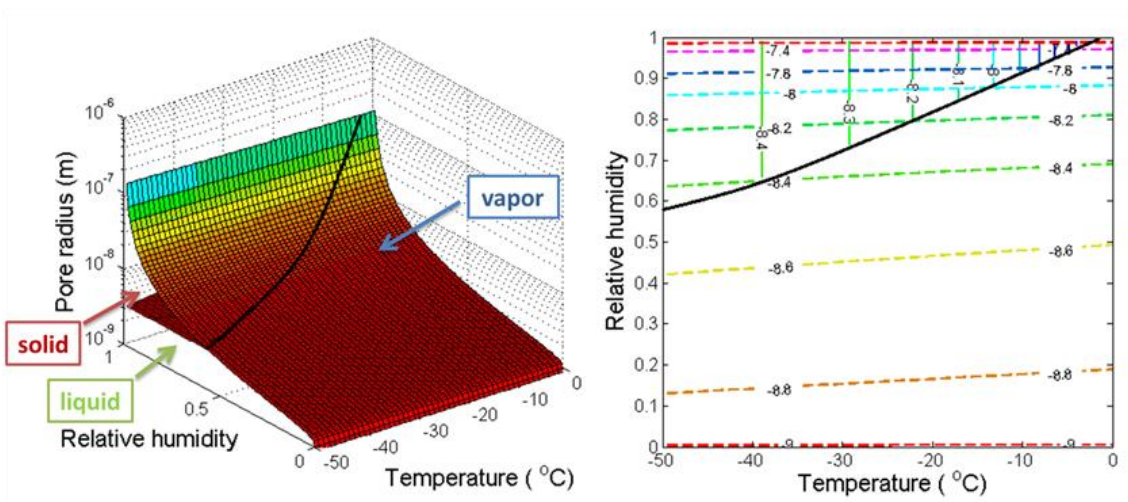

Figure 2.4. Calculated 3D phase diagram and critical radii

2.3 Estimation of ice formation

Frost damage is a serious deterioration problem for concrete materials in cold region. The internal force is caused by the freezing process of the pore water. Although there are some different mechanisms, like the hydraulic pressure proposed by Power (1945) or the crystallization pressure proposed by Scherer (2005), the ice formation is always the key point of this problem. Thus, it is beneficial to get find a convenient and clear way to get this information.

From Fig. 2.4, the moisture movement process (evaporation and condensation), and the ice

formation process (freezing and thawing) can be approximately studied separately, which means that if the environmental relative humidity does not change much, the ice formation process is mainly controlled by the temperature. So when T reaches the freezing point T_f (calculated by Eq. (2.6)), the chemical potential of each phase is just the same ($\mu_V = \mu_L = \mu_C$). If $T > T_f$, then $\mu_V = \mu_L < \mu_C$, there is no ice formed. If $T < T_f$,, then $\mu_V = \mu_L > \mu_C$, ice will continuously forms. Since the speed of liquid to solid phase transfer is much faster than the moisture movement within the concrete, at last, the chemical potential of liquid and solid phase should be the same, but lower than the environmental vapour phase $\mu_V > \mu_L = \mu_C$. It means that if the RH of the environment is high enough to satisfy $\mu_V > \mu_C$, the vapor water will continuously condensate to liquid or solid phase until the material is saturated, but this process usually take very long time so that it can be neglected during a short period.

In order to estimate the real ice content in the cement-based material, the pore size distribution is needed. But unfortunately it is not feasible to do experimental measurement every time, like using Mercury Intrusion Porometry (MIP), Nitrogen or Water Adsorption, Thermoporometry or Image Analysis. So an empirical estimation of pore size distribution is very helpful for such estimation. Here the empirical formula developed by Gong et al. (2012) is used to get the cumulated pore volume with pore radii larger than r_0:

$$V_N(r \geq r_0) = 1 - \frac{(1-k)[1+(C-1)k] \cdot e^{-\frac{2\gamma_{LV}\cos\theta}{(r_0-\delta)RT}v_L}}{(1-k \cdot e^{-\frac{2\gamma\cos\theta}{(r_0-\delta)RT}v_l})[1+(C-1)k \cdot e^{-\frac{2\gamma_{LV}\cos\theta}{(r_0-\delta)RT}v_L}]} \tag{2.21}$$

Eq. (2.21) was derived based on the water adsorption isotherm proposed by Xi et al. (1994), which reflects the liquid-vapor equilibrium in different size of pores. V_N is the normalized cumulated pore volume (0 to 1), C and k are parameters which can be decided by Xi et al's paper (1994):

$$\begin{cases} k = \dfrac{(1-\frac{1}{n})C-1}{C-1} \\ n = (2.5+\frac{15}{t})(0.33+2.2\frac{w}{c}) \times 1.5 \\ C = \exp(\frac{855}{RT}) \end{cases} \tag{2.22}$$

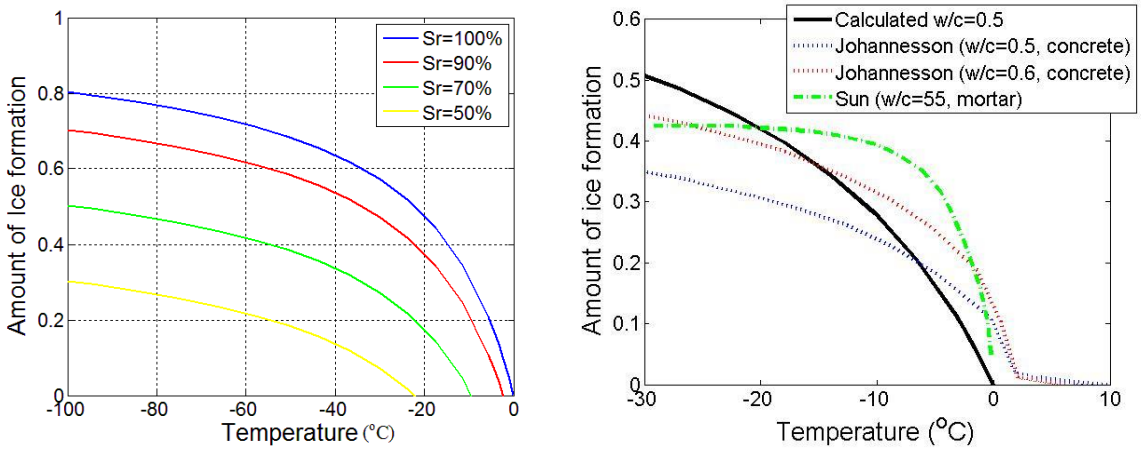

(a) (b)

Figure 2.5. Estimated ice amount (a) calculated ice formation curve (w/c=0.5) (b) comparison with previous study

Using the pore size distribution estimated above, the ice content can be calculated for different saturation degree and temperature (Fig. 2.5 (a)). The calculated results show: (1) higher saturation degree results in higher ice initiation temperature and more ice content; (2) as the temperature goes down, more ice will form but the increment rate will decrease. And also some previous experiments which measuring the ice content directly by calorimeter (Jonannesson, 2010; Sun and Scherer, 2010) are compared with the calculated curve. It can be seen that the calculated curve is well within the range of experimental data.

2.4 Conclusions of this chapter

This chapter mainly dues with the moisture equilibrium and phase change inside the concrete material at low temperatures, and the following conclusions can be drawn:

(1) The concept of the 3D phase diagram for pore water in cement-based materials is introduced, which includes the effect of pore size. This 3D diagram can give clear vision and explanation about the complex moisture equilibrium inside the materials. Not only restricted to the cement-based materials, this tool can also be applied to all kinds of porous materials.

(2) The quantitative 3D figure is drawn, the phase of moisture under any given environmental condition can be determined. The critical radii of every two phases and also the radii for three phases to stay together can be calculated. It has been found that the total moisture content, which includes both liquid and vapor phase is mainly controlled by the relative humidity. While how much of this liquid water would turn into ice is mainly determined by the temperature. So the numerical program for this problem can be improved by reducing insignificant parameters to achieve a better balance between efficiency and accuracy.

(3) The ice content can be estimated when knowing the pore size distribution. An empirical pore size distribution formula is also used to achieve this goal. The calculated results are shown, and compared with some available experimental data, but more strict experimental verification should be made in the next study.

(4) The thermodynamic model in this study is still an ideal one, in which the shape of pores has not been considered. For example, the large pore may have small entry, which makes the freezing point different. But it can be solved by introducing the pore shape information in this study, which will be done in the future study.

REFERENCES

Atkins, P., Paula, J. (2010). *Physical Chemistry*, W. H Freeman and Company, New York, ISBN 978-1-4292-1812-2

Gong, F., Sicat, E. and Ueda, T. (2012). “Estimation of pore size distribution of cement-based materials by using water adsorption isotherms.” *Proceedings of the 3nd International Conference on Durability of Concrete Structures*, Hong Kong.

Johannesson, B. (2010). “Dimensional and ice content changes of hardened concrete at different freezing and thawing temperatures” *Cement & Concrete Composites*, 32: 73-83

Powers, T. C. (1945). “A working hypothesis for further studies of frost resistance of concrete” Journal

of the American Concrete Institute, Vol. 16 No. 4, 245-272

Scherer, G. W. (1999). “Crystallization in pores” *Cement and Concrete Research*, 29, 1347-1358

Scherer, G.W. (2005). “Mechanisms of Frost Damage” *Materials Science of Concrete*, Vol. VII, eds. J. Skalny and F. Young (American Ceramic Society) 209-246

Sun, Z., Scherer, G. W. (2010). “Effect of air voids on salt scaling and internal freezing” *Cement and Concrete Research*, 40: 260-270

Xi, Y., Bazant, Z.P., Jennings, H.M. (1994). “Moisture diffusion in cementitious materials Adsorption isotherms” *Advanced Cement Based Materials*, 1: 248-257.

CHAPTER 3

3. Stress analysis under FTC

Once ice forms in highly saturated concrete material, internal tensile stress will be generated and causes damage to the material, which is a serious problem for concrete structures in cold and wet regions. On one hand, each component (porous body, ice and liquid) should satisfy the compatibility of stress and strain, which has been discussed by the poromechanical theories. On the other hand, if some empty voids exist, the hydraulic pressure will release when liquid water escapes from the expanded area according to Darcy's law. Recent closed freeze-thaw tests on the saturated mortar showed a consistent tendency: as the number of freeze-thaw cycles (FTC) increases, the deformation changes from the expansion to the contraction. In order to make clear the physical and mechanical changes during this process, a more comprehensive hydraulic model is developed, which combines both the mechanisms mentioned above. The estimated strain behavior by this model is in a good agreement with experimental measurements, and also, it has good potential and is more flexible to be applied to different cases such as different saturation degrees and cooling rates. The permeability change can be also considered in this model as a reflection of frost damage level.

3.1 Existing hydraulic pressure models

There are two main hydraulic theories for the freezing process in porous material. One is proposed by Powers (1949), aiming at discussing the suitable spacing factor of the air bubbles to avoid frost damage in the air-entrained concrete. In his model, it was assumed that all the liquid water can be expelled into the entrained air once ice forms in the surrounding material. According to Darcy's law, a pressure gradient is necessary to drive such kind of water flow, thus hydraulic pressure is generated.

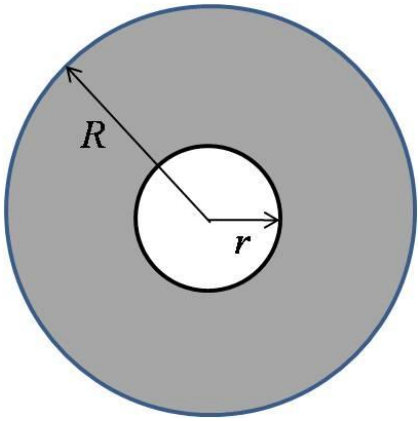

Fig. 3.1 Empty space and influential volume

Fig. 3.1 shows the basic concept of Powers' model. The central circle represents the empty air void with a radius of r, and the influential volume has a radius of R. Since the deformation of porous body was neglected, the expanded volume during ice formation should be balanced by the flow into the air void. According to this assumption and Darcy's law, Powers gave the hydraulic pressure at x ($r \le x \le R$) along the radial direction as:

$$p_h(x) = \frac{\eta}{k} \cdot \frac{1}{3}(1.09 - 1/S_r) \cdot \phi \cdot \frac{dw_f}{dT}\frac{dT}{dt} \cdot \int_r^R \left(\frac{R^2}{x^2} - x \right) dx \tag{3.1}$$

where $p_h(x)$ is the hydraulic pressure at each location, k is the permeability of porous material (m^2), η is the viscosity of liquid water (Pa·s), S_r is the saturation degree, ϕ is the void ratio, dw_f/dT is the ice forming rate as temperature changes, which depends on the pore size distribution, and finally dT/dt is the cooling rate.

Other than Powers' model, Coussy and Monteiro (2009) ignored the water flow, and proposed a poromechanical model for saturated porous materials, in which the increased volume can be balanced by the self-compression of liquid and solid water, and the pore pressure p_h is approximately obtained as follows (Coussy and Monteiro, 2009):

$$p_h \approx 0.09 \cdot \frac{\psi_C}{\psi_C / K_C + (1-\psi_C) / K_L} \tag{3.2}$$

where ψ_C is the ice content, 1-ψ_C is the liquid water content. K_C and K_L are the bulk moduli of the ice and liquid, respectively. This model also describes an ideal condition based on the assumption that the hydraulic pressure resulting from the volume change cannot be released (like in the sealed condition or the case of air voids that are very far apart from each other). So actually this model shows the upper bound that the pore pressure could reach.

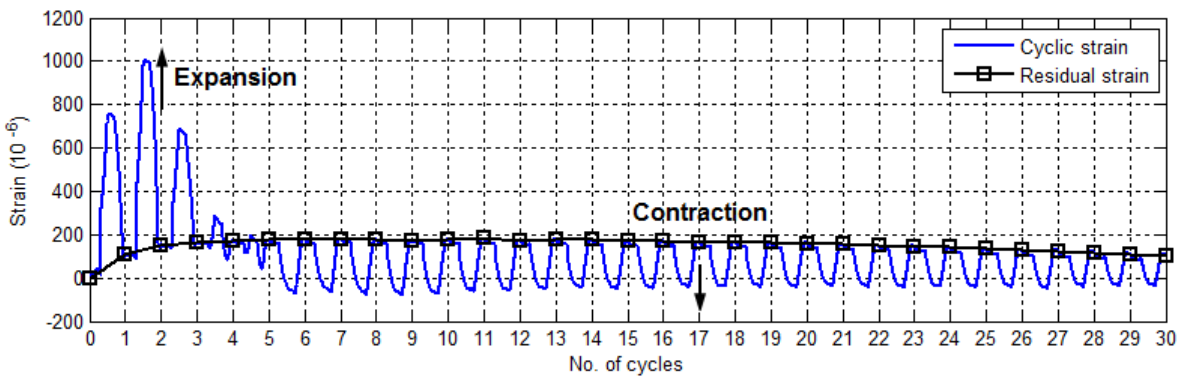

Fig. 3.2 Strain behavior during 30 cycles (water saturated, sealed and without thermal strain) (Sicat et al, 2013)

However, in reality, both water flow and self-compression exist, and which would be the dominant effect depends on the distribution of empty pores (like entrained or entrapped air) and permeability of the materials. That is, an upper bound of hydraulic pressure will be reached if there is only self-compression effect. But if the liquid water can move more easily to the empty voids (when empty voids are closer to each other or the permeability becomes bigger), the hydraulic pressure will release due to the escaped flow. Then if the water flow becomes the dominant effect, the hydraulic pressure will decrease and even become negligible. For example, Fig. 3.2 shows the measured deformation on the water-saturated mortar with closed moisture condition during 30 freeze-thaw cycles (Sicat et al. 2013). The reversing strain behavior from expansion at the beginning to contraction at last also reflects the change of total internal pore pressure: from positive value to negative value. The total pore pressure is the sum of hydraulic, crystallization and cryosuction pressures, and the crystallization and cryosuction pressures are always coexisting and regarded unchanged during the test (details will be discussed later). The sum of crystallization and cryosuction pressure is negative under the given environmental condition, but the hydraulic pressure is large enough at the beginning so that the total pressure is still positive. Since this total internal pressure can easily exceed the tensile strength of the porous body, damage will happens as internal micro-cracks and the permeability will increase (Yang et al. 2006). Then the

hydraulic pressure will decrease until it cannot cause further damage, and the total internal pressure will become negative in this study and results in contraction in the strain, which reduces the tensile remaining strain and may eventually increase the compression remaining strain (Fig. 3.2). Therefore the hydraulic pressure decreasing in the above test means a change from self-compression effect dominant to water flow dominant in the model, thus the two effects should be combined together to describe the observed phenomenon.

3.2 Proposed hydraulic pressure model

If the specimen is not fully saturated, the empty voids have the potential to hold the increased volume. Usually the water saturated specimens without special treatment (like vacuum saturation) are not really fully-saturated (95.8% in our test). Therefore, even for the closed test with the non-air entrained samples, there is still enough space to allow the volume increase when ice forms. But since the permeability of cement paste is extremely low, the water flow cannot be fast enough to avoid the hydraulic pressure.

Actually Powers' model was aiming for the hydraulic pressure in the air-entrained cement pastes, which is slightly different with our case (non-air-entrained concrete with different saturation degree). However, the concept and method can be used for this study. Even the air-entrainment agent was not used, the central sphere can still represent the empty space (Fig. 3.1), while the outer influential volume shows the range of pore water that will flow into this empty space. In addition, it is assumed that the liquid water will always occupy the smallest pore first, so if the central sphere represents the empty part, then the surrounding shell should be fully saturated.

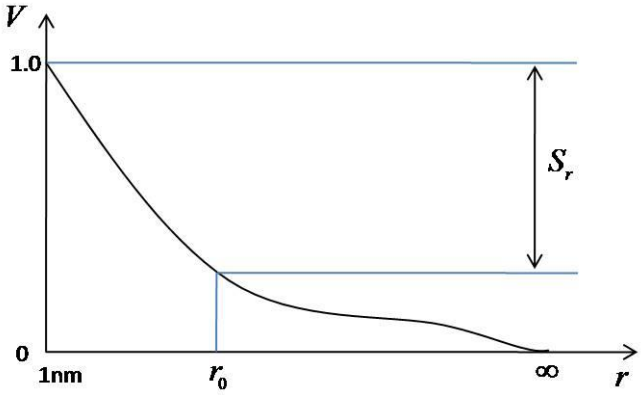

Fig. 3.3 Typical cumulated pore size distribution

If the saturation degree is S_r, the critical radius r_0 between empty and fulfilled pores can be determined by Fig. 3.3, and the pore size distribution can be obtained by experiments or empirical equations (Gong et al., 2014). Also in Fig. 3.3, it is assumed that the pores whose radii are bigger than r_0 will stay empty. Here the equivalent radius r_E can be chosen by the weighted mean value of empty volume:

$$r_E = \frac{\int_{\infty}^{r_0} r \cdot v(r)dr}{\int_{\infty}^{r_0} v(r)dr} \tag{3.3}$$

where $v(r)$ is the volume density of pores. The volume ratio of the central sphere to outer sphere should be equal to the real volume fraction of empty space to the whole material:

$$\frac{r_E^{\ 3}}{R_E^{\ 3}} = (1 - S_r) \cdot \phi \tag{3.4}$$

where R_E is the influential volume corresponding to r_E. Using Q to represent the water flow driven by the average pore pressure (p_h) in the surround area, which is:

$$Q = \frac{A}{V}\int q dt \quad (A = 4\pi r_E^{\ 2}, V = \frac{4}{3}\pi(R_E^{\ 3} - r_E^{\ 3})) \tag{3.5}$$

$$q = \frac{k}{\eta} \cdot \frac{\Delta p_h}{\Delta x} \quad (\Delta p_h = p_h, \Delta x = (R_E - r_E)/2) \tag{3.6}$$

The pore pressure (p_h) can be converted to the hydraulic stress (P_H) by the poromechanics, which is:

$$P_H = b p_h \tag{3.7}$$

where b is the Biot coefficient, and defined as b=2ϕ/(1+ϕ) (Coussy, 2004). At the same time, due to this pressure P_H, the material will expand while the liquid and ice will be compressed, that is:

$$\begin{cases} \varepsilon_p = P_H / K_p \\ \varepsilon_C = -p_h / K_C \\ \varepsilon_L = -p_h / K_L \end{cases} \tag{3.8}$$

where ε_p, ε_C and ε_L are the volume strain of the porous body, ice and liquid water, respectively. And here linear behavior is assumed for all these three components for convenience. Usually there is plastic deformation on the material, which will be discussed later, here we just choose the simple poroelastic relation. Then the increased volume by ice forming can be balanced by two parts:

$$0.09\phi\psi_C - Q = \varepsilon_p - \phi\psi_C\varepsilon_C - \phi\psi_L\varepsilon_L \tag{3.9}$$

After differentiation of Eq. (3.9) with respect to time, the following equation is derived:

$$0.09\phi\dot{\psi}_C - \frac{A}{V} \cdot q = \dot{\varepsilon}_p - \phi\psi_C\dot{\varepsilon}_C - \phi\psi_L\dot{\varepsilon}_L \tag{3.10}$$

Taking Eqs. (3.5), (3.6) (3.7) and (3.8) into Eq. (3.10):

$$0.09\phi\dot{\psi}_C - \frac{A}{V} \cdot \frac{k}{\eta} \cdot \frac{2}{R_E - r_E} p_h = \left(\frac{b}{K_p} + \frac{\phi\psi_C}{K_C} + \frac{\phi\psi_L}{K_L}\right) \cdot \dot{p}_h \tag{3.11}$$

Eq. (3.11) is the proposed hydraulic model in this paper, if knowing the environmental conditions, moisture conditions and the material properties, the time dependent hydraulic pressure (p_h) can be calculated by solving Eq. (3.11). For convenience, let $C_1 = \frac{A}{V} \cdot \frac{k}{\eta} \cdot \frac{2}{R_E - r_E}$, $C_2 = \left(\frac{b}{K_p} + \frac{\phi\psi_C}{K_C} + \frac{\phi\psi_L}{K_L}\right)$ and $C_3 = 0.09\phi\dot{\psi}_C$, then Eq. (3.11) becomes:

$$C_1 \cdot p_h + C_2 \cdot \dot{p}_h = C_3 \tag{3.12}$$

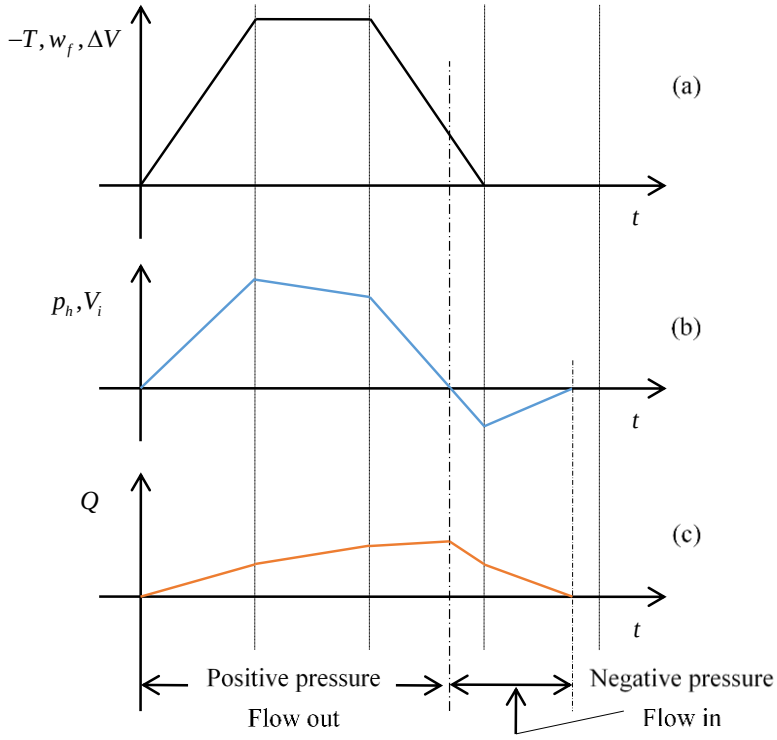

Fig. 3.4 Change of each parameters (a) temperature (-*T*), frozen water amount (w_f), total increased volume (ΔV) (b) hydraulic pressure (p_h), volume balanced by deformation (V_i=ΔV-Q) (c) the released flow (Q).

According to Eq. (3.12) and Fig. 3.4, some basic characters of the modified model can be seen as below:

(1) During the freezing process, ice forms so that $\dot{\psi}_C > 0$, and only part of the increased volume will flow away based on Darcy's law ($C_1 \cdot p_h < 0.09\phi\dot{\psi}_C$). Therefore, the hydraulic pressure is increasing according to Eq. (3.12) ($\dot{p}_h > 0$).

(2) When the temperature reaches the lowest value and keeps constant, the ice formation stops ($\dot{\psi}_C = 0$) and C_1 and C_2 are positive, which means p_h and $\dot{p}_h$ should have opposite sign. Since $p_h > 0$, so $\dot{p}_h < 0$, then the hydraulic pressure should still be positive but gradually release.

(3) When the temperature raises up, the ice content will decrease ($\dot{\psi}_C < 0$), the hydraulic pressure will continue to decrease but much faster compared to the constant temperature period. Once the hydraulic pressure becomes negative, the expelled water will move back again from the central void. So it is possible to have short period with negative hydraulic pressure (Fig. 3.4 (b)). At last, all the expelled water during ice formation will move back so the moisture distribution is assumed same as the beginning.

(4) According to different saturation conditions, Eq. (3.12) can be changed back to Coussy and Monteiro's model or Powers' model. For example, if the release of hydraulic pressure is quite limited ($C_1 \approx 0$, like very high saturation condition), then it becomes:

$0.09\phi\psi_C = \left(\frac{b}{K_p} + \frac{\phi\psi_C}{K_C} + \frac{\phi\psi_L}{K_L}\right) \cdot p_h$ which is similar to Coussy and Monteiro's model. If the permeability is higher (like due to frost damage accumulation) so that the water corresponding to increased volume can move to the central void more quickly ($C_2 \approx 0$), then it becomes Powers' model.

3.3 Ice formation and permeability

According to the discussion in Chapter 2, the ice content (the volume fraction of pore space filled with ice) can be drawn as a function of temperature. Although the ice amount at each freezing temperature can be estimated if adopting an empirical pore size distribution, as presented in Section 2.3, one of the essential parameters are still unknown, which is the pore shape factor. The pore shape factor can explain the differences between the freezing curve and melting curve (Fig. 3.5), because the freezing point is usually controlled by the size of pore entry while the melting point is by that of pore body (Sun, 2010b), and the pore shape factor λ can be defined as:

$$\lambda = \frac{\Delta T_M}{\Delta T_F} \tag{3.13}$$

where ΔT_m and ΔT_f are the drop of melting point and freezing point with the same ice content. For the same amount of ice content, ΔT_m is always smaller than ΔT_f. Sun's experimental data show that λ is usually between 0.1 and 0.5 for cement-based materials (Sun, 2010b).

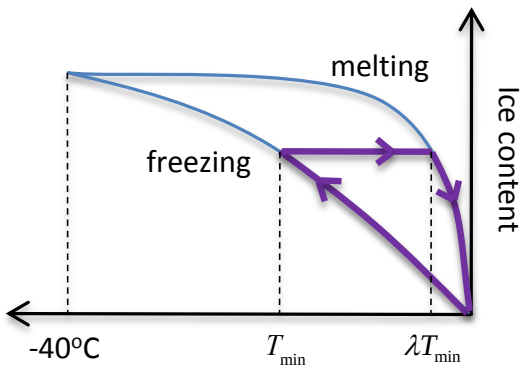

Fig. 3.5 Freezing and melting curve used in the analysis

The shape factor will not only affect the freezing and melting curve, but also be necessary to calculate the crystallization pressure (discussed in next section), therefore, here it is better to choose some experimental measurements which have both the information of ice content and pore shape factor. There are limited ways to measure the ice content inside the concrete, such as the thermoporometry (Sun and Scherer, 2010a; Johannesson, 2010) and electronic method (Cai and Liu, 1998). Among those experimental data, Sun's test (2010a) is chosen to give general characters of ice forming and melting process, because the experiments were more precisely controlled and the results can correlate different variables reasonably and comprehensively, such as the ice content, pore shape, pore size distribution and deformation. In addition, the majority of formed ice is in the smaller pores (r < 100 nm), of which the normalized pore size distributions are very similar among different W/C ratios (Gong et al., 2014). Therefore, the ice content of fully saturated specimen can be empirically regressed based on Sun's DSC data (2010a), in regarding with the temperature:

$$w_f = -3.585\times10^{-4}T^2 - 0.0236T \quad (-40^{o}C<T<0^{o}C) \tag{3.14}$$

$$w_m = \frac{0.449T}{T-2.525} \quad (-40^{o}C<T<0^{o}C) \tag{3.15}$$

The melting point is always higher than the freezing point for the same pores. If the temperature reaches the lowest value $T_{\min}$, and then increases again, the existing ice would not start to melt immediately, until the temperature reaches $\lambda T_{\min}$ (Fig. 3.5). Thus, the melting curve should be adjusted according to the lowest temperature as:

$$w_m = \begin{cases} -3.585\times10^{-4}T_{\min}{}^2 - 0.0236T_{\min} & (T_{\min} < T < \lambda T_{\min}) \\ \dfrac{0.449T}{T-2.525} & (\lambda T_{\min} < T < 0^{o}C) \end{cases} \tag{3.16}$$

If the specimen is partially saturated (S_r<1), which means the biggest pores with volume fraction of (1-S_r) are empty, then the real ice content can be assumed as the value calculated by Eqs. (3.14) and (3.15) but subtracted by (1-S_r):

$$\psi_C = \begin{cases} w_f - (1-S_r) & (\text{freezing}, w_f > (1-S_r)) \\ w_m - (1-S_r) & (\text{melting}, w_m > (1-S_r)) \end{cases} \tag{3.17}$$

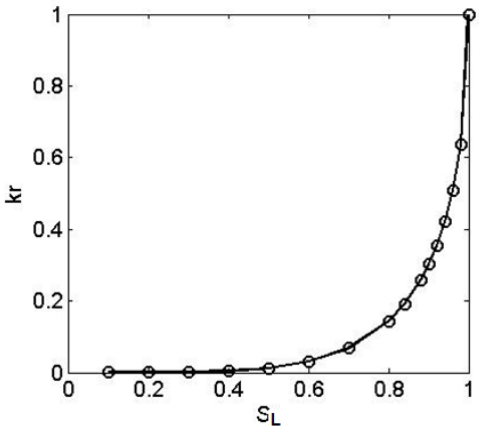

Fig. 3.6 Relative permeability to liquid saturation degree

The permeability of unsaturated porous material has been well described by the van Genuchten equations as (van Genuchten, 1980):

$$k_r = \frac{k}{k_0} = S_L{}^{0.5}[1-(1-S_L{}^{\frac{1}{m}})^m]^2 \tag{3.18}$$

$$S_L = [1+(\frac{P}{P_0})^{1/(1-m)}]^{-m} \tag{3.19}$$

where k_0 is the permeability of fully saturated material, k is the permeability under the saturation degree of S_r, k_r is the relative value that shows the reduction effect. m is the parameter that needs to be determined using Eq. (3.19), in which the S_r can be experimentally measured as a function of capillary pressure P/P_0. Although van Genuchten equations are originally for soil media and also for the vapor-liquid system, Coussy (2005) has discussed the feasibility to use those equations to describe the cement-based materials and also the effect of ice formation. It has been discussed that the permeability mainly depends on the "liquid saturation", which means no matter the larger pores are occupied by gas or ice

crystal or both, they have the same effect on the permeability of liquid water. A more practical expression for cement-based material was given by Coussy (2005) as:

$$S_L = [1 + (\frac{R_*}{R_f})^{1/(1-m)}]^{-m} \tag{3.20}$$

where R_f is the critical pore size for freezing under different temperatures. R_*=4.26nm for cement-based materials, which is a factor reflecting the radius of pores which can be percolated to each other. Then the parameter m can be determined according to Sun's DSC data (2010b), and it is approximately equal to 0.5. Therefore, the relative permeability by liquid saturation should be (also see Fig. 3.6):

$$k_r = \frac{k}{k_0} = S_L^{0.5}[1-(1-S_L^{2})^{0.5}]^2 \tag{3.21}$$

3.4 Crystallization and cryosuction pressures

Due to the surface tension, there is a pressure difference between liquid and crystal on the crystal/liquid interface, and also a difference between liquid and gas on the liquid/vapor interface. If assuming that the pressure of the gas is the same as the ambient pressure (zero), then the cryosuction pressure is always negative, depending on the liquid saturation degree. The pressure uniformity of liquid phase requires that the surface tension of crystal/liquid interface and liquid/vapor interface should be equal:

$$\kappa_{CL}\gamma_{CL} = \kappa_{LV}\gamma_{LV} \tag{3.22}$$

where κ_{LV} and γ_{LV} represent the curvature and surface energy of liquid/vapor interface respectively. Then, the cryosuction pressure can be related to the freezing point by:

$$\Delta p = -\kappa_{LV}\gamma_{LV} = \Delta S_{fv}(T - T_0) \tag{3.23}$$

Therefore, the cryosuction pressure can be calculated simply from the temperature distribution:

$$p_l = \psi_L \cdot \Delta S_{fv}(T - T_0) \tag{3.24}$$

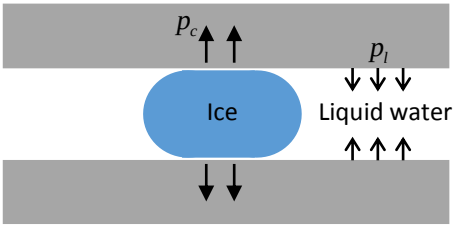

Fig. 3.7 Crystallization pressure and cryosuction pressure in a cylindrical pore

The crystallization pressure is pressure between the ice crystal and the pore wall, see p_c in Fig. 3.7. This kind of pressure is different from the hydraulic pressure caused by volume expansion, but generated due to the differences in the curvatures at different locations of the ice crystal (Scherer and and Vallenza II, 2005). For example, in Fig. 3.7, if there is no force coming from the pore wall, the ice crystal should always grow spherically. However, due to the constraint of the irregular shape of pores, the ice crystal will hardly grow spherically, then a force must be applied to the ice crystal to ensure such shape of growth, and this kind of force between the ice crystal and the pore wall is called crystallization pressure. It can be imagined that whenever the saturation degree is high or low, once ice forms, the crystallization pressure will always exist. The crystallization pressure acting on the pore wall is always

accompanied with the cryosuction pressure (Fig. 3.7), and also depends on the shape of the pores (λ) based on data from Sun (2010a):

$$p_c = \psi_C \cdot (1-\lambda)\Delta S_{fv}(T - T_0) \tag{3.25}$$

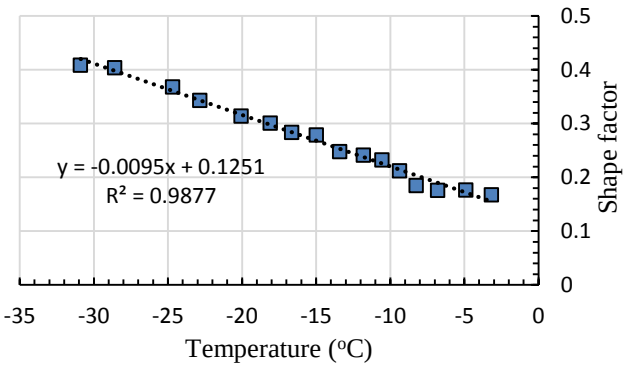

Fig. 3.8 Pore shape factor as a function of freezing point, based on Sun (2010a)

According to the experimental data (Sun, 2010a), the shape factor that defined by Eq. (3.13) can be approximately rewritten as a linear function of freezing point (Fig. 3.8), then, Eq. (3.25) becomes:

$$p_c = \psi_C \cdot (0.875 + 0.0095T)\Delta S_{fv}(T - T_0) \tag{3.26}$$

3.5 Experimental verification

The mortar specimens in this experiment (Sicat et al. 2013) used ordinary Portland cement with density of 3.14 g/cm^3, fine aggregate which is 1.2mm or less in size with density of 2.67 g/cm^3 at 1467.6 kg/m^3 of concrete without air entraining agent to promote damage. Mix proportion for specimens is 1:2:6 (water: cement: fine aggregate). After curing, specimens were cut into size of 40mm x 40mm x 2mm (see Fig. 3.9 (a)). Specimens were submerged underwater until mass was constant to attain full saturation. Finally, the specimens were sealed with vinyl tape to prevent water uptake or loss. The preparation of the specimens is shown in Fig. 3.9 (a) and (b). The size distribution of entrapped air can be obtained from image anlysis (Fig. 3.9 (c)). The critcal radius r_0 between empty and fullfilled pores can be estimated combining pore size information and saturation condition (Gong et al. 2014), which is shown in Table 3.1. Finally Fig. 3.9 (d) shows the temperature history of each cycle.

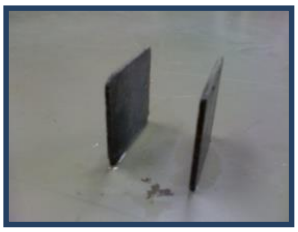

(a)

(b)

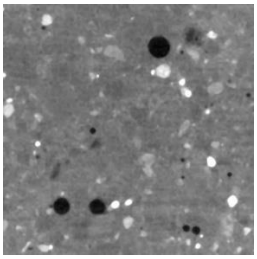

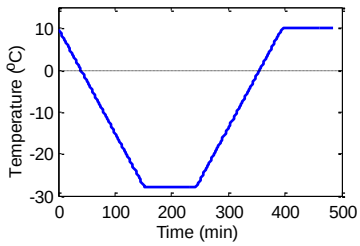

(c) (d)

Fig. 3.9 Outline of the experiment (a) 40 x 40 x 2mm cut specimens; (b) sealed specimens; (c) X-ray CT scanning (6.2x6.2mm)

Reasonable parameters are chosen for the calculation model (see Table 3.2). The critical radius (r_0, the radius between empty pores and pores filled with water according to Fig. 3.3) can also be estimated using the empirical pore size distribution (Gong et al. 2014), and for the macro pores (r>10μm), the estimation formula is (Shimomura et al, 1992):

$$v(r) = V(\infty) \cdot B \cdot C \cdot r^{C-1} \cdot \exp(-B \cdot r^{C}) \tag{3.27}$$

where $v(r)$ is the density of pore volume of concrete or mortar, $V(\infty)$is the total pore volume of unit concrete, r is the radius of pore (m), B and C are the parameters depending on the water cement ratio w/c. If w/c=0.5, the empirical values were given as $V(\infty)$=0.015, B=12000, and C=1.2 (Takewaka et al, 2003). The estimated r_0 is 2×10^{-4}m, which is quite close to the value calculated based on the information in Sicat et al.'s paper (2013), which is 1.7×10^{-4}m. Therefore, the empirical estimation is reliable and easier to be applied to other cases.

Table 3.1 Parameters by experimental measurements

Type (w/c)	Mortar (0.5)
Mix proportion by weight (water: cement: aggregate)	1:2:6
Water saturated (vacuum saturated)	0.228 g/cc (0.238g/cc)
Real water saturation (compared with vacuum saturation)	0.958
Critical radius r_0 (by X-ray CT scanning)	1.7×10^{-4}m
Lowest temperature	-28°C
Cooling rate (also heating)	15 °C/h
Elastic modulus of concrete material E (measured)	34 GPa

Table 3.2 Parameters by empirical estimation

Saturated permeability (undamaged) k_0	10^{-21}m^2
Viscosity of water η (Coussy, 2005)	$2.88\times10^{-5}\exp[509.53/(123.15+T)]$Pa·s
Poisson's ratio of concrete material v	0.2
Bulk modulus of porous body $K_p=E/[3(1-2v)]$	18.9 GPa
Bulk modulus of ice crystal K_C	8.8 GPa
Bulk modulus of liquid water K_L	2.2 GPa
Critical radius r_0 (by empirical equations)	2×10^{-4}m
Equivalent r_E	6×10^{-4}m
Equivalent R_E	0.0028m

Adopting the parameters listed in Table 3.1 and Table 3.2 to the proposed model, the three kinds of pore pressure can be calculated (Fig. 3.10). The crystallization and cryosuction pressures are always coexisted and the sum of two pressures are always less than or equal to zero. The hydraulic pressure is closely related to the permeability (k_0), for the first freeze/thaw cycle, the permeability of undamaged material can be assumed, which is around 10^{-21}m^2 according to Valenza and Scherer's beam-bending test (2004). Thus, for closed test without water uptake, the hydraulic pressure will reach the maximum value during first FTC, and then reduce gradually. The total pressure (sum of three pressures in Fig.

3.10) is still positive, which means expansion occurs at the beginning. In Fig. 3.10, the crystallization pressure and cryosuction pressure are calculated by Eq. (3.26) and Eq. (3.24). The hydraulic pressure is calculated by Eq. (3.11). The basic characters of hydraulic pressure in Fig. 3.10 is in agreement with the discussion of Fig. 3.4.

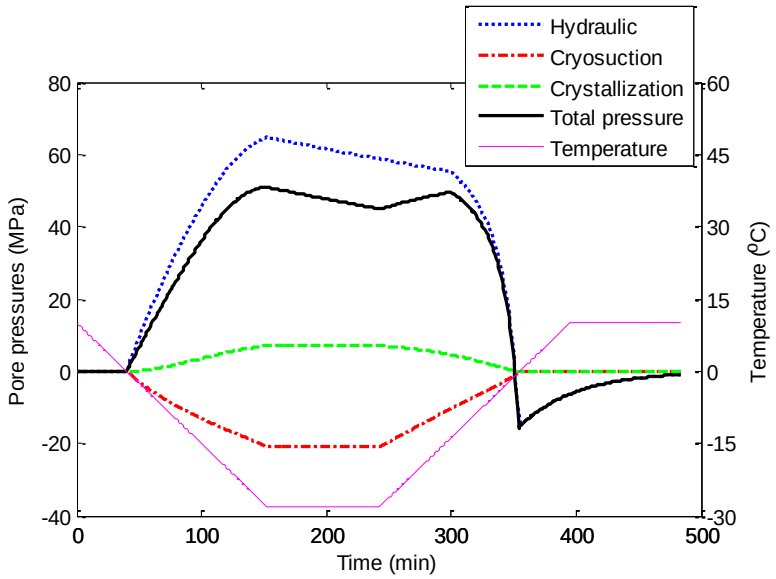

Fig. 3.10 Simulated hydraulic, crystallization and cryosuction pressures

It is difficult to measure the pore pressure in cementitious materials directly, however, the measured strain can be used to verify the model sufficiently, because the total deformation directly results from the total internal forces. More precisely, the stress-strain relationship of the porous body is nonlinear under the high pressure condition, and the plastic deformation was also observed during the experiment as seen in Fig. 3.11. The detailed stress-strain relation under cyclic freeze thaw has been discussed in previous work (Gong et al. 2013). The plastic deformation is mainly shown as the residual strain, but for the peak strain of each cycle, it is still almost linear to the stress level. Therefore, in order to focus on the hydraulic model proposed in this study, a simple stress-strain relation is assumed. Then according to the poroelastic theory, the one-dimensional strain should be:

$$\varepsilon_x = \left(\frac{b}{3K_p}\right)\left(p_h + p_l + p_c\right) \tag{3.28}$$

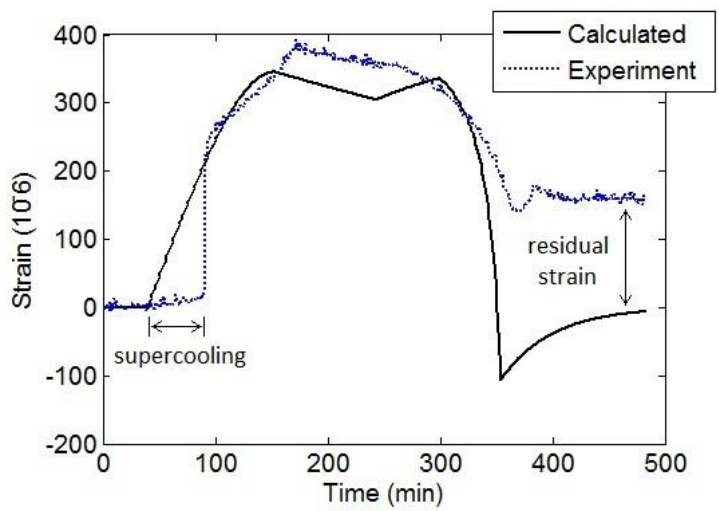

Fig. 3.11 Calculated strain and experimental test (first cycle, $k_0=10^{-21}m^2$)

From Fig. 3.11, it can be seen that the estimated strain matches experimental measurements well. The difference between the nucleation temperatures is because the nucleating agent (metaldehyde) was used in Sun's test (where we took the ice amount information from). While in our test, the super cooling effect existed because nucleating agent was not used. Although the freezing point of bulk water should be at 0°C, if the water is too pure and lack of nucleating particles, the freezing point can still drop below 0°C, such as -8°C in our test. However, this difference does not affect the stress level as temperature continues to decrease. Another difference in Fig. 3.11 is the residual strain resulting from the plastic deformation, which is just a response of the material and thus ignored in this model. Here it should be emphasized that the main purpose of this work is to develop the stress model which can express both the self-compaction self-compression effect and pressure release effect, further to describe the deformation tendency in closed condition for moisture. In order to make the model simple, the stress model is still based on poroelastic theories, although plastic deformation actually exists during the test. And also, since the strain is usually within a few hundreds of microns, there is no big difference between stress estimated by elastic model and plastic model. If only concerning the plastic deformation as a "response" of the material, this materials property can be discussed separately, like author's previous work (Gong, et al. 2013). Therefore, the influence of the plastic behavior is not taken into consideration in this model.

As discussed at the beginning, once the moisture content is constant, the crystallization pressure and cryosuction pressure only depend on the pore size distribution of micro pores(r<100nm), which has been observed unchanged within 3 cycles in Sun's test (2010b). Thus, these two kinds of pressures can be assumed unchanged in the following cycles. Then we only need to focus on the hydraulic pressure. From Eq. (3.11), the three most important factors are cooling rate, saturation degree and permeability. Cooling rate is set manually and kept constant during the test. The change of saturation degree can be also neglected (even a residual strain of 500μ is corresponding to 0.1% volume increase of empty space). Therefore, the reduction of hydraulic pressure mainly results from the change of permeability. Actually previous studies also observed permeability increase by frost damage (Yang et al. 2006). This increment of permeability or reduction of hydraulic pressure is mainly due to the occurrence of micro cracks during the early freeze-thaw cycles, which might change the micro structure in mortar although the pore size distribution might still be unchanged. Thus, the hydraulic pressure would be continuously reduced in the latter cycles.

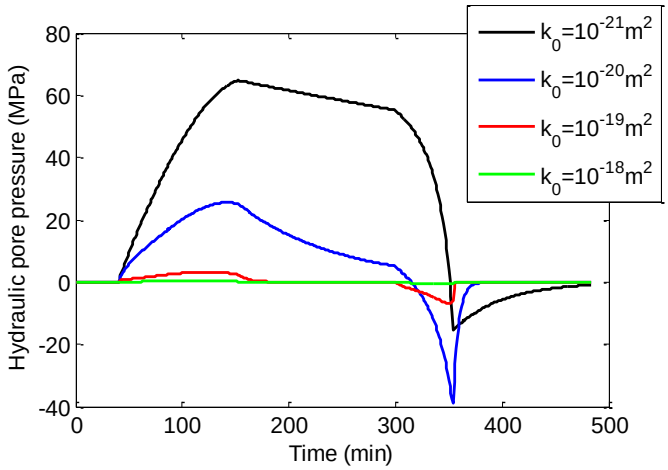

Fig. 3.12 Calculated hydraulic pore pressure with different permeability

Then by increasing the permeability, the reduction of hydraulic pore pressure can be calculated (Fig. 3.12). It should be noticed that in reality, negative hydraulic pressure cannot reach -40MPa, because liquid water has good capability for compression but not tension. Still here, in order to reduce the complexity of the model, this aspect is not considered.

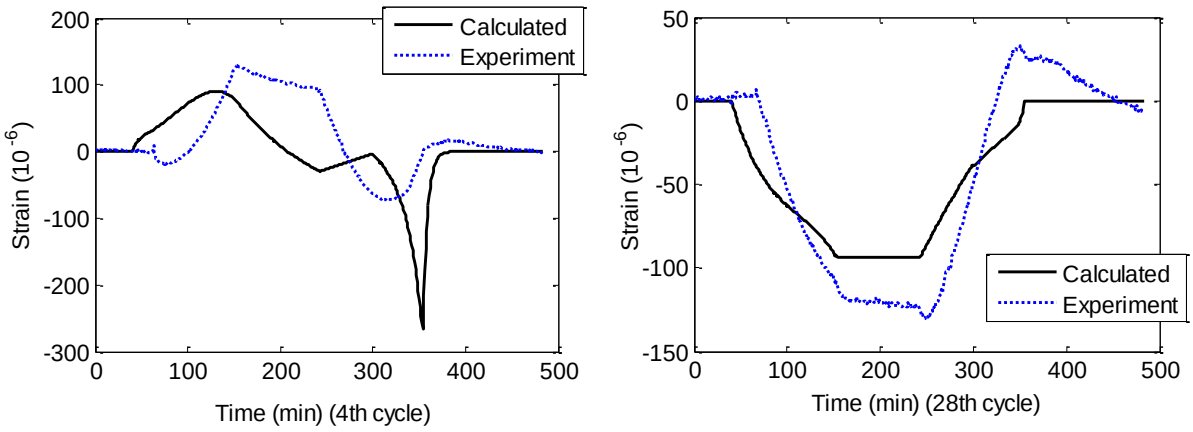

(a) (b)

Fig. 3.13 Calculated and experimental strain (a) 4th cycle, k_0=10^{-20}m^2 (b) 28th cycle, k_0=10^{-18}m^2

Fig. 3.13 shows the comparison between estimated strain and measured strain. The 4th and 28th cycle are chosen to show the typical change of the strain behavior, which are corresponding to the permeability of 10^{-20}m^2 and 10^{-18}m^2, respectively. Although it is difficult to measure the permeability during the test, the above values of permeability can be estimated based on the following arguments: first it is proved that the permeability change is the reason of the reverse phenomenon in the test, and it is also qualitatively known that the permeability will increase due to frost damage (Yang et al. 2006). Therefore a proper value of permeability should be existed that can match the observed behavior best. Together with Fig. 3.11, three kinds of typical strain behavior are shown: State 1: always expansion dominant; State 2: change from expansion to contraction; and State 3: always contraction dominant. Actually State 2 is a transition state between State 1 and 3, and State 3 is a final steady state in the closed test.

3.6 Parametric analysis

According to the comparison and discussion above, the reliability of the proposed model can be verified, then deeper discussions are able to be made. The most affective parameters are cooling rate, saturation degree and the permeability. Among three factors, the cooling rate is certain and controlled manually; the saturation degree is considered constant in closed test, but it will increase in the open test. Finally, the change of permeability is due to the damage caused by hydraulic pressure, and at the same time, the hydraulic pressure will decrease if permeability becomes larger, so an equilibrium steady state can be achieved at last.

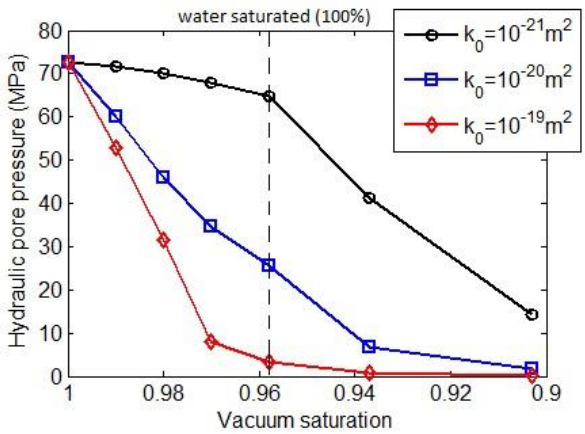

Fig. 3.14 Hydraulic pore pressure (peak value) change with vacuum saturation degree (cooling rate=15°C/h)

Setting the cooling rate as 15°C/h, the hydraulic pore pressure (maximum value) can be obtained regarding the vacuum saturation degree, and for each level of permeability (Fig. 3.14). It is certain that the peak pressure would decrease as saturation degree decreases, and also as permeability increases. The effect of permeability becomes less significant if S_r is closed to 100%. It is because once all the empty spaces are filled up, the water flow and pressure release will stop so that the permeability has no effect on the stress. Therefore, in the closed test, we can observe a big changing tendency from expansion to contraction due to the permeability change. But in the open test, the saturation degree will increase gradually due to the water uptake. For example, if S_r=99%, the permeability change would not reduce the hydraulic pressure effectively, then there is always expansion in the open test. It is also easy to understand that higher cooling rate will result in higher hydraulic pressure, as shown in Fig. 3.15. And for the 95.8% saturation, the permeability has a great effect on the calculated pressure.

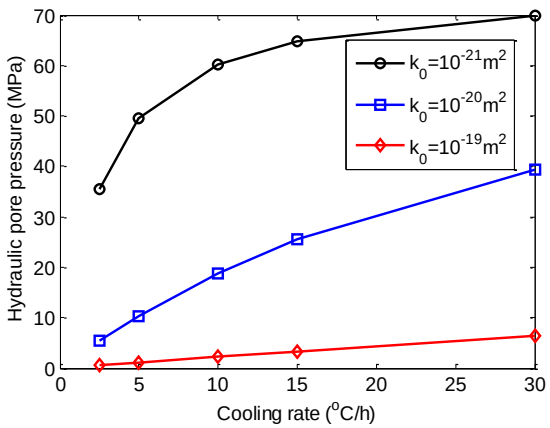

Fig. 3.15 Hydraulic pore pressure change with cooling rate (S_r=95.8%)

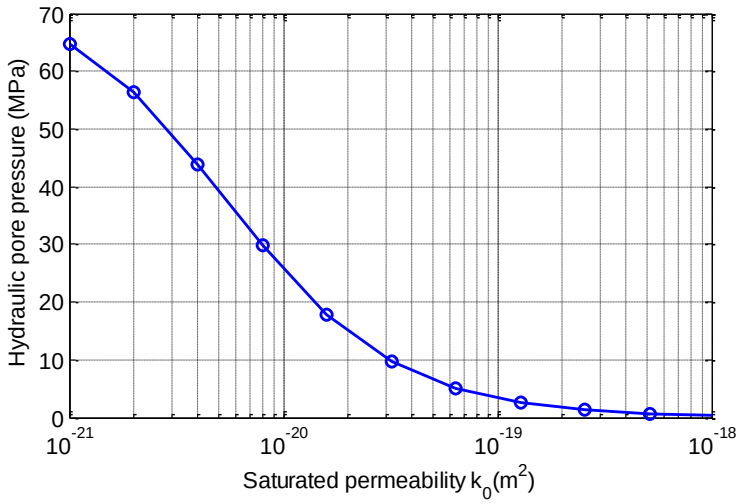

Fig. 3.16 Hydraulic pore pressure reduction as permeability increases (cooling rate=15°C/h, S_r=95.8%)

The permeability is a very important factor for concrete durability. Previous study only discussed the permeability increase qualitatively (Yang et al. 2006) and indirectly (by testing the water absorption speed). However, there are only few direct experimental measurements on it. One reason is that the damage is difficult to evaluate under different frost conditions. And also the permeability itself is not easy to be measured for concrete materials. Here the proposed model can provide a "back analysis" way to evaluate the permeability change. For example, Fig. 3.16 shows peak value of the hydraulic pore pressure depending on permeability, which will decrease if the permeability increases due to damage. Then once the magnitude of hydraulic pressure can be estimated according to the measured deformation, it is also possible to calculate the change of permeability accordingly. Considering the fact that the permeability of concrete materials are usually difficult to measure, and also the permeability increment by frost damage is also a crucial problem for concrete durability, it is much more convenient to apply this model to predict the permeability change by frost damage. The model does not need additional test and can be applied to any environmental conditions. However, if making this model to a testing method, more experimental verifications are needed, which will be conducted in the future studies.

3.7 Conclusions of this chapter

In this chapter, the internal stress analysis has been conducted for the concrete materials under freeze-thaw cycles, several conclusions can be drawn:

(1) A comprehensive hydraulic pressure model is proposed, trying to cover all the existing main mechanisms. The poromechanical rules and Darcy's law are combined to calculate the hydraulic pressure, which becomes a half static and half dynamic force. The hydraulic pressure is closely depending on the permeability of the material, and might decrease gradually at the number of freeze thaw cycles increases. The total pressure is the combination of three pressures (hydraulic, crystallization and cryosuction), which will be positive at the beginning but convert to be negative later. This mechanism explains the reverse phenomenon of the strain during test with closed moisture condition.

(2) The experimental measurements are used to verify the reliability of the proposed model. Poroelastic relation is assumed to estimate the strain based on the calculated total pressure, and the estimated strain is in good agreement with experimental data.

(3) The effect of the main parameters on the calculated results is also discussed. The saturation degree plays a crucial role in the super high saturation region (higher than 96%), which makes the reverse phenomenon (from expansion to contraction as the No. of freeze-thaw cycles increases) only happens in test with closed moisture condition but not in open condition. And at last, the permeability change is a result of frost damage, but at the same time, the increased permeability will help to reduce the stress level, and finally the system will achieve an equilibrium steady state.

(4) The relationship between stress level and permeability revealed by this model can also provide a possible way to evaluate the durability problem under a given environmental condition. That is, after a certain number of freeze thaw cycles, we can estimate the permeability according to the strain behavior during that cycle. This quick method is convenient, based on the same specimen, and the permeability can be tracked during the entire test. But the reliability needs further investigation (for example, by comparing with direct permeability measurements), which will be conducted in the further work.

REFERENCES

Cai, H., and Liu, X. (1998). "Freeze-thaw durability of concrete: ice formation process in pores." *Cement and Concrete Research*, 28(9), 1281-1287.

Coussy, O., (2004), "Poromechanics", Wiley, West Sussex, England.

Coussy, O., (2005), "Poromechanics of freezing materials", Journal of the Mechanics and Physics of Solids, 53, 1689-1718.

Coussy, O. and Monteiro, P.J.M., (2009), "Errata to "Poroelastic model for concrete exposed to freezing temperatures" [Cement and Concrete Research 38 40-48]", Cement and Concrete Research, 39, 371-372.

Gong, F., Zhang, D., Sicat, E. and Ueda, T. (2014), "Empirical estimation of pore size distribution in cement, mortar and concrete" Journal of Materials in Civil Engineering, Vol. 26, No. 7, pp. 04014023-1-11

Johannesson, B., (2010). "Dimensional and ice content changes of hardened concrete at different freezing and thawing temperatures" Cement and Concrete Composite, 32: 73-83.

Power, T. C., (1949), "The air requirement of frost-resistant concrete", Proc. Highway Res. Board, 29, 184-211.

Scherer, G.W. and Valenza II, J.J. (2005). "Mechanism of Frost Damage." In: Skalny, J. and Young, F. Eds. *Materials Science of Concrete Vol. VII*: American Ceramic Society

Shimomura, T. and Ozawa, K. (1992), "Analysis of water movement in concrete based on micro pore structure model." Proceedings of JCI, Vol. 14, No. 1, 631-636. (Japanese)

Sicat, E., Gong, F., Zhang, D. and Ueda, T., (2013). "Change of the Coefficient of Thermal Expansion of Mortar Due to Damage by Freeze Thaw Cycles." Journal of Advanced Concrete Technology, Vol. 11, 333-346.

Sun, Z. and Scherer, G.W. (2010a), "Effect of air voids on salt scaling and internal freezing." Cement and Concrete Research, 40, 260-270.

Sun, Z. and Scherer, G.W. (2010b), "Pore size and shape in mortar by thermoporometry." Cement and Concrete Research, 40, 740-751.

Takewaka, K., Yamaguchi, T. and Maeda, S., (2003), "Simulation model for deterioration of concrete structures due to chloride attack" Journal of Advanced Concrete Technology, 1: 139-146.

Valenza II, J.J. and Scherer, G.W. (2004), “Measuring permeability of rigid materials by a beam-bending method: V, Isotropic rectangular plates of cement paste” J. Am. Ceram. Soc., 87 (10) 1927-1931.

Van Genuchten, M.Th. (1980), “A closed-form equation for predicting the hydraulic conductivity of unsaturated soils” Soil Sci. Soc. Am. J., 44, 892-898.

Yang, Z., Weiss, W.J. and Olek, J. (2006), “Water transport in concrete damaged by tensile loading and freeze-thaw cycling.” Journal of Materials in Civil Engineering, Vol. 18, No. 3, 424-434.

CHAPTER 4

4. Mechanical Properties at Low Temperatures

4.1 Multi-phase composite

The theories of multi-phase composite will be used to estimate the effective elastic modulus for concrete containing different amount of air, liquid water and ice. The well-known Hashin-Shtrikman model (1963) could give the highest lower bound and lowest upper bound for a general *n*-phase composite, but it didn't take the shape and distribution of each phase into consideration. The following researchers found that it is more proper to regard the multi-phase composite as an original materials with different phases of inclusions, and the inclusion can be in different kinds of shapes. Among those models, the self-consistent method by Berryman (1980) can be applied to several types of inclusion shape, such as sphere, needle, disk and penny cracks. Based on Berryman's work and Mori-Tanaka's (1973) theory (which calculated the average internal stress in the matrix of a material containing inclusions with transformation strain), Benveniste (1987) provided a new approach to estimate the effective properties of composites. According to Benveniste's model, given the bulk moduli K_i, the shear moduli G_i and the volume faction ϕ_i, where i = 1, 2 represent the matrix material (i = 1) and the inclusion phase (i = 2), and also $\phi_1 + \phi_2 = 1$, then the effective moduli are calculated as:

$$\begin{cases} K^* = K_1 - \dfrac{\phi_2 \cdot P}{1-\phi_2+\phi_2 \cdot P}(K_1 - K_2) \\ G^* = G_1 - \dfrac{\phi_2 \cdot Q}{1-\phi_2+\phi_2 \cdot Q}(G_1 - G_2) \end{cases} \tag{4.1}$$

where P and Q are the coefficients related elastic properties of two phase and the shape of inclusions, which were given in the literature (Berryman, 1980). For the pores of concrete materials, penny cracks is the most suitable morphology (Li and Wang, 2007), so the expression of P and Q are:

$$\begin{cases} P = \dfrac{K_1 + 4G_2/3}{K_2 + 4G_2/3 + \pi\alpha\beta_1} \\ Q = \dfrac{1}{5}\left(1 + \dfrac{8G_1}{4G_2 + \pi\alpha(G_1 + 2\beta_1)} + 2\dfrac{K_2 + 2G_2/3 + 2G_1/3}{K_2 + 4G_2/3 + \pi\alpha\beta_1}\right) \end{cases} \tag{4.2}$$

where $\beta_1 = G_1[(3K_1+G_1)/(3K_1+4G_1)]$; α (between 0 and 1) is the equivalent aspect ratio reflecting the level of stress concentration, which has different values for different kinds of inclusions.

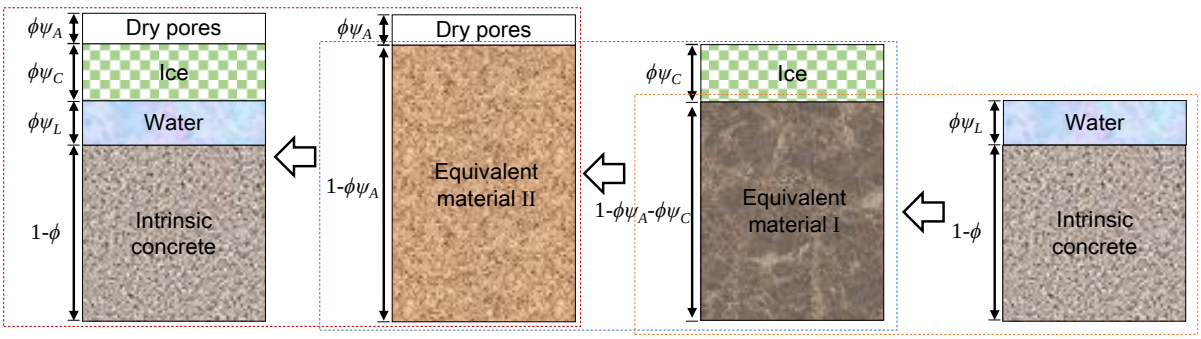

Fig. 4.1 The idea of composition

According to micromechanics, the pores in concrete material can be divided into two categories:

the entrained or entrapped air, which are thought geometrically sphere; and the capillary and gel pores, whose geometry are usually ellipse, disk and penny cracks. Previous studies found that due to stress concentration, the effect of inclusion phase in non-spherical pores is much greater than that in spherical pores on the elastic properties (Yaman et al., 2002a; Stora et al., 2006). In addition, once the capillary and gel pores are occupied by liquid water or ice, the stress concentration will be deduced compared to dry cases. Since the formed ice will be embedded into the pore system tightly, the stress concentration in ice-filled pores could be negligible (α_C=1). The liquid water has much smaller bulk modulus than ice and negligible shear capacity, so its aspect ratio should be much smaller than ice but slightly bigger than dry pores. In this model, α_L=0.15 and α_A=0.12 is chosen according to the test data of Yaman et al. (2002a).

Since Benveniste's model is limited to two-phase composite, the ideal of decomposition (Wang and Li, 2007) is needed to change the four-phase (intrinsic concrete, liquid water, ice and air) system into a three-stage but two-phase problem, as illustrated in Fig. 4.1. The order of composition has six kinds of combination for this problem, but it will not affect the final result much (which will be discussed later), so Fig. 4.1 is just showing one example. The equivalent material I is made up with intrinsic concrete and water; the equivalent material II is made up with equivalent material I and ice; and finally, the real system is composed by equivalent material II and dry air. If following the order indicated in Fig. 4.1, the effective moduli of Material I is:

$$\begin{cases} K_{\mathrm{I}} = K_S - \dfrac{\phi_L \cdot P_L}{1-\phi_L+\phi_L \cdot P_L}(K_S - K_L) \\ G_{\mathrm{I}} = G_S - \dfrac{\phi_L \cdot Q_L}{1-\phi_L+\phi_L \cdot Q_L}(G_S - G_L) \end{cases} \tag{4.3}$$

Then the effective moduli of Material II is:

$$\begin{cases} K_{\mathrm{II}} = K_{\mathrm{I}} - \dfrac{\phi_C \cdot P_C}{1-\phi_C+\phi_C \cdot P_C}(K_{\mathrm{I}} - K_C) \\ G_{\mathrm{II}} = G_{\mathrm{I}} - \dfrac{\phi_C \cdot Q_C}{1-\phi_C+\phi_C \cdot Q_C}(G_{\mathrm{I}} - G_C) \end{cases} \tag{4.4}$$

Finally the effective moduli of concrete material is:

$$\begin{cases} K^* = K_{\mathrm{II}} - \dfrac{\phi_A \cdot P_A}{1-\phi_A+\phi_A \cdot P_A}(K_{\mathrm{II}} - K_A) \\ G^* = G_{\mathrm{II}} - \dfrac{\phi_A \cdot Q_A}{1-\phi_A+\phi_A \cdot Q_A}(G_{\mathrm{II}} - G_A) \end{cases} \tag{4.5}$$

The elastic properties of each component phase are shown in Table 4.1. While for the intrinsic concrete phase, the elastic properties should vary depending on its mix proportion, such as the water to cement ratio, the amount of aggregates and so on. Here a particular group of parameters (Yaman et al., 2002a) are given for the comparison purpose. During the three stages of composition, the parameters of the basic material and inclusion phase in each step should be adjusted accordingly, as shown in Table 4.2, which corresponding to the composition order in Fig. 4.1. Then after getting K^* and G^*, the effective elastic modulus and Poisson's ratio of the whole material can be obtained based on the theorem of elastic mechanics:

$$E^* = \frac{9K^*G^*}{3K^*+G^*} \tag{4.6}$$

$$\nu^* = \frac{1}{2}\left(1 - \frac{1}{1/3 + K^*/G^*}\right) \tag{4.7}$$

Table 4.1. The elastic properties of each moisture phase

	Intrinsic concrete (S)	Ice crystal (C)	Liquid water (L)	Dry pores (A)
K (GPa)	27.91	8.8	2.2	0
G (GPa)	18.45	4.06	0	0
E (GPa)	45.35	10.56	-	-
ν	0.229	0.3	-	-

Table 4.2. Parameters of each composition step

	Liquid water (L)	Ice crystal (C)	Dry pores (A)
P	$\frac{K_S}{K_L + \pi\alpha_L\beta_S}$	$\frac{K_I + 4G_C/3}{K_C + 4G_C/3 + \pi\alpha_C\beta_I}$	$\frac{K_{II}}{\pi\alpha_A\beta_{II}}$
Q	$\frac{1}{5}\left(1 + \frac{8G_S}{\pi\alpha_L(G_S + 2\beta_L)} + 2\frac{K_L + \frac{2}{3}G_S}{K_L + \pi\alpha_L\beta_S}\right)$	$\frac{1}{5}\left(1 + \frac{8G_I}{4G_C + \pi\alpha_C(G_I + 2\beta_I)} + 2\frac{K_C + \frac{2}{3}G_C + \frac{2}{3}G_I}{K_C + \frac{4}{3}G_C + \pi\alpha_C\beta_I}\right)$	$\frac{1}{5}\left(1 + \frac{8G_{II}}{\pi\alpha(G_{II} + 2\beta_{II})} + \frac{4G_{II}}{3\pi\alpha_A\beta_{II}}\right)$
β	$\beta_S = G_S\frac{3K_S + G_S}{3K_S + 4G_S}$	$\beta_I = G_I\frac{3K_I + G_I}{3K_I + 4G_I}$	$\beta_{II} = G_{II}\frac{3K_{II} + G_{II}}{3K_{II} + 4G_{II}}$
α	0.15	1.0	0.12
ϕ	$\phi\psi_L/(\phi\psi_L + 1 - \phi)$	$\phi\psi_C/(1 - \phi\psi_A)$	$\phi\psi_A$

There are several sets of order during the composition process. For example, for the unsaturated concrete (three-phase composite) in room temperature, the composition order could be ice to liquid or liquid to ice; and for a four-phase system with air, liquid water and ice, there are six sets of orders. Using the elastic properties in Table 4.1, and taking the maximum value of void ratio (0.25) that concrete material could have, the differences among different composition orders are shown in Fig. 4.2. It can be seen that the differences between different sets of orders are rather negligible compared to the whole range of changing. Therefore, the average values of all the composition orders will be taken as the final predicted results.

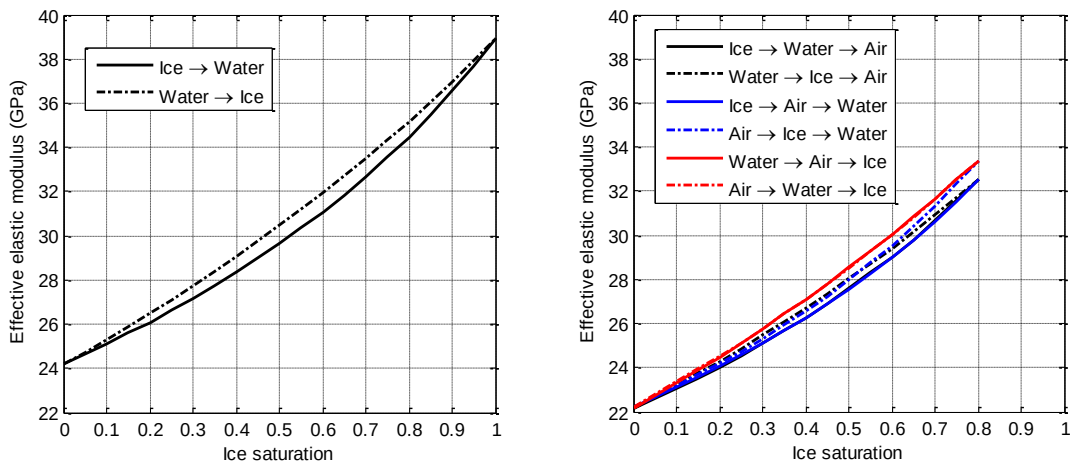

(a) (b)

Fig. 4.2 The effect of the composition order (a) room temperature (b) 80% saturation at freezing temperature

4.2 Experimental verification

In order to make reliable comparison, the value of elastic modulus of intrinsic concrete must be determined properly. Actually the elastic modulus of intrinsic concrete Yaman et al. (2002a) is obtained by elongating the E-ϕ (elastic modulus to void ratio) curve to the vertical axis (ϕ=0), which means the idea elastic modulus if the void ratio is zero (the intrinsic concrete). However, according to the discussion in their later study (Yaman et al., 2002b), the aspect ratio of dry pores (which has a similar meaning as α_A in this paper, but based on different multi-phase composite formulas) is estimated between 0.1 and 0.2, which will make the elastic modulus nonlinear to the void ratio (Wang and Li, 2007), and also the closer to the zero void ratio, the bigger increase in the elastic modulus. Therefore, not only the intrinsic elastic modulus varies with different mix proportion, but also the average value should become bigger than 45.35GPa that indicated in Table 4.1.

Based on Yaman et al.'s data (2002a), since each mix proportion with different void ratio, the elastic modulus and Poisson's ratio at dry and fully saturated conditions are known, and they must share the same values of intrinsic elastic properties. Therefore, by regressing Yaman et al.'s data, the best fitted aspect ratio for dry pores (α_A=0.12) and saturated condition (α_L=0.15) can be determined. And the intrinsic elastic moduli of each mix proportion can also be obtained by the inverse analysis. The details of Yaman et al.'s (2002a) data are shown in Table 4.3, in which the elastic modulus and Poisson's ratio are estimated using the proposed model in Chapter. It can be seen that the estimated values are bigger than the linear extended modulus and average Poisson's ratio. The estimated values in Table 4.3 still need further investigation, which will be conducted in the future.

Table 4.3 Yaman et al.'s data (2002a) and the estimated intrinsic properties

ID	Poisson's ratio		Elastic modulus		Porosity	Intrinsic elastic modulus	Intrinsic Poisson's ratio
	Sat.	Dry	Sat.	Dry			
35-00-L-2	0.252	0.238	40.84	38.43	0.094	52	0.29
40-00-L-2	0.268	0.235	40.78	35.94	0.102	51	0.31
45-00-L-2	0.263	0.221	38.31	33.51	0.131	52	0.31
35-05-L-2	0.251	0.224	37.36	32.92	0.129	52	0.29
35-06-L-2	0.246	0.238	37.47	35.11	0.128	54	0.29
35-12-L-2	0.242	0.22	36.13	31.37	0.211	62	0.32
40-07-L-0	0.26	0.229	37.04	30.61	0.161	54	0.32
40-05-L-0	0.261	0.229	36.81	31.57	0.171	56	0.33
40-05-L-2	0.268	0.219	37.45	29.76	0.159	53	0.33
45-05-L-0	0.253	0.232	35.75	30.93	0.155	52	0.31
40-09-L-2	0.251	0.242	33.99	30.93	0.199	58	0.33
45-05-L-2	0.254	0.223	35.46	29.99	0.17	53	0.32
35-10-L-2	0.256	0.237	32.86	27.1	0.207	54	0.34
50-05-L-0	0.269	0.236	33.79	26.88	0.2	54	0.35
45-09-L-0	0.244	0.217	32.18	27.33	0.208	54	0.31

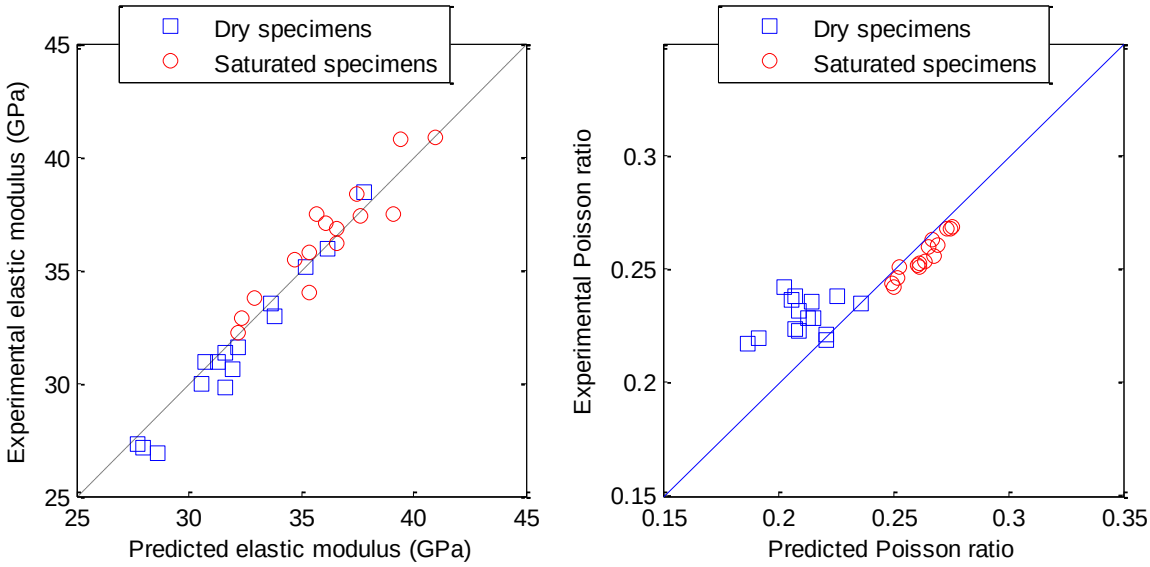

Fig. 4.3 The predicted elastic modulus and Poisson's ratio, with comparison to experimental measurements in Yaman et al. (2002a)

Then using the developed model in this paper, the effective elastic moduli and Poisson's ratio of dry and saturated concrete at room temperature can be predicted, and the elastic moduli are in a good agreement with experimental values (Fig. 4.3). Although there is some difference between in the Poisson's ratio, but considering that this difference will not affect the stiffness and the strengths much, the predicted values are still in an acceptable range.

Table 4.4 Mix proportion and estimated properties

Ref.	W/C	Ψ_{CP}	Void ratio[1]	Intrinsic elastic modulus (GPa)[2]
Rostasy and Wiedemann, 1980	0.54	0.504	0.22	44.4
Lee et al., 1988a,b	0.48	0.63	0.18	46.7
	0.35	0.624	0.1	49.6

Note: 1. The void ratio is estimated by empirical formulas in Gong et al. (2014).
2. The intrinsic elastic modulus of concrete is estimated inversely based on the saturated concrete at room temperature.

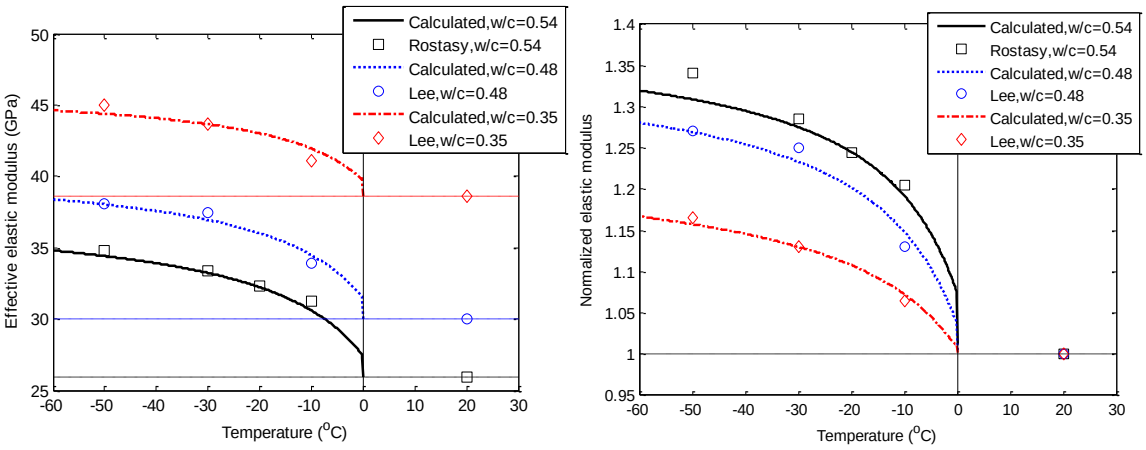

Fig. 4.4 Predicted effective elastic modulus for saturated concrete under freezing, with comparison to previous data

For the prediction under freezing temperatures, the ice content should be estimated first based on

the pore size distribution and the temperature. Either using the theoretical estimation in Chapter 2 or the empirical experimental measurements in Section 3.3, the ice content can be estimated at each freezing temperature. Then if adopting the estimation in Chapter 2, the elastic moduli change regarding temperature can be calculated (Fig. 4.4) for the selected experiments (Rostasy and Wiedemann, 1980; Lee et al., 1988a,b) and the predicted curves match the test data well. The mix proportion of the specimens is listed in Table 4.4. Since there is no comprehensive information about the total void ratio, it must be estimated empirically (Gong et al., 2014), and the brief summary of the estimation method is discussed in Section 5.2.2. The intrinsic elastic modulus is difficult to measure, so here it is estimated inversely from the saturated elastic modulus at room temperatures. Then the effective elastic moduli at different freezing temperature can be predicted and are reliable to be used as inputs for the following RBSM analysis.

4.3 Conclusions of this chapter

This chapter presents the theoretical model for the effective elastic properties of concrete material due to the ice strengthening effect, and the detailed conclusion are as follows:

(1) The theories of multi-phase composites are introduced to explain the macro elastic properties change when ice forms in a highly saturated concrete, in which the stress concentration in pores with different phases of moisture can be taken into consideration.

(2) Based on the existing two-phase theories and the concept of composition, the freezing concrete, which is a four-phase composite, can be composed step by step by a series of two-phase problems. And by regressing of the previous data of dry and water saturated concrete, the proper value for the aspect ratio of pores with different phases of moisture can be determined.

(3) Finally using the proposed model in this chapter, the effective elastic moduli due to ice strengthening effect at different temperatures can be predicted, which are also in a good agreement with experimental data. Therefore, the predicted elastic property change is reliable for the RBSM simulation of the static strengths.

REFERENCES

Benveniste, Y. (1987). "A new approach to the application of Mori-Tanaka's theory in composite materials." *Mechanics of materials*, 6(2), 147-157.

Berryman, J. G. (1980). "Long - wavelength propagation in composite elastic media II. Ellipsoidal inclusions." *The Journal of the Acoustical Society of America*, 68(6), 1820-1831.

Gong, F., Zhang, D., Sicat, E., and Ueda, T. (2014). "Empirical estimation of pore size distribution in cement, mortar, and concrete." *Journal of Materials in Civil Engineering*, 26(7).

Hashin, Z., and Shtrikman, S. (1963). "A variational approach to the theory of the elastic behaviour of multiphase materials." *Journal of the Mechanics and Physics of Solids*, 11(2), 127-140.

Lee, G., Shih, T., and Chang, K. (1988a). "Mechanical properties of concrete at low temperature." *Journal of cold regions engineering*, 2(1), 13-24.

Lee, G., Shih, T., and Chang, K. (1988b). "Mechanical properties of high-strength concrete at low temperature." *Journal of cold regions engineering*, 2(4), 169-178.

Mori, T., and Tanaka, K. (1973). "Average stress in matrix and average elastic energy of materials with misfitting inclusions." *Acta metallurgica*, 21(5), 571-574.

Rostasy, F., and Wiedemann, G. (1980). "Stress-strain-behaviour of concrete at extremely low

temperature." *Cement and Concrete Research*, 10(4), 565-572.

Stora, E., He, Q.-C., and Bary, B. (2006). "Influence of inclusion shapes on the effective linear elastic properties of hardened cement pastes." *Cement and concrete research*, 36(7), 1330-1344.

Wang, H., and Li, Q. (2007). "Prediction of elastic modulus and Poisson's ratio for unsaturated concrete." *International Journal of Solids and Structures*, 44(5), 1370-1379.

Yaman, I., Aktan, H., and Hearn, N. (2002). "Active and non-active porosity in concrete part II: evaluation of existing models." *Materials and Structures*, 35(2), 110-116.

Yaman, I., Hearn, N., and Aktan, H. (2002). "Active and non-active porosity in concrete part I: experimental evidence." *Materials and Structures*, 35(2), 102-109.

CHAPTER 5

5. Constitutive Laws for RBSM

The Rigid Body Spring Model (RBSM) is a discrete numerical analysis method, which was first developed by Kawai (1977). Unlike the continuum methods such as Finite Element Method or Finite Difference Method, RBSM is a more proper way to simulate splitting and cracking in cement-based materials like mortar and concrete. And also compared to other discrete method like Distinct Element Method, RBSM is more suitable for small deformation and tiny cracks which often occurs in concrete structures.

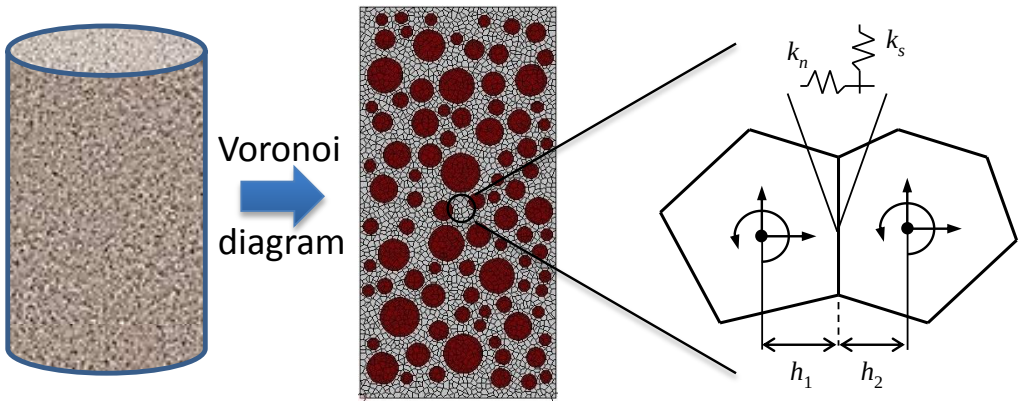

Fig. 5.1 Voronoi geometry, elements, degree of freedom and springs

The concrete to be simulated is divided into polyhedron elements, and the mesh is arranged randomly using a Voronoi diagram. Each Voronoi cell represents a mortar or aggregate element in the model. For two adjacent elements, there are two springs connecting them: normal spring and shear spring, which are placed at the boundary of the elements (see Fig. 5.1). Each element has two translational and one rotational degree of freedom at the center of gravity. The normal and shear moduli are calculated by assuming a plane stress condition as follows (Nagai et al. 2004):

$$\begin{aligned} k_n &= E/(1-\nu^2) \\ k_s &= E/(1+\nu) \end{aligned} \tag{5.1}$$

where k_n and k_s are the stiffness of normal and shear spring; E and ν are the elastic modulus and Poisson's ratio of the element (either mortar or aggregate), respectively. In case of the springs on the mortar-aggregate interface, the stiffness is given as a weighted average mortar and aggregate element:

$$\begin{aligned} k_n &= (k_{n1}h_1 + k_{n2}h_2)/(h_1+h_2) \\ k_s &= (k_{s1}h_1 + k_{s2}h_2)/(h_1+h_2) \end{aligned} \tag{5.2}$$

where the subscripts 1 and 2 represent the mortar and aggregate elements respectively, and h is the length of the perpendicular line from the center of gravity of element to the boundary. The stress-strain relationship of the normal spring will adopt a linear tension-softening curve, and a normal distribution was assumed for the tensile strength to increase the heterogeneous performance (Nagai et al, 2004):

$$f\left(f_t\right)=\frac{1}{\sqrt{2\pi}s}\exp\left[-\frac{\left(f_t-\mu\right)^2}{2s^2}\right] \tag{5.3}$$
$$s=-0.2\mu+1.5$$

where f_t is the tensile strength of the element, and for $f_t<0$, set $f_t=0$; μ is the average value of f_t; and s is the standard derivation. For the shear spring of porous body, the following criterion is adopted (Kosaka et al. 1975):

$$\tau_{\max}=\pm\left(0.11f_t^3\left(-\sigma+f_t\right)^{0.6}+f_t\right) \qquad \left(\sigma\le f_t\right) \tag{5.4}$$

where σ is the normal stress. And for the interface between mortar and aggregate, the shear criterion follows:

$$\tau_{\max}=\pm\left(-\sigma\tan\varphi+c\right) \tag{5.5}$$

where φ and c are constant values. When facture occurs in the normal spring, the shear strength should also reduce as the crack opening width increases.

5.1 Deformation under pore pressures

According to the existing theories of frost damage, there are mainly three kinds of pressures responsible to the material deformation, that is, the hydraulic pressure (p_h) due to ice volume expansion (Powers, 1949; Coussy and Monterio, 2008; Errata, 2009), the crystallization (p_c) and cryosuction (p_l) pressures due to the thermodynamic equilibrium between ice crystal and unfrozen water (Scherer, 2005). Among those three pressures, the hydraulic pressure itself also depends on the material deformation, which needs to be considered in a nonlinear constitutive model; crystallization and cryosuction pressures only depend on the pore structure and temperature, which can be applied as a boundary condition to the mechanical model at the last.

5.1.1 Mechanical model

The constitutive relation for the normal spring under the cyclic freezing/thawing stress has been discussed in the authors' previous paper (Gong et al, 2013) as shown in Fig. 5.2. Different from the external loading, the hydraulic stress during freeze/thaw cycle itself is also depending on the material's deformation. For example, in Fig. 5.2 (b), after pore stress exceeds the tensile strength ($f_t^{(1)}$), the final equilibrium can still be achieved at $\varepsilon_{ta}^{(1)}$. This is because as the porous body continuously expands, the hydraulic pressure will decrease linearly as in Fig. 5.2 (a) (if assuming an elastic behavior for ice and water). Therefore, the stress-strain condition under each certain freezing condition is the intersection point of Fig. 5.2 (a) and (b). After each cycle, the vertical axis should be moved rightward, which means an initialization of the strain but with degraded properties (residual tensile strength and elastic modulus), thus the damage accumulation in multiple FTCs can be modeled. Actually there should be a stress reduction in the softening part of Fig. 5.2 (b) if under cyclic loadings (like frost cycles or fatigue cycles), as discussed later in Fig. 5.8. However, if considering the small numbers of FTC cycles, the stress drop might be ignored for the simulation convenience, and it won't affect the damage cumulating due to FTC a lot.

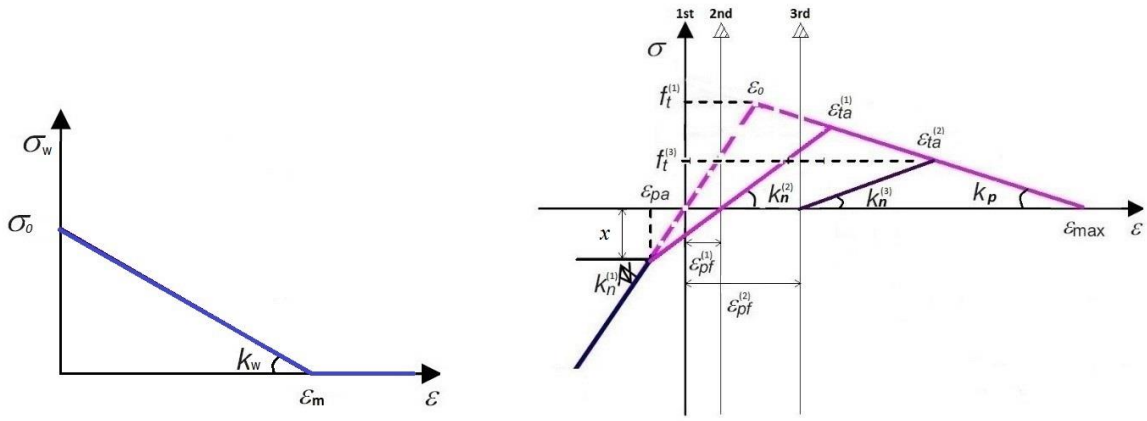

(a) (b)

Figure 5.2 Stress-strain relationship under multiple FTCs

The softening part of the stress-strain curve in Fig. 5.2 (b) is simply taken as a linear relation, with minimum number of parameters that need to be assumed ($k_n^{(1)}$, $f_t^{(1)}$ and ε_{max}). This relation can ensure good simulation under external loads such as compression, tension and bending. However, previous researches on concrete deformation under FTC showed a large variance (Hasan et al., 2004; Sun and Scherer, 2010a; Sicat et al., 2013; Kaufman, 2004; Johannesson, 2010), which might be because different materials and test procedures were used. In order to make a comprehensive model which can simulate most of those results, the input variables are separated into two groups: (1) the environmental variables, which finally lead to the calculated pore pressures; (2) the material's behavior, such as the magnitude of residual deformation ($\varepsilon_{pf}^{(n)}$) caused by a certain level of maximum deformation ($\varepsilon_{ta}^{(n)}$). The calculation of pore pressures will be discussed in the next section, while the differences among material's responses can be reflected by ε_{pa}, that is, once the maximum deformation ($\varepsilon_{ta}^{(n)}$) is given, how much residual impact ($\varepsilon_{pf}^{(n)}$) will be caused is mainly depending on the value of ε_{pa}. Inversely, the value of ε_{pa} can be determined according to $\varepsilon_{ta}^{(1)}$and $\varepsilon_{pf}^{(1)}$ from the first cycle of each particular FTC test. For example, from Fig. 5.2 (b),

$$k_n^{(1)} = \frac{x}{\varepsilon_{pa}} = \frac{f_t^{(1)}}{\varepsilon_0}$$
$$k_n^{(2)} = \frac{x}{\varepsilon_{pa} + \varepsilon_{pf}^{(1)}} = \frac{f_t^{(1)} - k_p(\varepsilon_{ta}^{(1)} - \varepsilon_0)}{\varepsilon_{ta}^{(1)} - \varepsilon_{pf}^{(1)}} \tag{5.6}$$

where k_p is the slope of the softening curve (absolute value) and ε_0 is the strain corresponding to the tensile strength (usually equals to 150μ). Then combining the two equations above and eliminate x, there is,

$$\varepsilon_{pa} = \frac{\varepsilon_0 \varepsilon_{pf}^{(1)}[f_t^{(1)} - k_p(\varepsilon_{ta}^{(1)} - \varepsilon_0)]}{f_t^{(1)}(\varepsilon_{ta}^{(1)} - \varepsilon_{pf}^{(1)}) - \varepsilon_0[f_t^{(1)} - k_p(\varepsilon_{ta}^{(1)} - \varepsilon_0)]} \tag{5.7}$$

According to Nagai's RBSM model, for an average element size of 2.5mm, ε_{max} is around 12000μ, then k_p will be much smaller compared to k_n. Therefore, $f_t^{(1)}$-$k_p(\varepsilon_{ta}^{(1)}$-$\varepsilon_0)$ can be approximately equal to $f_t^{(1)}$, which means Eq. (5.7) can be simplified as:

$$\varepsilon_{pa} = \frac{\varepsilon_0 \varepsilon_{pf}^{(1)}}{\varepsilon_{ta}^{(1)} - \varepsilon_{pf}^{(1)} - \varepsilon_0} \tag{5.8}$$

From Eq. (5.8), once the maximum strain and residual strain of the first cycle are known from each experiments, ε_{pa} can be estimated (Table 5.1). From Fig. 5.2 (b), ε_{pa} can be also estimated by the residual stiffness ($k_n^{(n+1)}$) and residual strain ($\varepsilon_{pf}^{(n)}$) of a certain cycle n, like Hasan's test (Hasan, 2004; Ueda, 2009).

$$\varepsilon_{pa} = \frac{k_n^{(n+1)} \cdot \varepsilon_{pf}^{(n)}}{k_n^{(1)} - k_n^{(n+1)}} \tag{5.9}$$

Table 5.1. ε_{pa} calculated from different literatures

Ref.	Material	Size (mm)	*w/c*	Peak strain (μ)	Residual strain (μ)	ε_{pa} (μ)
Hasan (2004)	Concrete (cyl)	100×100×200	0.5	-	-	400
Sun (2010a)	Mortar (cyl)	5×5×15	0.55	900	350	131
Sicat (2011)	Mortar	40×40×2	0.5	760	100	34
Kaufmann (2004)	Mortar	25×25×10	0.63	300	80	171
			0.4	625	135	60
Johannesson (2010)	Mortar	20×20×160	0.5	1250	400	86
			0.6	800	250	94

5.1.2 Deformation under freeze-thaw cycles

The stress analysis in Chapter 3 is based on a linear elastic assumption for the porous body, which is more convenient to obtain the basic characteristics of the freezing stress. However, for the constitutive laws in RBSM, the nonlinear stress-strain relation is adopted for the normal spring, thus for the simulation purpose, the hydraulic model (Eq. (3.11)) should be changed accordingly. Then first for a fully saturated concrete material, according to the poromechanical theories, the volume expansion during ice formation $\Delta V/V$ should be balanced by the volume change of each phase:

$$\Delta V / V = \varepsilon_C + \varepsilon_L + \varepsilon_p \tag{5.10}$$

where ε_p, ε_C and ε_L are the volume strain of the porous body, ice and liquid water, respectively. Assume an elastic behavior for ice and water as:

$$\begin{cases} \varepsilon_C = \phi\psi_C \cdot p_h / K_C \\ \varepsilon_L = \phi\psi_L \cdot p_h / K_L \end{cases} \tag{5.11}$$

where p_h is the hydraulic pressure in pores; ϕ is the void ratio; ψ_C is the normalized ice content; ψ_L=1-ψ_C is the liquid water content; K_C and K_L are the bulk moduli of the ice and water, respectively. The pore pressure that in terms of the effective stress (σ_w, which is an average stress on the porous matrix caused by pore pressure) can be expressed as (Coussy, 2005):

$$\sigma_w = b \cdot p_h \tag{5.12}$$

where b=2ϕ/(1+ϕ) is Biot coefficient (Coussy, 2005). Since the volume expansion is in proportion to ice content, which is $\Delta V/V$=0.09$\phi\psi_C$, and also the volume strain of porous body approximately equals to 3 times of the one-dimensional strain under uniform expansion (ε_p=3ε_x), then Eq. (5.10) becomes:

$$0.09\phi\psi_C = \left(\frac{\phi\psi_C}{K_C} + \frac{\phi\psi_L}{K_L}\right) \cdot \frac{\sigma_w}{b} + 3\varepsilon_x \tag{5.13}$$

Eq. (5.13) describes the internal effective stress σ_w in relation to the strain of concrete material (ε_x), therefore, in Fig. 5.2 (a), the value σ_0 can be determined when ε_x=0, which is:

$$\sigma_0 = b \cdot 0.09\phi\psi_C \Big/ \left(\frac{\phi\psi_C}{K_C} + \frac{\phi\psi_L}{K_L}\right) \tag{5.14}$$

Eq. (5.14) is actually the same as Coussy and Monteiro's model (2009) in which the deformation of porous body was neglected. And the stiffness k_w in Fig. 5.2 (a) can be determined from Eq. (5.13):

$$k_w = \frac{3b}{\phi[\psi_C / K_C + \psi_L / K_L]} \tag{5.15}$$

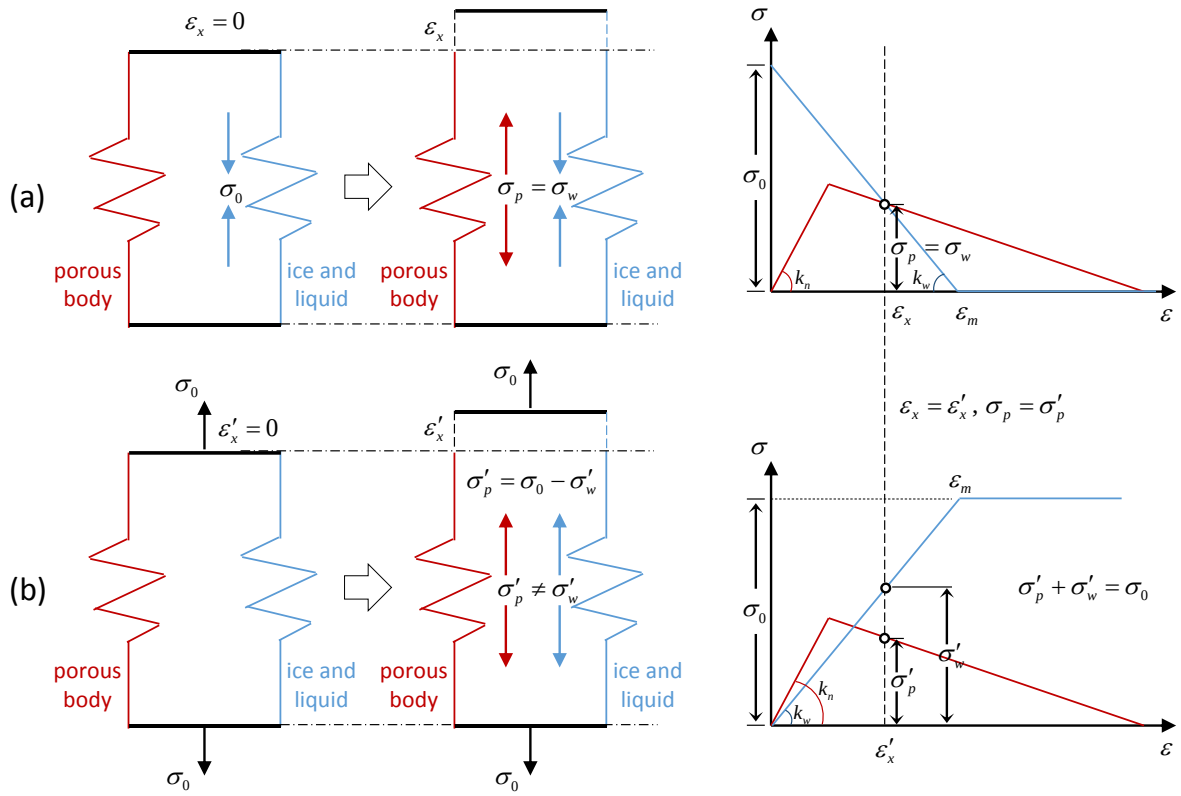

Figure 5.3. Parallel spring system, the internal effective stress can be transformed into an external load on two springs (a) stress σ_0 is generated internally from the ice-water spring (b) stress σ_0 is applied on two springs from outside

The above constitutive laws for both porous body and ice-water (like Eq. (5.13)) show a series relation, in which the total increased volume is balanced by two springs. The series agrees with the physical process but is inconvenient for making the total stiffness matrix, especially for the iteration in the nonlinear analysis. However, the series spring system with input strain can be transformed into the parallel spring system with input stress, which can be proved mathematically. From Fig. 5.3, once the volume increases due to ice formation, an initial effective stress (σ_0) will generate inside the spring of ice and water (like in a pre-compressed condition), then the ice-water spring will start to expand but at

the same time it will be confined by the spring of porous body. As the porous body continues to expand, the pre-stored stress in ice-water spring will release linearly while the stress in the porous body spring will change nonlinearly according to Fig. 5.2 (b), until the two spring stresses reach an equilibrium. Therefore, during this process, the initial stress is applied inside (without external forces), and finally the stresses in two springs must be the same but at opposite signs (porous body is in tension but ice and water are in compression). This model can describe the real physical process well but is not convenient for the numerical simulation, especially when external load (mechanical load) is also applied outside of two springs. As shown in Fig. 5.3, it can be proved mathematically that the final states of spring for porous body are the same when σ_0 is directly applied outside on two springs. Then the spring of ice-water will only act as an aided tool to get the correct status of the porous body, but with less physical meaning. Since the main target is to find the deterioration of the porous body, this transformation has no effect on the porous material and on the contrary, the internal effective stress can be treated as an ordinary external load. In addition, this parallel system can automatically provide a changing load on the porous body. Then the numerical analysis can be conducted by simply adding another stiffness matrix:

$$[\mathrm{K}_p + \mathrm{K}_w]\{u\} = \{F_0\} \tag{5.16}$$

where $[\mathrm{K}_p]$and $[\mathrm{K}_w]$ are the stiffness matrix of the porous body and ice-water system, respectively. And the load boundary condition $\{F_0\}$ can be calculated using $\{\sigma_0\}$:

$$\{F_0\} = [B]^T \{\sigma_0\} \tag{5.17}$$

where $[B]$ is the deformation matrix in RBSM analysis. Since the internal effective stress is a volume stress, it can be considered only applied on the normal spring, then finally the element stiffness matrix would be:

$$k_e = \begin{bmatrix} k_n + k_w & 0 \\ 0 & k_s \end{bmatrix} \tag{5.18}$$

For the partially saturated cases, σ_0 in Fig. 5.2 (a) can be calculated as:

$$\begin{aligned} &0.09\phi\dot{\psi}_C - \frac{A}{V}\cdot\frac{k}{\eta}\cdot\frac{2}{R_E - r_E}p_h = \left(\frac{\phi\psi_C}{K_C} + \frac{\phi\psi_L}{K_L}\right)\cdot\dot{p}_h \\ &\sigma_0 = b\cdot p_h \end{aligned} \tag{5.19}$$

The total internal pressure is the sum of those three pressures, which is $p=p_h+p_l+p_c$, and the total effective stress on the porous body becomes:

$$\sigma = b\cdot(p_h + p_l + p_c) = \sigma_0 + b\cdot p_l + b\cdot p_c \tag{5.20}$$

where p_l and p_c can be calculated by Eq. (3.24) and Eq. (3.25).

5.2 Ice strengthening effect

5.2.1 Ice strengthened constitutive laws

For a saturated concrete material, if the temperature is above zero and there is no ice inside the concrete, before the stress reaches the tensile strength (f_t) of the normal spring, the spring will behave linearly and never get failure; after the strain exceeds the critical value (ε_0) corresponding to the tensile strength, the stress capacity will decrease linearly until the normal spring gets failure, as shown in Fig

5.4 (a). The maximum crack width defined by Nagai et al. (2004) was 0.03mm for mortar and 0.01mm for interface, which corresponding to a maximum tensile strain (ε_{max}) of 12000μ and 4000μ if the average size of element is chosen as 2.5mm. Once ice forms at freezing temperatures, since the ice inside the coarse aggregates is negligible, the elastic modulus will only increase significantly in the mortar elements. Although the stiffness in RBSM will also depend on the effective Poisson's ratio according to Eq. (5.1), but it has rather limited effect compared to elastic modulus and can be assumed constant as 0.18 for mortar conveniently. Then if applying an external load, the effective stiffness would become k_n' and the total tensile strength would increase to f_t', while the critical tensile strain is still assumed as ε_0.

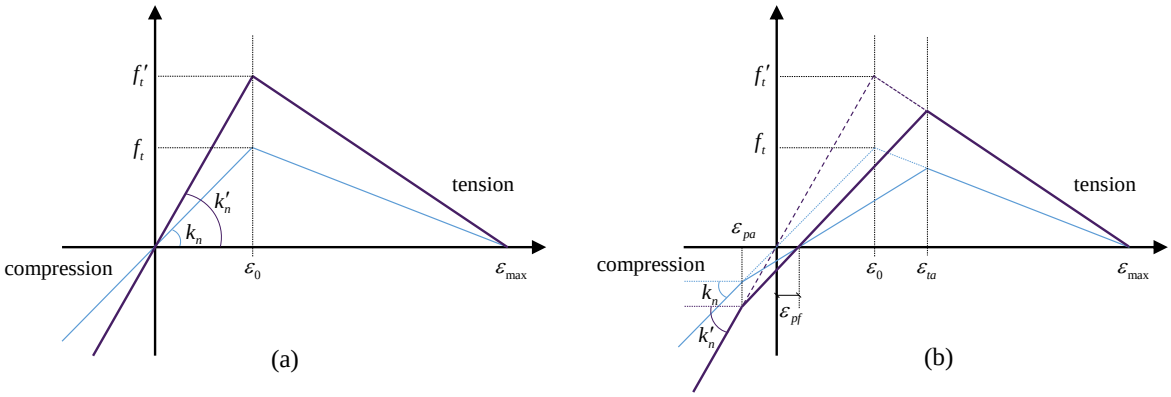

Fig. 5.4 The stress-strain relation strengthened by ice

The unloading and reloading paths have also been modified based on previous models (Gong et al., 2013) to reflect the ice strengthening effect (Fig. 5.4 (b)). In the previous model, ε_{pa} is used to show the relative relationship between the maximum plastic tensile strain (ε_{ta}) in the softening curve and the unrecoverable strain (ε_{pf}) at the end of each FTC (Gong et al., 2015). No matter whether there is formed ice or not, for the porous body itself, the above mechanical parameters should always be the same. Then the consistency of the stress-strain relationship of porous body under different conditions could be satisfied. For example in both Fig. 5.4 (b), when ice melts and k_n' becomes equal to k_n, the ice strengthened curve will shift back to the original one in room temperature.

5.2.2 Input material properties

The determination process of input material properties will be based on Nagai et al. (2004), and another two parameters are included in this study: the void ratio (ϕ_m) and the intrinsic elastic modulus (E_s) of mortar elements. As shown in Fig. 5.5, the W/C ratio of mortar is the only parameter that decided manually, and other parameters can be derived according to the flow chart. Based on Kosaka et al.'s (1975) data, the compressive strength (Eq. (5.21)), elastic modulus (Eq. (5.22)) and the tensile strength (Eq. (5.23)) are as follows:

$$f_{cm}' = 21.3c/w - 10.6 \tag{5.21}$$

$$E_m = 1000(7.7\ln f_{cm}' - 5.5) \tag{5.22}$$

$$f_{tp} = 1.4\ln f_{cm}' - 1.5 \tag{5.23}$$

where c/w is the inverse value of W/C ratio, f'_{cm} is the static compressive strength of mortar (MPa), E_m is the elastic modulus of mortar (MPa) and f_{tp} is the pure tensile strength of mortar (MPa). The properties

of interface are regressed by Nagai et al. (2004), which are based on the experiments by Hsu and Slate (1963) and Taylor and Broms (1964):

$$f_{ti} = -1.44\,w/c + 2.3 \tag{5.24}$$

$$c = -2.6\,w/c + 3.9 \tag{5.25}$$

where f_{ti} is the tensile strength of mortar-aggregate interface (MPa), c is the constant in Eq. (5.5) (MPa). The elastic modulus of coarse aggregates are set as 50GPa; the Poisson's ratio of mortar and aggregates are 0.18 and 0.25; and the constant φ in Eq. (5.5) is chosen as 35° according to Nagai et al. (2004).

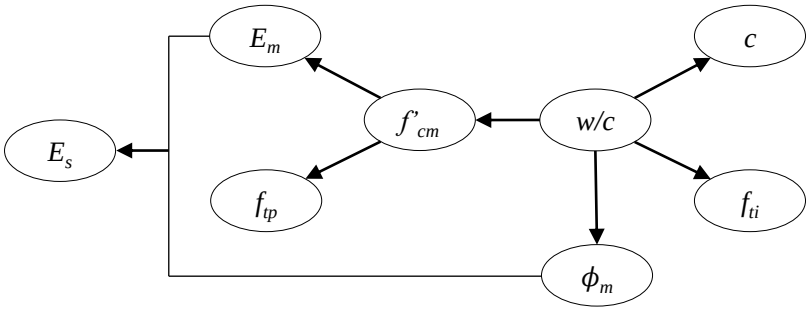

Fig. 5.5 Determination of input material properties

Once the W/C ratio is known, the void ratio of mortar can be estimated using the empirical equations by Gong et al. (2014), which was developed based on Xi et al.'s (1994) water adsorption isotherms and the empirical equations by Shimomura et al. (1992) and Takewaka et al. (2003). For cement paste, the fully saturated water content was given by Xi et al. (1994):

$$W_{sat} = \frac{CkV_m}{(1-k)[1+(C-1)k)]} \tag{5.26}$$

where W_{sat} (g/g) is the normalized water content by weight of cement paste, and the parameters in Eq. (5.26) were given as:

$$\begin{cases} V_m = (0.068 - \dfrac{0.22}{t})(0.85 + 0.45\dfrac{w}{c}) \times 0.6 \\ k = \dfrac{(1-\dfrac{1}{n})C - 1}{C-1} \\ n = (2.5 + \dfrac{15}{t})(0.33 + 2.2\dfrac{w}{c}) \times 1.5 \\ C = \exp(\dfrac{855}{T}) \end{cases} \tag{5.27}$$

where t is the age of cement paste and T is the absolute temperature. In this study t is chosen as 28 days and T is 293K for convenience. Then the total volume ratio of pores in cement paste (ϕ_{cp}) would be:

$$\phi_{cp} = \frac{W_{sat}/\rho_l}{1/\rho_s + W_{sat}/\rho_l} \tag{5.28}$$

where ρ_l and ρ_s are the density of liquid water and cement-based solid, which are roughly assumed as $\rho_l \approx 1\text{g/cm}^3$ and $\rho_s \approx 2.16\text{g/cm}^3$, respectively. As discussed in Gong et al. (2014), the total void ratio of mortar (ϕ_m) and concrete (ϕ_{con}) can be estimated as:

$$\phi_m = \psi_{CP} \cdot \phi_{cp} + V_{meso} \tag{5.29}$$

$$\phi_{con} = (1 - \psi_{AGGRE})\phi_m + V_{macro} \tag{5.30}$$

where Ψ_{CP} and Ψ_{AGGRE} are the volume ratio of cement paste and coarse aggregates respectively, V_{meso} and V_{macro} are the volume ratio of meso pores and macro pores (Shimomura et al., 1992; Takewaka et al., 2003), which can be estimated by the following equation (Gong et al., 2014):

$$V_{meso} = 5 \times 10^{-4} \exp(6.15 w/c) \tag{5.31}$$

$$V_{macro} = 0.22(w/c)^2 - 0.11 w/c + 0.016 \tag{5.32}$$

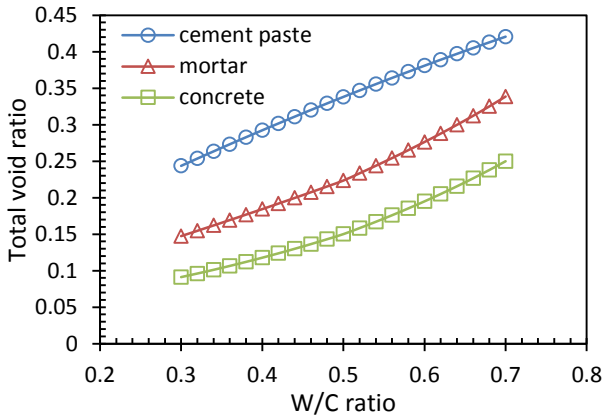

Fig. 5.6 Input total void ratio from empirical estimation

Table 5.2 The input material properties of mortar

w/c	ϕ_m	f'_{cm}	E_m	f_{tp}	c	f_{ti}	E_s
0.3	14.74%	60.28	26.06	4.24	3.12	1.87	37.2
0.5	22.35%	31.91	21.17	3.35	2.60	1.58	36.0
0.7	33.86%	19.76	17.47	2.68	2.08	1.29	39.3

Fig. 5.6 shows an example of the estimated total void ratio for cement paste, mortar and concrete with different W/C ratio. The volume fraction of cement paste in mortar is roughly determined by regression of Sicat et al.'s data (2014), which is approximately as Ψ_{CP}=0.313w/c+0.486, and the volume fraction of coarse aggregate in concrete is assumed as 40%. In the RBSM simulation, only the total void ratio of mortar will be used as the input in the calculation. After knowing the elastic modulus (E_m) and the void ratio (ϕ_m) of the mortar, the intrinsic elastic modulus of mortar solid (E_s) can be back analyzed using the two-phase model in Chapter 4, in which the mortar can be approximately regarded as water saturated. Then the input material properties in Fig. 5.5 can be estimated as shown in Table. 5.2. In addition, the effective elastic modulus of mortar due to ice strengthening effect can also be calculated using the proposed model in Chapter 4 (Fig. 5.7). For the mortar-aggregate interface, there are limited studies on the properties change due to ice strengthening effect, which will be investigated in the future studies. But the elastic modulus of interface at different temperatures will still use a weighted average of mortar and aggregate (Eq. (5.2)) but adopting the strengthened values. Then tensile strength of interface (f_{ti}) will be changed according to the elastic modulus by setting the critical strain

(ε_0) unchanged, which is similar to the mortar part as discussed in Fig. 5.4.

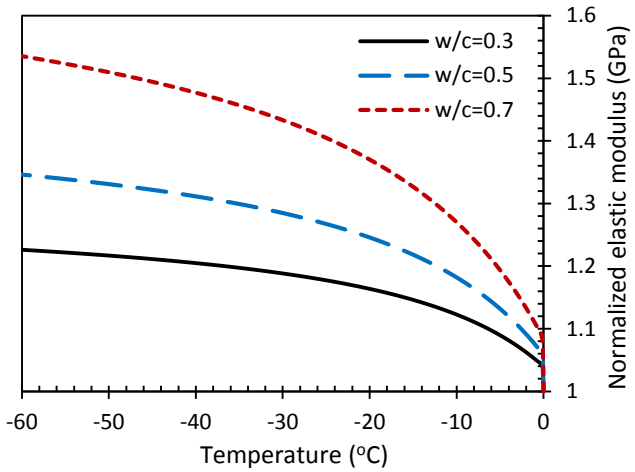

Fig. 5.7 Estimated effective elastic modulus of saturated mortar under low temperature

5.3 Fatigue loading

The constitutive model for fatigue loading based on RBSM has been studied by Matsumoto et al. (2008) and modified later (2010). Matsumoto et al.'s model not only dues with the damage cumulating during large number of fatigue cycles, but also takes the time-dependent creep into condition, which contents four kinds of mechanical component in the springs: the elastic, plastic, visco-elastic and visco-plastic component. However, if only focus on the damage cumulating during fatigue loading, Matsumoto's model can be simplified into a time-independent two component model, which only concerns the elastic and plastic deformation. Since the creep itself does not cause significant damage or failure, especially when the stress condition is rather uniform, such as the uniaxial compression and tension, thus it can be estimated based on the existing theories (Bazant and Baweja, 2000; Bazant and Hubler, 2014). By doing so, the calculation can become much simpler and more efficient, and easy to be combined with the FTC damage in the next step. In addition, although the strain history will become slightly different from Matsumoto's simulation, the damage cumulating and fatigue life will not be affected much. Then, using the similar idea presented in Matsumoto et al. (2010), a stress reduction must be introduced in the tension softening curve of the normal spring (see Fig. 5.8).

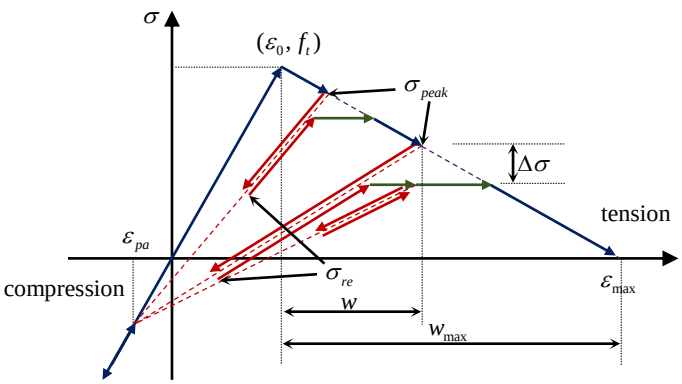

Fig. 5.8 The stress reduction in the tensile softening curve for normal spring

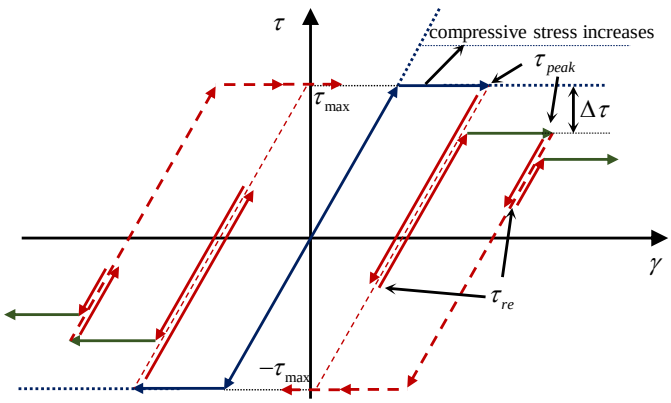

Fig. 5.9 The stress-strain relation of shear springs and the reduction of shear capacity

Compared to the stress-strain relation discussed in Section 5.1 and 5.2, ε_{pa} still has the same value and same physical meaning, while the only change is the introduce stress reduction $\Delta\sigma$, which empirically depends on the peak stress (σ_{peak}) and residual stress (σ_{re}) of each loading cycle (Matsumoto et al., 2010):

$$\Delta\sigma = c_{yn}\sigma_{peak}{}^{\alpha}(\sigma_{peak} - \sigma_{re}) \tag{5.33}$$

where c_{yn} and α are parameters which reflects the effect of unloading and reloading on the stress reduction. For the shear spring, the ideal plastic performance is assumed as shown in Fig. 5.9, and also similar stress drop as the normal spring is introduced to reflect the degradation during cyclic loadings. The maximum shear capacity (shear criterion) will be affected by both the crack width in normal spring and the unloading and reloading of the shear stress, which is (Matsumoto et al., 2010):

$$\begin{aligned} \tau_{\max} &= \pm\left[0.11 f_t^3 (f_t - \sigma)^{0.6} + f_t\right] \times f_1 \times f_2 \\ f_1 &= 1 - w / w_{\max}, \quad f_2 = 1 - c_{ys}\tau_{peak}{}^{\beta}(\tau_{peak} - \tau_{re}) \end{aligned} \tag{5.34}$$

where f_1 is the reduction factor due to the crack opening in normal direction and f_2 reflects the effect of cyclic shear stress. w is the crack width after the tensile strain exceeds the critical strain (ε_0) at the tensile strength (f_t), and $w_{\max}$ is the maximum crack width:

$$\begin{aligned} w &= (h_1 + h_2)(\varepsilon - \varepsilon_0) \\ w_{\max} &= (h_1 + h_2)(\varepsilon_{\max} - \varepsilon_0) \end{aligned} \tag{5.35}$$

Since $\varepsilon_{\max}$ is much bigger than ε_0, then $w_{\max} \approx (h_1+h_2)\varepsilon_{\max}$=0.03mm. c_{ys} and β are the parameters reflected the continuous degradation of the shear spring by cyclic unloading and reloading. τ_{peak} and τ_{re} are the peak and residual stress in the shear springs. In Matsumoto et al.'s study (2010), the above parameters are given for the pure mortar, which are:

$$\begin{aligned} c_{yn} &= 2.0 \times 10^{-6} \\ c_{ys} &= 3.0 \times 10^{-10} \\ \alpha &= 9.0 \\ \beta &= 7.0 \end{aligned} \tag{5.36}$$

However for the concrete, the mortar-aggregate interface must be taken into consideration. Although the properties of the interface are usually weaker than the mortar, the general characteristics of the degradation at interface should be similar with the mortar. Therefore, similar idea as Matsumoto

et al. (2010) will be applied on the interface, which is:

$$\Delta\sigma = c_{yni}\sigma_{peak}{}^{\alpha_i}(\sigma_{peak} - \sigma_{re}) \tag{5.37}$$

$$\begin{aligned} &\tau_{\max} = \pm\left(-\sigma\tan\varphi + c\right)\times f_1 \times f_2 \\ &f_1 = 1 - w/w_{\max},\ \ f_2 = 1 - c_{ysi}\tau_{peak}{}^{\beta_i}(\tau_{peak} - \tau_{re}) \end{aligned} \tag{5.34}$$

where c_{yni}, α_i, c_{ysi} and β_i have the same physical meaning with the mortar element, but the values should be different to reflect different degradation speed under cyclic loads, which are chosen as:

$$\begin{aligned} &c_{yni} = 2.0\times10^{-4} \\ &c_{ysi} = 3.0\times10^{-9} \\ &\alpha_i = 9.0 \\ &\beta_i = 7.0 \end{aligned} \tag{5.35}$$

During the fatigue test, the duration is usually long enough to have obvious creep deformation. The creep occurs at all stress levels and, within the service stress range, is linearly dependent on the stress if the pore water content is constant. There are several models to estimate the creep strain under sustained loads, such as the B3 Model (Bazant and Baweja, 2000). In addition, Bazant and Hubler also developed a theoretical model for the creep under fatigue loadings based on Paris law (2014), in which the total creep strain is:

$$\varepsilon_N = J_{tot}\sigma_{mean} \tag{5.36}$$

where ε_N is the total creep strain after N cycles; J_{tot} is the total material compliance (the creep strain caused by per unit of stress); σ_{mean}=0.5($\sigma_{\max}$+$\sigma_{\min}$) is the mean stress of the fatigue loading. The total compliance is composed by two parts:

$$J_{tot} = J(t,t_0) + J_N \tag{5.37}$$

where $J(t,t_0)$ is the compliance for ordinary creep based on the B3 Model (Bazant and Baweja, 2000), and here the elastic response is excluded; J_N is the compliance for the cyclic effect of fatigue. If excluding the elastic response during the fatigue test, and also moisture content is assumed constant, then $J(t,t_0)$ would be as the follows according to the B3 Model:

$$J(t,t_0) = q_2 Q(t,t_0) + q_3\ln[1+(t-t_0)^n] + q_4\ln\left(\frac{t}{t_0}\right) \tag{5.38}$$

where q_2, q_3 and q_4 represent the ageing viscoelastic compliance, non-ageing viscoelastic compliance, and flow compliance, respectively (Bazant and Baweja, 2000); and $Q(t,t_0)$ is a binomial integral which cannot be expressed analytically, whose values are shown in Bazant and Baweja's paper (2000); n is a constant which equals to 0.1; t_0 is the age when the loads are applied (in days); t is the current time (in days). The determination of those parameters are:

$$\begin{cases} q_2 = 185.4c^{0.5} f_c{}^{-0.9} \\ q_3 = 0.29(w/c)^4 q_2 \\ q_4 = 20.4(a/c)^{-0.7} \end{cases} \tag{5.39}$$

where w, c and a are the content (kg/m^3) of water, cement and aggregates respectively. For the cyclic effect, Bazant and Hubler has given its expression as:

$$J_N = C_t \left(\frac{\Delta\sigma}{f_c} \right)^m N \tag{5.40}$$

where C_t is constant based on the material properties, which is chosen as 6.67×10^{-3} (micron/MPa); N is the number of fatigue cycles; m is a constant which equals to 4 according to Bazant and Hubler (2014); $\Delta\sigma$ is the amplitude of the fatigue loads. Then, if taking w=310, c=620 and a=1240 as in Matsumoto et al. (2010), for different loading frequency, the basic creep ($J(t,t_0)$) and the fatigue creep (J_N) can be estimated as in Fig. 5.10 (a). It can be seen that the basic creep is almost linear to the logarithm value of cycles while the fatigue creep is linear to the No. of loading cycles. Fig. 10 (b) shows the total compliance for different stress levels. It can be seen that for the low cycle fatigue, the fatigue creep is not significant while the main creep deformation comes from the basic creep. And for the high cycle fatigue, the fatigue creep becomes obvious and the higher stress level is, the bigger creep compliance will be. Finally in the RBSM simulation, the total creep compliance will be introduced to each normal spring according to their particular stress conditions.

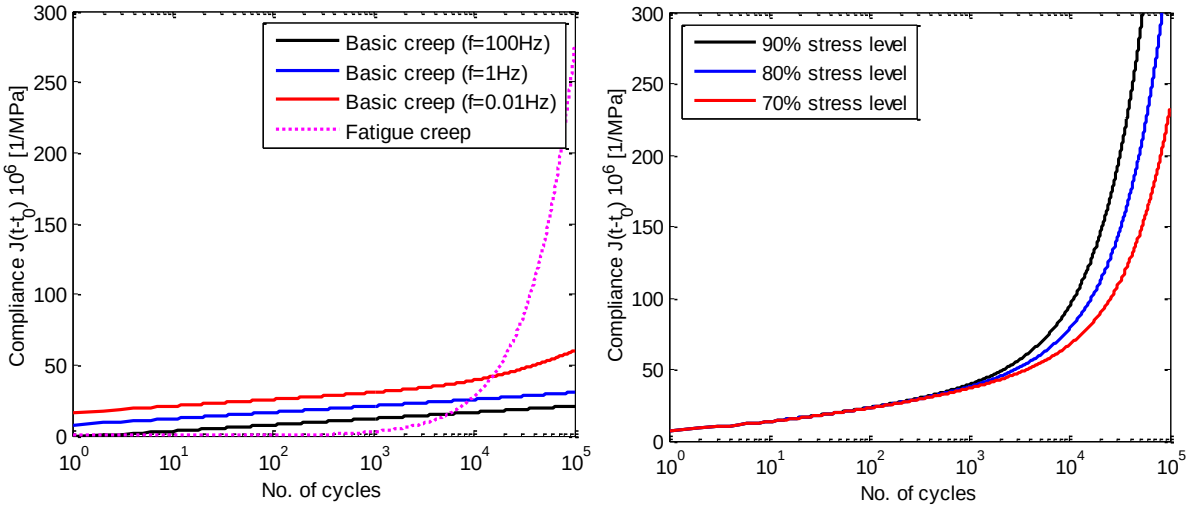

(a) (b)

Fig. 5.10 The estimated creep compliance during fatigue test

5.4 Conclusions of this chapter

The constitutive laws for Rigid Body Spring Method (RBSM) under different freeze-thaw and mechanical loading conditions are developed in this chapter, and the details are:

(1) The constitutive laws are developed based on the theoretical derivations in previous chapters, which will be used in the RBSM simulation in the next chapter.

(2) For the constitutive laws of pure FTC deformation, the nature of the internal effective stress (an average stress on the porous matrix caused by pore pressures) as well as the deformation compatibility between ice-water and pore structure can be conveniently described by a parallel spring model, and the constitutive laws for each spring is discussed. This parallel system can adjust the applied stress on the spring of porous body automatically if the strain changes. In addition, the strengthening effect by ice can be also taken into consideration. The transformation of internal effective stress to an equivalent external stress makes the numerical simulation much simpler.

(3) The ice strengthening effect under external loadings at low temperatures can be reflected by the increasing in the input stiffness in the mesoscale simulation. Since the critical strain at the tensile strength does not change, the actual tensile strength will also increase proportionally to the stiffness

due to the strengthening effect. In addition, since the moisture in the coarse aggregates can be neglected, the increasing in the stiffness and tensile strength will only happen in the mortar part and mortar-aggregate interface. Therefore, by changing the properties of mortar and interface, the macroscale mechanical behavior can be simulated.

(4) The constitutive laws under fatigue loading are also discussed in this chapter. In order to make the stress-strain relationships of each spring much simpler, the previous model is simplified into a time-independent model which only focus on the final damage under fatigue loadings. And also the damage cumulating is introduced to mortar-aggregate interface similarly as pure mortar in previous studies, then by doing so, the fatigue simulation to concrete becomes possible.

REFERENCES

Bazant, Z. P., and Baweja, S. (2000). "Creep and shrinkage prediction model for analysis and design of concrete structures: Model B3." *ACI Special Publications*, 194, 1-84.

Bazant, Z. P., and Hubler, M. H. (2014). "Theory of cyclic creep of concrete based on Paris law for fatigue growth of subcritical microcracks." *Journal of the Mechanics and Physics of Solids*, 63, 187-200.

Coussy, O., (2005). “Poromechanics of freezing materials.” *Journal of the Mechanics and Physics of Solids*, 53, 1689-1718.

Coussy, O. and Monteiro, P.J.M., (2008). “Poroelastic model for concrete exposed to freezing temperatures.” *Cement and Concrete Research*, 38, 40-48.

Coussy, O. and Monteiro, P.J.M., (2009). “Errata to “Poroelastic model for concrete exposed to freezing temperatures” [Cement and Concrete Research 38 (2008) 40–48]”, *Cement and Concrete Research*, 39, 371-372.

Gong, F., Sicat, E., Ueda, T. and Zhang, D., (2013). “Meso-scale mechanical model for mortar deformation under freeze thaw cycles.” *Journal of Advanced Concrete Technology*, 11, 49-60.

Gong, F., Zhang, D., Sicat, E. and Ueda, T. (2014), “Empirical estimation of pore size distribution in cement, mortar and concrete.” *Journal of Materials in Civil Engineering*, 26 (7), 04014023

Gong, F., Sicat, E., Zhang, D. ad Ueda, T., (2015), “Stress analysis for concrete materials under multiple freeze-thaw cycles.” *Journal of Advanced Concrete Technology*, 15, 124-134.

Hasan, M., Okuyama, H., Sato, Yasuhiko. and Ueda, T., (2004). “Stress-stain model of concrete damaged by freezing and thawing cycles.” *Journal of Advanced Concrete Technology*, 2 (1), 89-99.

Hsu, T.T.C. and Slate, F.O., (1963), “Tensile bond strength between aggregate and cement paste or mortar.” *Journal of ACI*, 60 (4), 465-485.

Johannesson, B., (2010). “Dimensional and ice content changes of hardened concrete at different freezing and thawing temperatures.” *Cement & Concrete Composites*, 32, 73-83

Kaufmann, J.P., (2004). “Experimental identification of ice formation in small concrete pores.” *Cement and Concrete Research*, 34, 1421-1427.

Kawai, T., (1977). “New element models in discrete structure analysis.” *Journal of Society of Naval Architectures of Japan*, 141, 187-193.

Kosaka, Y., Tanigawa, Y. and Kawakami, M., (1975). “Effect of coarse aggregate on fracture of concrete (Part1).” *Transactions of the Architectural Institute of Japan*, 228, 1-11 (in Japanese).

Matsumoto, K., Sato, Y., Ueda T. and Wang, L., (2008). “Mesoscopic analysis of mortar under high-stress creep and low-cycle fatigue loading.” *Journal of Advanced Concrete Technology*, 6 (2), 337-

352.

Matsumoto, K., Sato, Y., and Ueda, T. (2010). "FRACTURE MECHANISM AND PREDICTION OF DEFORMATION OF MORTAR UNDER TIME-DEPENDENT LOADS BY MESO-SCALE ANALYSIS." *Doboku Gakkai Ronbunshuu E/JSCE Journal of Materials, Concrete Structures and Pavements*, 66(4), 380-398.

Nagai, K., Sato, Y. and Ueda, T., (2004). "Mesoscopic simulation of failure of mortar and concrete by 2D RBSM." *Journal of Advanced Concrete Technology*, 2 (3), 359-374.

Power, T. C., (1949). "The air requirement of frost-resistant concrete." *Proc. Highway Res. Board*, 29, 184-211.

Scherer, G.W. and Valenza II, J.J., (2005). "Mechanism of frost damage." In: Skalny, J. and Young, F. Eds. *Materials Science of Concrete*, Vol. VII: American Ceramic Society, 209-246.

Shimomura, T., Ozawa, K., 1992. Analysis of water movement in concrete based on micro pore structural model. Proceedings of JCI, Vol.14, No.1, 631-636. (Japanese)

Sicat, E., Gong, F., Zhang, D. and Ueda, T., (2013). "Change of the coefficient of thermal expansion of mortar due to damage by freeze thaw cycles." *Journal of Advanced Concrete Technology*, 11, 333-346.

Sicat, E., Gong, F., Ueda, T. and Zhang D., (2014). "Experimental investigation of the deformational behavior of the interfacial transition zone (ITZ) of mortar during freezing and thawing cycles." *Construction and Building Materials*, 65, 122-131.

Sun, Z. and Scherer, G.W., (2010a). "Effect of air voids on salt scaling and internal freezing." *Cement and Concrete Research*, 40, 260-270.

Sun, Z. and Scherer, G.W., (2010b). "Pore size and shape in mortar by thermoporometry." *Cement and Concrete Research*, 40, 740-751.

Takewaka, K., Yamaguchi, T., Maeda, S., (2003). "Simulation model for deterioration of concrete structures due to chloride attack". *Journal of Advanced Concrete Technology*, 1: 139-146.

Taylor, M.A. and Broms, B.B. (1964). "Shear bond strength between coasrse aggregate and cement paste or mortar." *Journal of ACI*, 61 (8), 939-956.

Ueda, T., Hasan, M., Nagai, K., Sato, Y. and Wang, L., (2009). "Mesoscale simulation of influence of frost damage on mechanical properties of concrete." *Journal of Materials in Civil Engineering*, 21, 244-252.

Xi, Y., Bazant, Z.P., Jennings, H.M., (1994). "Moisture diffusion in cementitious materials Adsorption isotherms". *Advanced Cement Based Materials*, 1: 248-257.

CHAPTER 6

6. Mesoscale Simulations

6.1 Deformation under pure FTC

The numerical model is conducted to simulate previous experiments, that is, the saturated mortar (Sicat et al, 2013) and mortar with single aggregate (Sicat et al, 2014) in closed test (40mm×40mm×2mm square slice), as well as the concrete cylinder (Hasan et al, 2004) in open test (100mm×100mm×200mm). The 2D models are developed with the size and boundary conditions shown in Fig. 4. The input material properties are chosen according to those experiments and also some are from the empirical values (Table 6.1). Fig. 6.1 (a) and (b) are for the closed test under 30 and 20 freeze/thaw cycles, respectively, with the cooling rate of 15ºC/h and lowest temperature of -28ºC. Fig. 6.1 (c) is for the open test under 300 cycles, and the cooling rate is around 7.5ºC/h with lowest temperature of -20ºC.

Table 6.1. Parameters for mortar in closed test (Sicat et al. 2013)

Type (w/c)	Mortar (0.5)
Mix proportion by weight (w : c : a)	1:2:6
Water saturated (vacuum saturated)	0.228 (0.238) g/cc
Real water saturation	95.8%
Poisson's ratio of mortar v	0.2
Bulk modulus of ice crystal K_C	8.8 GPa
Bulk modulus of liquid water K_L	2.2 GPa
Critical radius r_0 (Gong et al, 2014)	2×10^{-4}m
(by X-ray CT scanning)	1.7×10^{-4}m
Equivalent r_E	6×10^{-4}m
Equivalent R_E	0.0028m

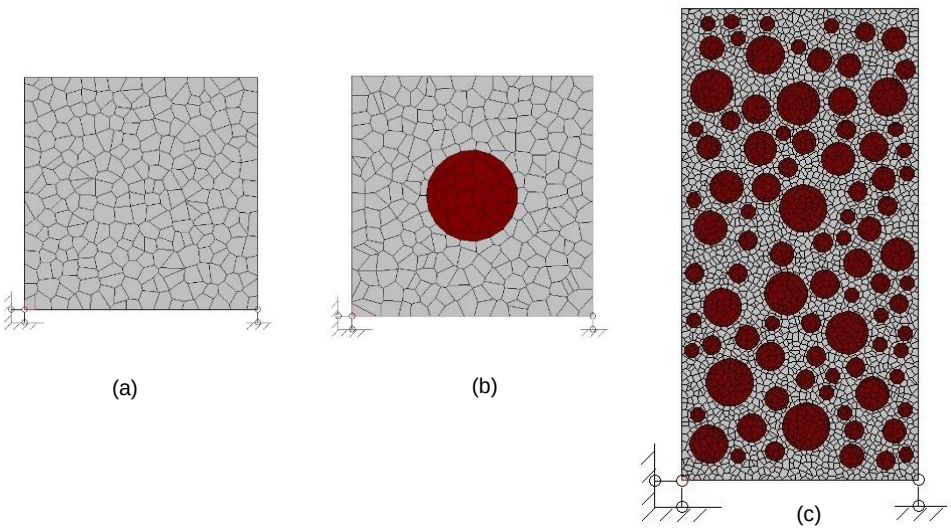

Figure 6.1. Simulation models and boundary conditions (a) mortar $40\text{mm}\times40\text{mm}$, 259 elements (b) mortar with single aggregate $40\text{mm}\times40\text{mm}$, 274 elements (c) concrete cylinder $200\text{mm}\times100\text{mm}$,

4251 elements

Here the temperature and moisture distribution are assumed uniform because the size of specimens is small in Sicat's tests. Even for bigger specimens in Hasan's tests, the measured temperatures at different locations inside the concrete cylinder still showed uniform distribution (Hasan et al., 2004). Since the FTC test was conducted directly after a long time of water curing, and also there was continuous water supply during the test, the moisture condition can be considered as uniform distributed as well. Therefore, the moisture movement and temperature difference are insignificant in the simulation model, and once the environmental conditions are given, the internal stress should be the same on all the normal springs, but only exits in the mortar and mortar-aggregate interfaces, because the ice formation in the aggregates is neglected (Sicat et al., 2014).

For the closed test, moisture content is constant, so the permeability is the main influential factor for the material deformation. It has been proved in previous study that the permeability of concrete materials would increase significantly after frost damage (Yang et al. 2006). And also by assuming proper changes in the permeability, the experimental observations can be simulated nicely and quantitatively by the developed pressure model (Gong et al. 2015). However, it is still difficult to predict the change of permeability precisely due to the two reasons: one is because the freeze-thaw experiment itself varies case by case (Sicat et al. 2013), and another is that the permeability of cementitious material is very small ($10^{-19}m^2$ to $10^{-21}m^2$) and difficult to be measured; in addition, it is not clear whether this increment is due to better pore connectivity or internal cracking, and in which scale. Therefore, the permeability change needs to be investigated in detail, which will be conducted in the future. Since this paper mainly focus on the mechanical analysis, the permeability change will be treated as an output, because only proper values can match the complex deformation in the experiments.

For the open test up to 300 cycles (Hasan et al. 2004), the permeability is no longer the key factor, because it can reach a large enough value in a few cycles, by which the Darcy's flow becomes quick enough to avoid damage. However, with continuous water supply in open test, the saturation degree will increase and the entrained or entrapped air will be filled up gradually. Even the water in smaller pores can move to the empty space completely freely, there is still no enough space to hold the additional volume. Therefore, for the open test, the Darcy's flow is ignored and it becomes a pure poromechanical problem. Then Eq. (5.19) becomes:

$$\begin{aligned} 0.09\psi_C &= \left(\frac{\psi_C}{K_C} + \frac{\psi_L}{K_L}\right) \cdot p_h + (1 - Sr) \\ \sigma_0 &= b \cdot p_h \end{aligned} \tag{6.1}$$

The water uptake was measured by Fagerlund (2002) during the open freeze-thaw test, which showed an increasing behaviour but with decreasing speed. According to Hall (1989), the cumulated water absorption increases almost linearly with the square root of time. Therefore, the saturation degree change in the simulation can be assumed as:

$$Sr = Sr_0 + a\sqrt{N} \tag{6.2}$$

where Sr_0 is the initial saturation degree when the test started, which is assumed as 0.98 considering some entrapped air. N is the number of freeze thaw cycles and the speed of saturation degree increment is controlled by factor a, which has the similar meaning as sorptivity. The driving force of this water uptake is no longer the capillary absorption because the specimen is almost saturated at the beginning so the capillary pressure is quite small inside the material. However, if a temperature gradient exists

from the surface inwards, the crysuction pressure (p_l) is not uniform according to Eq. (3.24). Thus there will be a pressure gradient in the unfrozen water:

$$\frac{\partial p_l}{\partial x} = \Delta S_{fv} \frac{\partial(\psi_L \cdot T)}{\partial x} \tag{6.3}$$

Since ψ_L=Sr-ψ_C, and ψ_C can be written as a function of temperature as Eq. (3.17). Then Eq. (6.3) becomes:

$$\frac{\partial p_l}{\partial x} = \Delta S_{fv} \frac{\partial(3.585\times10^{-4}T^3 + 0.0236T^2 + T)}{\partial x} = \Delta S_{fv}\left(1.076\times10^{-3}T^2 + 0.0472T + 1\right)\frac{\partial T}{\partial x} \tag{6.4}$$

Then according to Darcy's law, the water flow (m/s) is:

$$q = \frac{k}{\eta} \cdot \frac{\partial p_l}{\partial x} \tag{6.5}$$

From Eq. (6.4) and Eq. (6.5), the water flow (q) mainly depends on the temperature, which can be obtained by solving the heat transfer equations. If taking an average value of the water flow during one FTC as $\bar{q}$, then the total amount of water flowing into specimen during one cycle should be:

$$Q = \bar{q} \cdot A_C \cdot t \tag{6.6}$$

where A_C is the area of the concrete wet surface and t is the duration of one cycle. Then the increment of saturation degree becomes:

$$\Delta Sr = Q / V_A \tag{6.7}$$

where V_A is the volume of the pores. The water flow can be calculated by numerical analysis such as FEM, but here for convenience, the average flow ($\bar{q}$) can be taken from Jacobsen's measurements (2004), in which similar material and freezing conditions were used as Hasan's test (2004). Then if taking $\bar{q}$=2.25×10^{-10} m/s, A_C=π(0.1)^2/4=7.85×10^{-3} m^2 (only the top surface of concrete cylinder was contacted with free water in Hasan's tests), t=7hrs=2.52×10^4 s and V_A=2.17×10^{-4} m^3, and by Eq. (6.6) and Eq. (6.7), ΔSr can be obtained as 2×10^{-4}. Although it seems that water uptake is constant for each cycle from the discussions above, it is easy to imagine that the entrapped air should become more and more difficult to be extruded out as saturation degree continuously increases. In addition, the water flow measured by Jacobsen was also during the first several cycles. Therefore, Eq. (6.2) is still reasonable and the value of a can be chosen as 2×10^{-4}.

6.1.1 Mortar in closed test

For the closed test of mortar (30 cycles), the real time deformation is calculated based on the time-dependent internal pressures. Fig. 6.2 shows the simulated deformation of two cases and the comparison with experimental measurements. And the change of permeability can be estimated in such a way that the simulated deformation matches experiments well. For the case in Fig. 6.2 (a), the contribution of each pressure in the total effective stress is shown in Fig. 6.3 for a better understanding of the strain development.

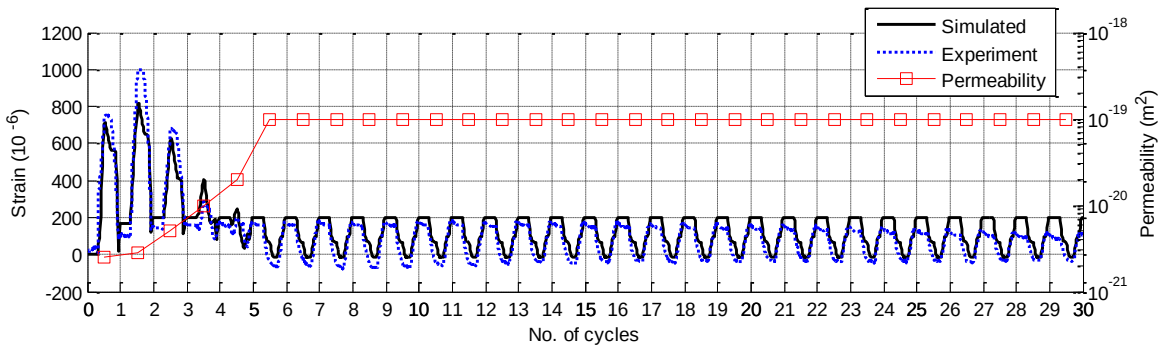

(a) Mortar (w/c=0.5, fine aggregate=754kg/m^3)

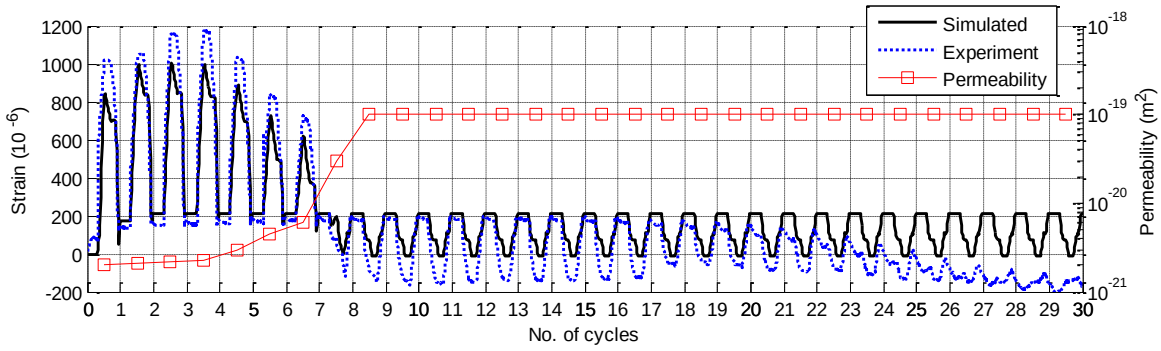

(b) Mortar (w/c=0.5, fine aggregate=1090kg/m^3)

Figure 6.2 Comparison between simulated and experimental deformation, two cases with same w/c ratio but different amount of fine aggregates.

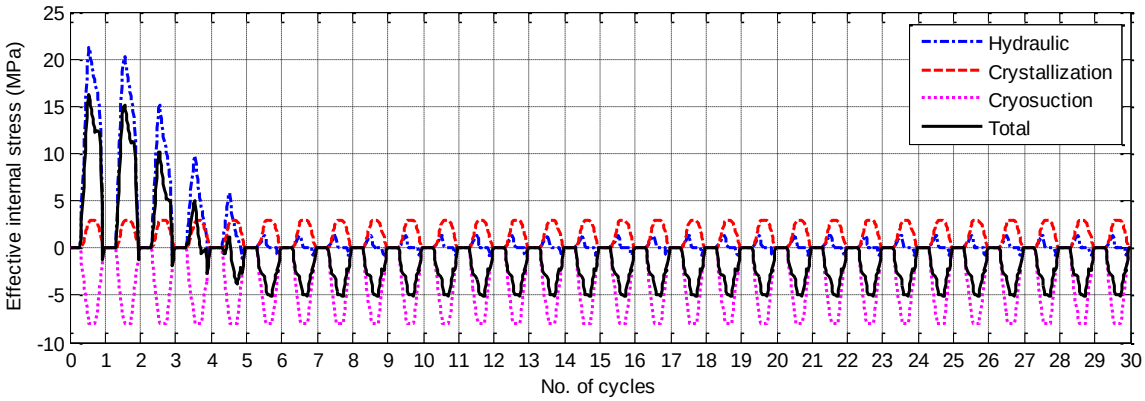

Figure 6.3. The contribution of each pressure in the total effective stress (w/c=0.5, fine aggregate=754kg/m^3)

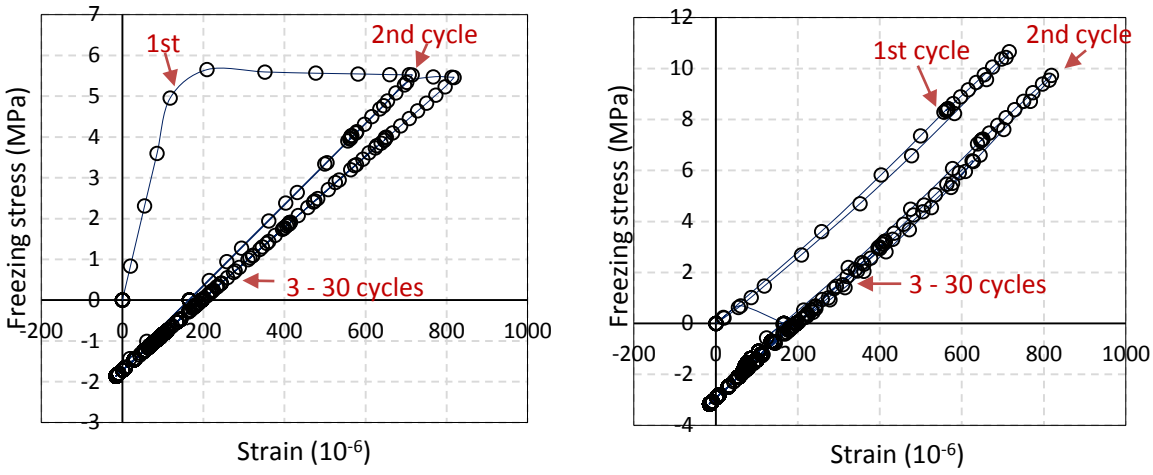

(a) (b)

Figure 6.4. Stress-strain history in closed test with 30 cycles (w/c=0.5, fine aggregate=754kg/m^3) (a) porous body (b) ice-water system

It can be seen that both Fig. 6.2 (a) and (b) show the same tendency, that is, the total internal pressure is positive at the beginning but as the hydraulic pressure is reduced due to cumulated damage, the total pressure changes to negative after a few cycles (see Fig. 6.3), thus the deformation also converts from expansion to contraction. The increasing residual strain of each cycle can be simulated based on the constitutive laws presented in Section 5.1, which will continuously increase if there is still expansion but should become constant if it converts to contraction. Fig. 6.2 (b) also shows a decreasing residual strain under cyclic compressive effective stress at last, and it is thought to be effect of creep, which has not been taken into consideration at this moment. The stress-strain history of two components (porous body and ice-water system) is shown in Fig. 6.4, from which it can be seen that the damage accumulation mainly occurs at the first two cycles. The total inputted effective stress (Fig. 6.3) will be shared by porous body and lice-water system together, therefore, during the freezing process of each cycle, the inputted stress during freezing can continuously increase even after exceeding the material's tensile strength, because the additional part can be shared by the ice-water system as in Fig. 6.4 (b).

The hydraulic pressure reduction and the increment of permeability interact with each other reciprocally. For example, if the hydraulic pressure is still high enough to cause damage, the permeability will increase in the next cycle and result in lower hydraulic pressure, and finally a stable status will be achieved in which hydraulic pressure disappears and permeability keeps constant. It can also be seen that the quick increment of permeability does not happens at the beginning. This might be because the initiation of new cracks is usually more difficult than the growth or propagation of existing cracks. That is why several cycles are needed to cumulate a certain level of damage before rapid deterioration starts. Finally, the difference in the increasing speed of permeability (or speed of damage) between Fig. 6.2 (a) and (b) might relate to the different amount of fine aggregates used in the experiments. Because greater amount of aggregates means lesser water content and smaller effective internal stress, the speed of damage could be slower.

6.1.2 Mortar-aggregate interface in closed test

The deformation behavior of mortar-aggregate interface is also measured using the same freeze-thaw test (Sicat et al. 2014). By introducing mechanical properties of the aggregate and interface (Table

6.2), the RBSM simulation can be conducted and the simulated deformation of interface is shown in Fig. 6.5, together with the experimental measurements.

Table 6.2. Mechanical properties in simulation

Parameters	Mortar	Aggregate	Interface
f_t (MPa) (a)	5.67	N.A.	1.83
f_t (MPa) (b)	4.09	N.A.	1.83
E (GPa) (a)	34	50	----
E (GPa) (b)	25	50	----
v	0.18	0.25	----
c (MPa)	----	----	3.05
φ (°)	----	----	35
w_{max} (mm)	0.03	N.A.	0.01

Note: (a) for closed test (Sicat et al. 2013, 2014); (b) for open test (Hasan et al. 2004). N.A means the aggregate is assumed not fracture. w_{max} is the maximum crack width.

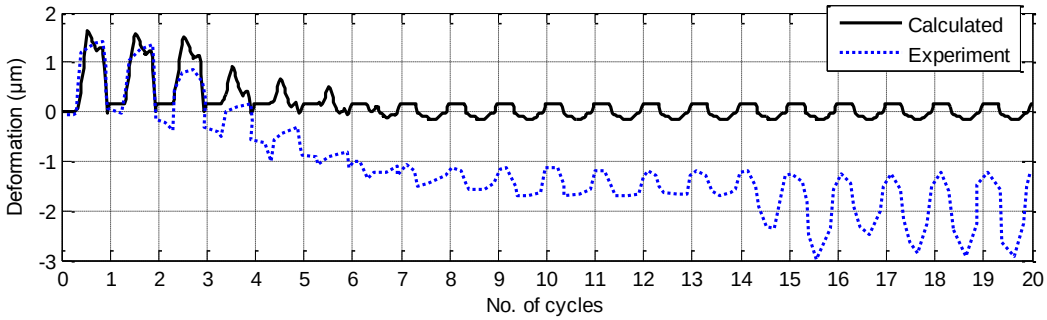

Figure 6.5. Comparison between simulated and experimental deformation of mortar-aggregate interface

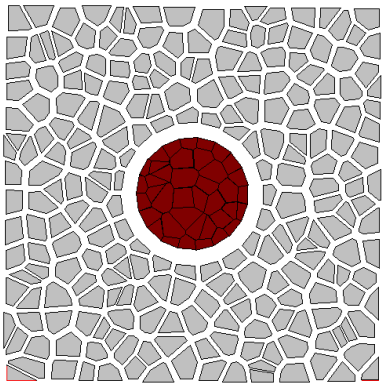

Figure 6.6. Crack opening in mortar part and mortar-aggregate interface (deformation enlarged 500 times)

The simulated results matches well with the experiment data for the first few cycles, but then a decreasing residual strain occurs in the experiments, even when the positive stress is still dominant in the simulation. Actually the experiment data itself showed a big scatter after a few cycles, which might be because that size of specimens and strain gages are very small so that the heterogeneous character of mortar could become more significant. For example, if some macro cracks occur during the test (see Sicat et al., 2014), and the strain gage just covers those cracks, then the measurement would be

interfered. Even if the strain gage does not cover those cracks, the local stress condition still might be redistributed. However, the crack opening can be simulated well by the current model, which might be more important for the durability problems under freeze-thaw cycles. The deformation pattern at the peak value during the first cycle is shown in Fig. 6.6, from which it can be seen that the mortar elements are almost uniformly expanded while the aggregate elements have insignificant expansion. The deformation compatibility is satisfied by the deformation at mortar-aggregate interface. The interface is usually the weakest point with smaller tensile strength and maximum crack width in the constitutive laws. Then if the expansion in mortar part is too big for the interface to accommodate the deformation, crack would occur at the interface. Therefore, the crack width at the interface might depends on the relative difference of the deformation between mortar and aggregate. Then the following relation could be developed:

$$w = \alpha \cdot (\varepsilon_M - \varepsilon_A) \cdot r_A \tag{6.8}$$

where w is the crack width of the interface, ε_M and ε_A are the strain in mortar part and aggregate part, respectively, and r_A is the radius of the aggregates. α (between 0 and 1) shows the constraint effect of the aggregate on the mortar deformation, for example, α=0 means the interface is strong enough that the mortar and aggregate can deform simultaneously; α=1 means the interface is so weak that there is no stress transfer between mortar and aggregate. The magnitude of α usually depends on the material properties of aggregate, mortar and interface, and it will also be affected by the volume ratio of mortar and aggregate, as well as the size of aggregate. From Fig. 6.7, α equals to 0.67 for this simulation case.

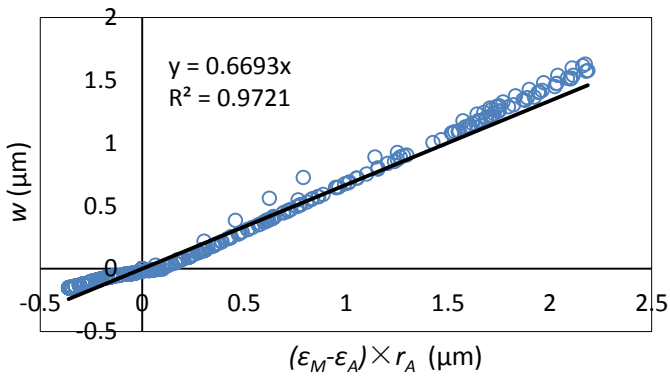

Figure 6.7. The relation between interface cracking width and the deformation difference between mortar and aggregate

6.1.3 Concrete in open test

The simulation results of concrete specimen under 300 FTCs with open moisture condition are shown in Fig. 6.8. The deformation is enlarged by 200 times in order to show the cracks clearly, from which it can be seen that the crack width in the mortar part is rather uniform and small while the crack opening of interface is much larger, and also bigger aggregates have larger crack width. This phenomenon also agrees with the discussion in the above section. Since the left half of the model contains more big aggregates, it will deform more and finally the specimen will bend slightly to the right. It is difficult to find some direct experimental observation for verifying the deformation characteristics shown in Fig. 6.8, however, since the behavior of a single mortar-aggregate interface has already been verified in Section 6.1.2, and previous experimental studies, like Jacobsen's SEM observation (1995), also shows that all the cracks are developed on the ITZ. In addition, Fig. 6.8 can be

also verified indirectly by the measured total deformation in Hasan et al. (2004). But of course more direct comparison would be better and this will be improved in the future studies.

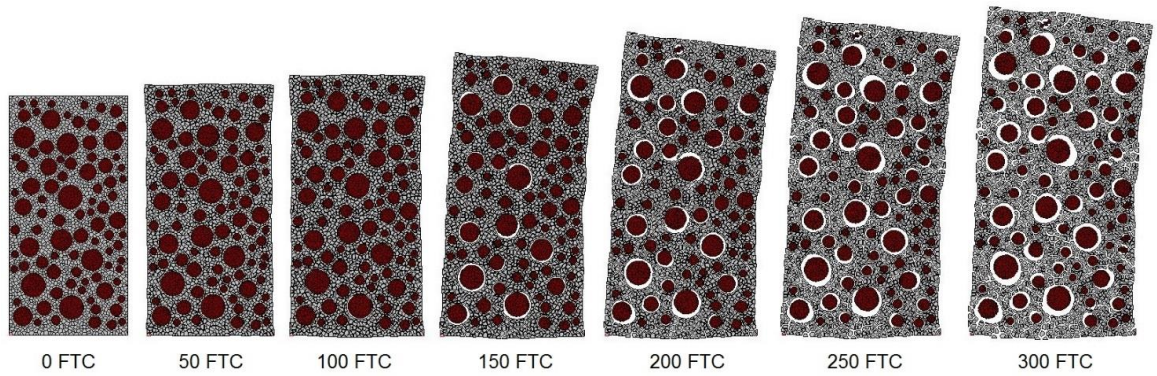

Figure 6.8. Simulated and experiment data of concrete under 300 cycles in open test (deformation is enlarged by 200 times).

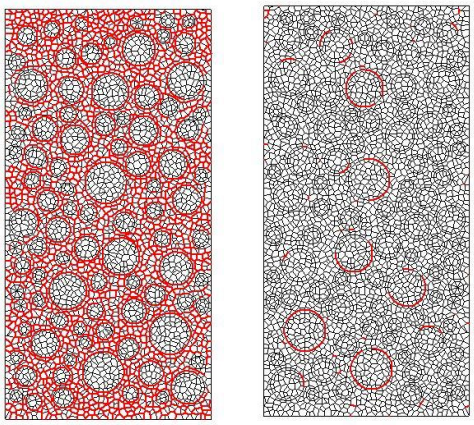

(a) (b)

Figure 6.9. Crack patters at 100th cycle (a) cracks width is larger than 0.002mm (b) cracks width is larger than 0.005mm

Fig. 6.9 shows the crack opening at the 100th cycle, it can be seen that larger aggregates have not only larger crack width, but also earlier crack opening. The crack width of mortar-aggregate interfaces varies depending on the aggregate size and the surrounding condition, meanwhile the input material properties is with normal distribution, therefore it is difficult to estimate the average width of those cracks. Here some typical locations are chosen and their crack openings during 300 cycles are shown in Fig. 6.10. Although all of those selected interfaces give similar increasing tendency, the magnitude could be different. It is difficult to find some direct experiment verification of the crack width at ITZ, however, Jacobsen's SEM observation also shows that all the cracks are developed on the ITZ (1995), and his estimated crack width varies from 5μm (at 31th cycle) to 12μm (at 95th cycle) (1996). Those crack widths were determined using the average expansion divided by the average crack density, and the crack density is counted manually from a selected area from SEM observation, which actually showed the overall characteristics of all the cracks. In the simulation program, all of the cracks along different size of aggregates can be calculated, which can vary from 0 to several dozens of micrometers. Thus, considering that there are many smaller aggregates compared with the selected ones in Fig. 6.10,

the average crack width could be smaller than the presented values, therefore the simulated results could have the similar range with the Jacobsen's data.

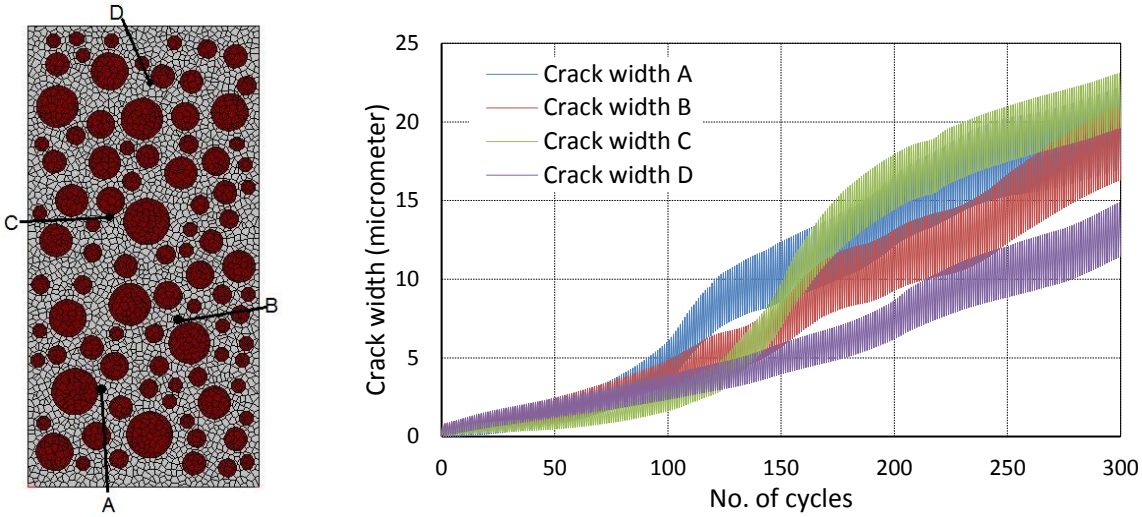

Figure 6.10. Crack width of mortar-aggregate interfaces at selected locations

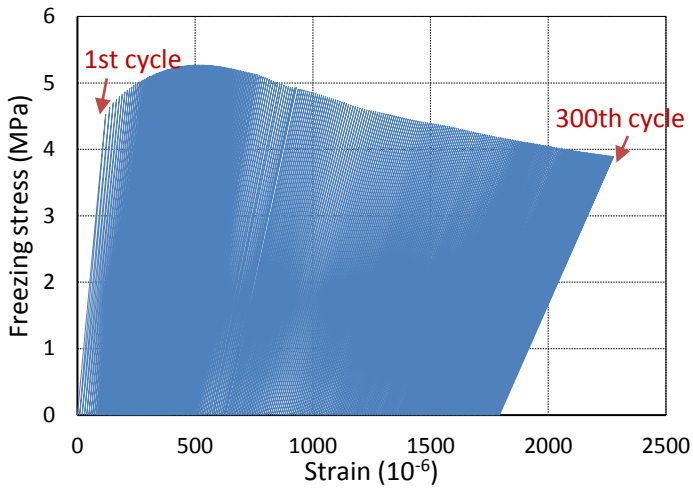

Figure 6.11. Stress-strain history of the concrete in open test with 300 cycles

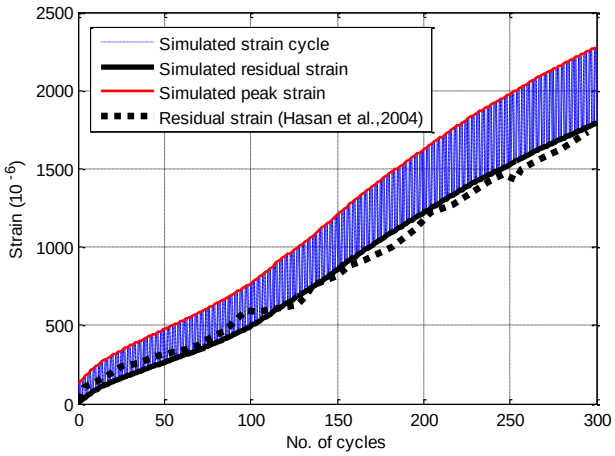

Figure 6.12. Simulated and experiment data of concrete under 300 cycles in open test.

The overall stress-strain history is shown in Fig. 6.11, where the stress means the average effective stress on the porous skeleton due to the average pore pressures and the strain is the average value of the whole concrete cylinder (the total vertical deformation divided by total height of the specimen). Since the pore pressures only exit in the mortar element and mortar-aggregate interfaces, and due to the constraint effect from the aggregates (when the mortar part expands while the aggregate do not expand), the tensile capacity of the whole concrete will be slightly higher than the average input tensile strength of mortar element (4.09MPa). Besides, different from the external tensile loads, the softening stage of concrete under internal freezing stress is rather ductile. It is because the mesoscale cracks are rather uniformly initiated and distributed, and even after the average effective stress exceeds the maximum capacity of material, the expanded ice still can prevent the crack closing, thus the stress release and brittle behavior in the uniaxial tension (Nagai et al., 2004) will not occur under the internal pore pressures. Fig. 6.12 shows the comparison between the simulated and experimental axial strains. It can be seen that the simulated residual strains match the experimental ones well. In Hasan et al.'s paper (2004), other material property degradation such as elastic modulus, compressive strength, are related to the residual strain (or plastic tensile strain), therefore, once the simulation model can fit the residual strain well, other changes in material's properties could also be estimated.

6.2 Static loading at constant low temperatures

The 2D RBSM simulation models and boundary conditions are presented in Fig. 6.13, the concrete column (200mm×100mm) will be used for the uniaxial compressive and tensile test (Fig. 6.13 (a)) and the concrete cubic (100mm×100mm) is for simulating the splitting tensile test (Fig. 6.13 (b)). Circular coarse aggregates are distributed randomly according to the size distribution from JSCE standard, with a maximum diameter of 20mm. The volume of aggregates is around 40% of the total volume of the models. There is a layer of boundary (zero thickness) elements between the applied loads on the material (Fig. 6.13 (c) (Matsumoto at al., 2010)). For the fixed boundary, all of the degree of freedoms (x, y and θ) are fixed; while for the loading plates, only x and θ are fixed.

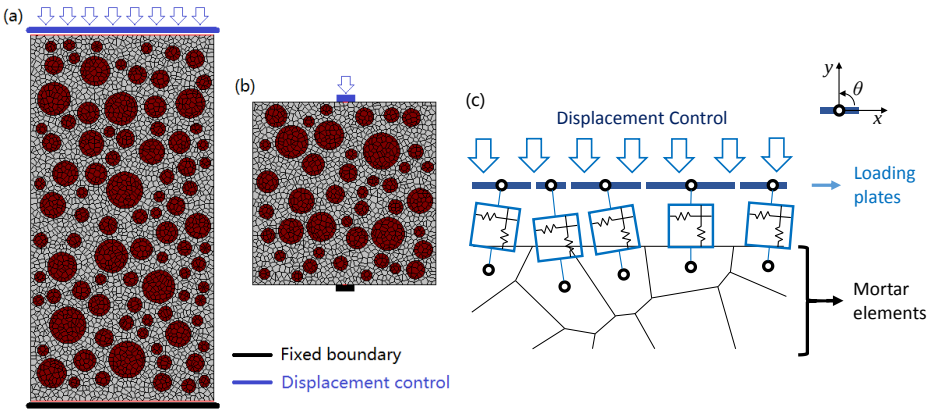

Fig. 6.13 The simulation models and boundary conditions (a) for uniaxial compression and tension, concrete column 200mm×100mm×100mm, 4251 elements; (b) for splitting, concrete cubic 100mm×100mm×100mm, 2094 elements; (c) the boundary elements

6.2.1 Pre-stored stress before loading

Before applying the mechanical loads, the pre-stored stress and strain within the porous matrix should be estimated first at different freezing temperatures. There are mainly three kinds of pressures

should be taken into consideration: the hydraulic pressure due to ice volume increment (Powers, 1949; Coussy and Monterio, 2009); and the crystallization and cryosuction pressures due to thermodynamic equilibrium (Sun and Scherer, 2010). The crystallization and cryosuction pressures are only depending on the temperature and pore size, while the hydraulic pressure is rather sensitive to the saturation degree and the amount of entrained or entrapped air. The quantitative estimation of hydraulic pressure is complicated and depending on many variables, such as saturation degree (Sr), the permeability (k_0), the volume strain of the porous matrix (ε_p), the cooling rate and so on. According to the derivations in Chapter 3, the expressions of three kinds of pore pressure are as:

$$p_h = \frac{0.09\psi_C}{\psi_C / K_C + \psi_L / K_L} \cdot f(Sr, k_0, \varepsilon_p ...) \tag{6.9}$$

$$p_l = \psi_L \cdot \Delta S_{fv} T \tag{6.10}$$

$$p_c = -\psi_C \cdot (1-\lambda) \Delta S_{fv} T \tag{6.11}$$

where $0 \le f(Sr, k_0, \varepsilon_p \ldots) \le 1$ is a reduction factor which depends on several parameters (Sr, k_0, ε_p and so on). If the saturation degree is extremely high (like the vacuum saturation), serious damage will occur even just during the first cycle, like several thousands of microns of expansion in Sun and Scherer (2010). Such magnitude of deformation is far beyond the elastic range of concrete materials and the damaged material could barely support the external loads. However, the saturation degree in the real structures cannot reach such an extremely high value, and also for the lab test, the air-entrained agent was always used in order to eliminate the effect of internal damage on the overall mechanical behavior. Then due to the sufficient empty spaces, the hydraulic pressure will be very limited (Gong et al., 2015). Therefore, only the crystallization and cryoscution pressures will be taken into consideration in this simulation to evaluate the pre-stored stress and strain condition before applying the mechanical loads. Then the total pore pressure will be:

$$p = \left(\psi_L - \psi_C \cdot (1-\lambda)\right) \Delta S_{fv} T \tag{6.11}$$

The pore pressure by Eq. (6.11) will be transformed to an average isotropic compressive stress on the mortar elements, based on Coussy's equation (Coussy, 2005):

$$\sigma_0 = \frac{2\phi_m}{1+\phi_m} \cdot p \tag{6.12}$$

where ϕ_m is the void ratio of mortar, which has been discussed in Section 5.2.2.

6.2.2 Analysis of compression

The unaxial compressive tests are simulated for concrete columm (Fig. 6.13 (a)) with different W/C ratio at different temperatures, and the stress-strain curves are shown in Fig.11.It can been seen that the low strength concrete (W/C=0.7) usually has a higher relative increment in elastic modulus and compressive strength than the high strength concrete (W/C=0.3). It is because the differences in moisture content and original properties of the porous matrix (mortar). Since there would be a static effective stress (Eq. (6.12)) due to the pore pressure (Eq. (6.11)) before the mechancal loading, which means each specimen should have a certain level of shrikage (positive compressive strain), as shown in

the smaller graphs in Fig. 6.14. For the same W/C ratio, the pre-stored shrinkage is bigger at lower temperatures, while under the same temperature, this kind of shrinkage is bigger for higher W/C ratio.

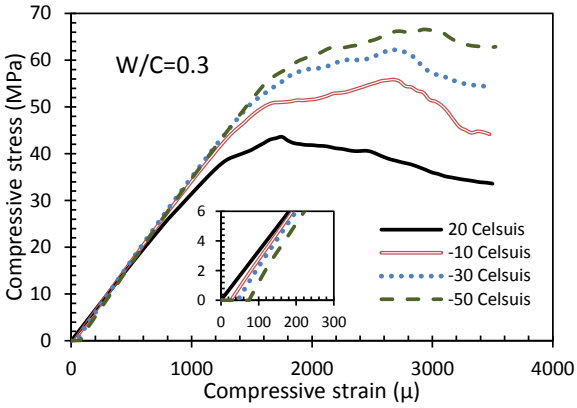

(a)

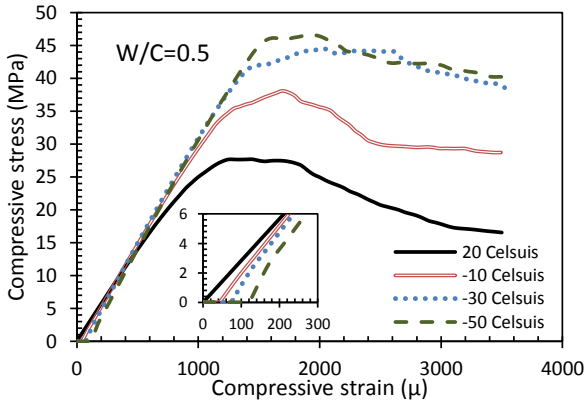

(b)

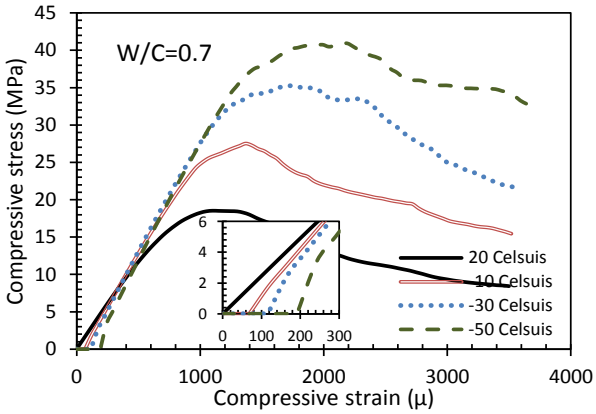

(c)

Fig. 6.14 Stress strain curve in compression at different temperatures (a) W/C=0.3 (b) W/C=0.5 (c) W/C=0.7

The increment of the compressive strength for each W/C ratio mainly comes from three aspects: (1) due to the increased elastic modulus in mortar, the tensile capacity of mortar and interface to have cracks becomes bigger so the concrete becomes more difficult to get the tensile cracks; (2) the shear capacity will increase once the elastic modulus increases according to Eq. (5.1); (3) the pre-stored shrinkage stress by pore pressures will postpone the tensile cracking and also enhance the shear capacity by reducing the total normal tensile stress. Since for the compression test with fix boundary condition in the horizontal direction, the shear failure of the springs will plays a rather crucial role than the tensile failure (Nagai et al., 2004), therefore the increment in tensile stiffness should be the main reason for the strength change.

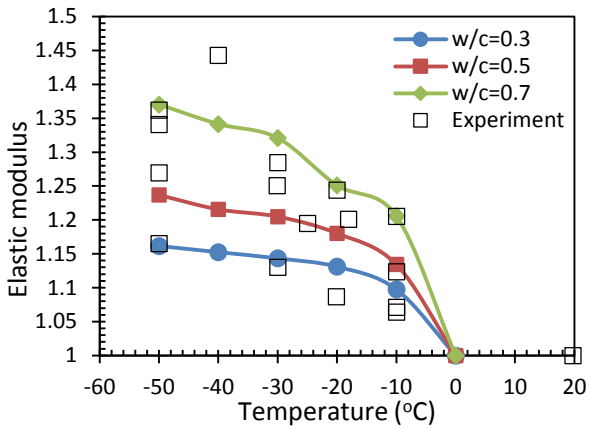

Fig. 6.15 The simulated elastic moduli and experiment data

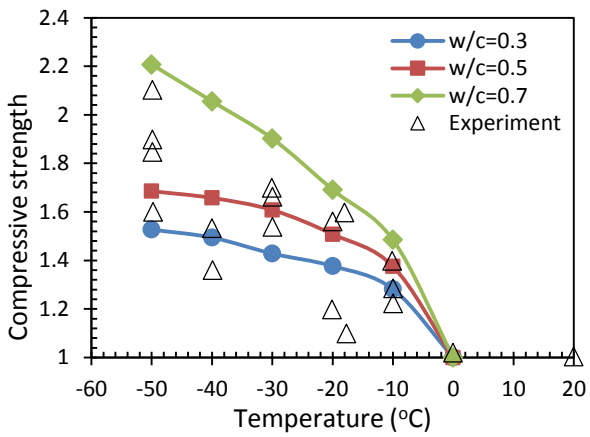

Fig. 6.16 Simulated and experimental compressive strength at freezing temperatures

The elastic modulus of specimens for different W/C ratio and temperatures are calculated according to ASTM C496, in which 0 to 40% of the ultimate compressive strength in the stress-strain curves in Fig. 6.14 will be used to determine the modulus of elasticity, as shown in Fig. 6.15. The change of compressive strength is also shown in Fig. 6.16 together with some experimental data. Since it is difficult to find a single literature which covers all the cases of mix proportion and testing temperatures, several groups of test date from different literatures are collected (Montejo et al., 2008) for the comparison purpose (Rostasy and Wiedemann, 1980; Lee et al., 1988a,b; Kasami et al., 1981; Marshall, 1982; Filiatrault and Holleran, 2001). In addition, in order to enhance the flexibility and applicability of the simulation model, the input material properties discussed in Section 5.2.2 are all coming from empirical estimation, which means the perfect agreement with each single test data may not be necessary while the overall range and tendency should be more important. Since the test data itself also has a large scatter. Therefore, in Fig. 6.15 and Fig. 6.16, the W/C=0.3 and W/C=0.7 curves can be regarded as two bounds of usual concrete material. For W/C=0.3, the void ratio of mortar (ϕ_m) is the smallest but the original elastic modulus (E_m) in room temperature are the biggest, then the normalized increment ($\Delta E/E$ and $\Delta f_c^{'}/ f_c^{'}$) of the concrete column will become the lowest. While for W/C=0.7, ϕ_m is the biggest but E_m is the smallest for the mortar, which will lead a highest normalized increment in elastic modulus and compressive strength for concrete. Finally, the W/C=0.5 can be regarded as an average case.

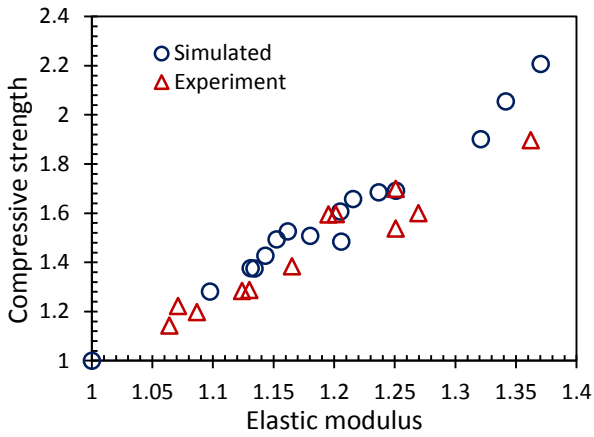

Fig. 6.17 Relation between compressive strength and elastic modulus at different temperatures

The relation between the relative increment in the compressive strength and elastic modulus is shown in Fig. 6.17, from which the simulated results matches the experimental data well. It can be seen that the compressive strength increases linearly to the elastic modulus, which means the ice formation has a synchronic effect on these two mechanical parameters.

6.2.3 Analysis of tension

Splitting tensile test

The simulation of splitting tensile test is conducted on the concrete cubic (Fig. 6.13 (b)), the material properties and the coarse aggregate ratio are same with the compression test in the previous section. It is difficult to draw the stress-strain curves for splitting test, and the load-displacement curves are usually used. But in order to make a direct comparison with the uniaxial tension test, the applied load has been converted to the splitting tensile stress by:

$$\sigma_s = \frac{2P}{\pi A} \tag{6.13}$$

where σ_s is the splitting tensile stress along the loading surface (MPa); P is the applied load (N); A is the area of the loading surface (mm^2) and in this 2D simulation, the unit thickness is assumed. Then the stress-displacement curves of all the W/C ratios are shown in Fig. 6.18. The basic characteristics among different W/C ratios and different temperatures are similar to the compression cases, such as the increment in effective elastic moduli and strengths, the pre-stored shrinkage due to the pore pressures and so on. The pre-stored shrinkage by pore pressures in Fig. 6.18 is not significant compared to the deformation from external load, which is same with the compression case. However, since the final failure in splitting test is mainly due to the tensile failure of the normal springs along the loading surface, the strengthened tensile strength and pre-stored uniform shrinkage stress are the two most important reasons for the macro-scale strength increment.

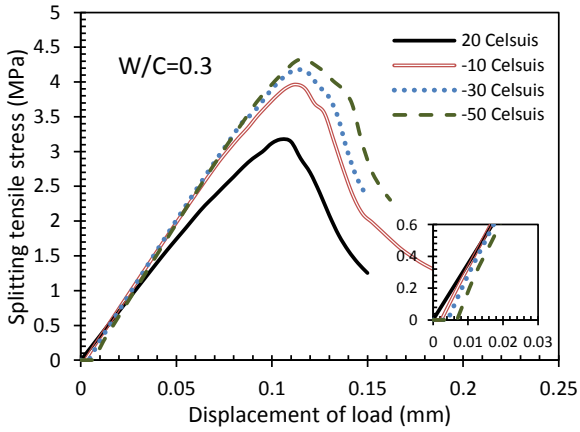

(a)

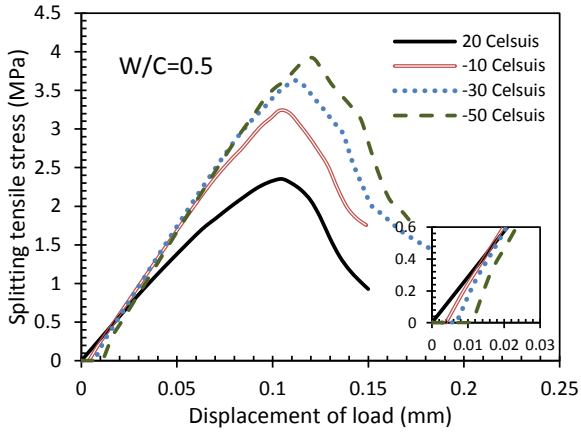

(b)

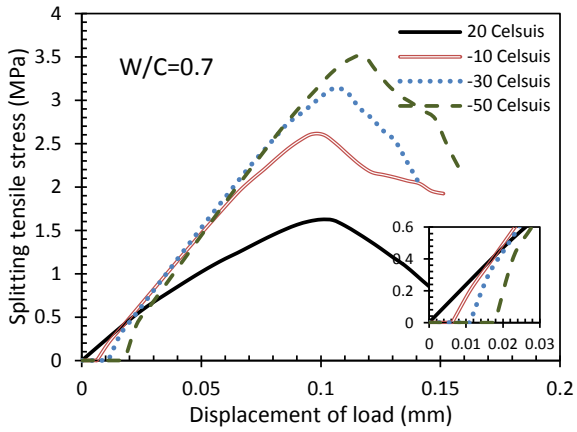

(c)

Fig. 6.18 Stress displacement curve in splitting at different temperatures (a) W/C=0.3 (b) W/C=0.5 (c) W/C=0.7

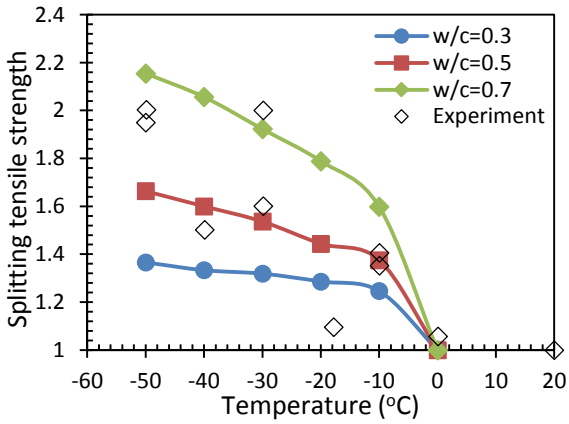

Fig. 6.19 Simulated and experimental splitting tensile strength at different temperatures

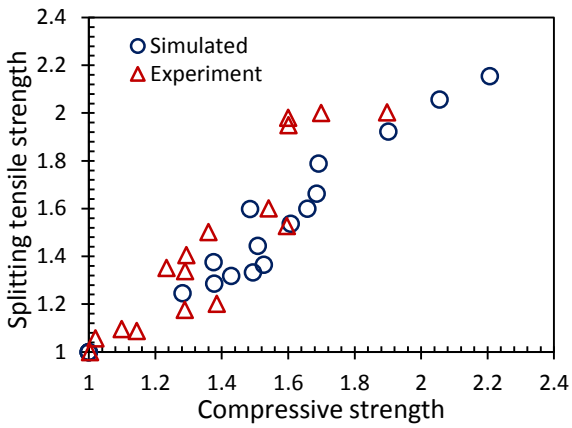

Fig. 6.20 Relation between splitting tensile strength and compressive strength

The simulated splitting tensile strengths of different cases are compared with collected previous test data, which can be seen in Fig. 6.19. The test data were summarized in Montejo et al. (2008), which were collected from Nasser and Evans (1973), Kasami et al. (1981) and Lee et al. (1988a). The simulated results agree with the test data well in the tendency and range, which can be a good prediction for the scattered test results. In addition, in order to eliminate the effect of scatter in the test data, the relative relation between compressive strength and splitting tensile strength of each specimen is compared in Fig. 6.20, and a better agreement can be seen. From both the experimental and simulated results, the compressive and splitting tensile strength have the synchronic change and the same magnitude.

Uniaxial tensile test

The uniaxial tensile tests have also been simulated, and the simulation model is same with the compression test (Fig. 6.13 (a)). Compared to the compression, the uniaxial tension suffers little effect from the shear stress, and its failure is mainly based on the normal springs in the vertical direction. Therefore, the increment in tensile strength and the pre-stored compressive pore pressure finally leads to the tensile strength increase in macro-scale. In addition, compared to the splitting tensile test, the displacement of load is equal to the average deformation in uniaxial tension test, which means the pre-stored shrinkage becomes more significant in the total deformation by external tension, as shown in Fig. 6.21. However, since the final tensile failure still depends on the normal springs along the tensile direction, the tensile strength should still be similar with the splitting cases. In Fig. 6.21, the strain at the tensile strength seems moving leftwards as temperature decreases, it is just because of significant shrinkage before loading, and if looking at the relative strain change from 0 to maximum tensile stress, the lower temperature still has a larger critical strain at tensile strength. Furthermore, the pre-store compressive pore pressures are uniform in the mortar part, and the material strength is randomly distributed (like the normal distribution in this simulation), therefore, in the uniaxial tension test, it could be possible that when the weakest layer starts to have cracks, the other part is still under shrinkage. Then when the material reaches its tensile capacity, the absolute deformation might still be shrinkage, such as the W/C=0.7 case at -50°C in Fig. 6.21.

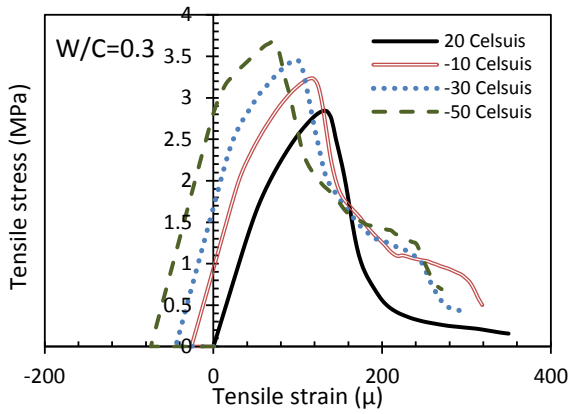

(a)

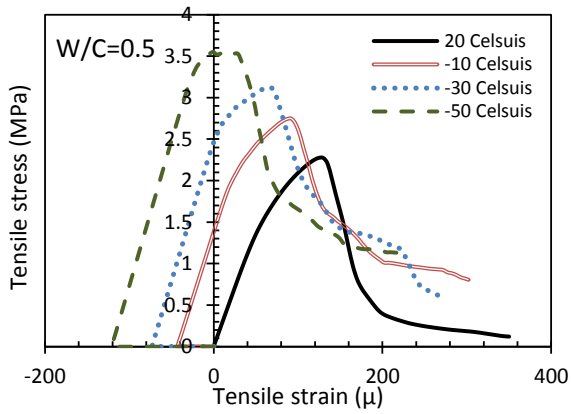

(b)

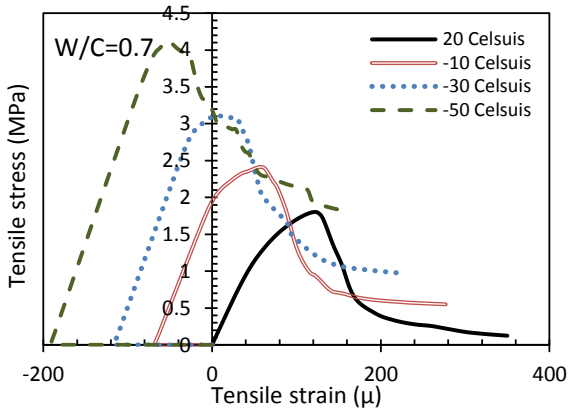

(c)

Fig. 6.21 Stress strain curve in uniaxial tension at different temperatures (a) W/C=0.3 (b) W/C=0.5 (c) W/C=0.7

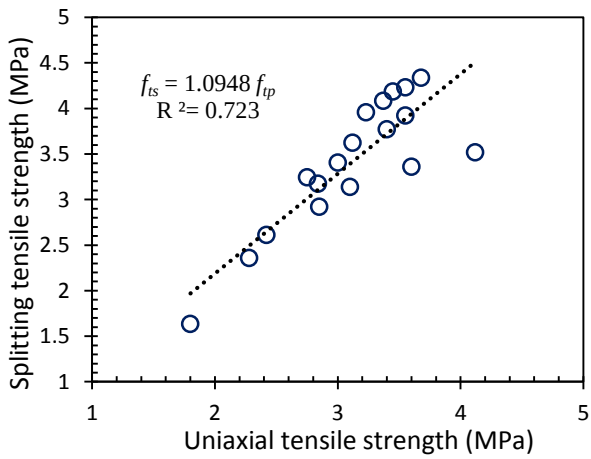

Fig. 6.22 Relation between the simulated splitting tensile strength and uniaxial tensile strength

Here since the previous experimental studies on the tensile strength are usually using the splitting tensile tests, therefore it is difficult to find direct experimental verifications to the simulated uniaxial tensile strengths. However, the simulated uniaxial strengths can be compared to the splitting strengths (which has already been verified above) as shown in Fig. 6.22. It can be seen that the tensile strengths

from splitting tests are in a good agreement with the uniaxial tests, the value is slightly higher (around 10%), this difference is also agree with the usual experience. Therefore, the simulated tensile strengths are reliable.

6.3 Fatigue loading with combination of FTC damage

The model and boundary condition for the fatigue tests and also the combined tests are shown in Fig. 6.23, in which the mortar cylinder will be used to verify the fatigue life that from the simplified fatigue constitutive laws without FTC damage, and compared with Matsumoto et al.'s (2010) simulation. Then the pure fatigue model will be extended from mortar to concrete, and the fatigue life of Fig. 6.23 (b) will be compared with previous experimental data. After verifying the pure fatigue simulation of mortar and concrete, the combined FTC and fatigue test will be simulated on the concrete cylinder. Table 6.3 shows the input material properties of the mortar concrete in this simulation, and also the simulated static compressive and tensile strengths of the undamaged mortar and concrete are shown in Fig. 6.24, which will be used as the references for the FTC damaged cases.

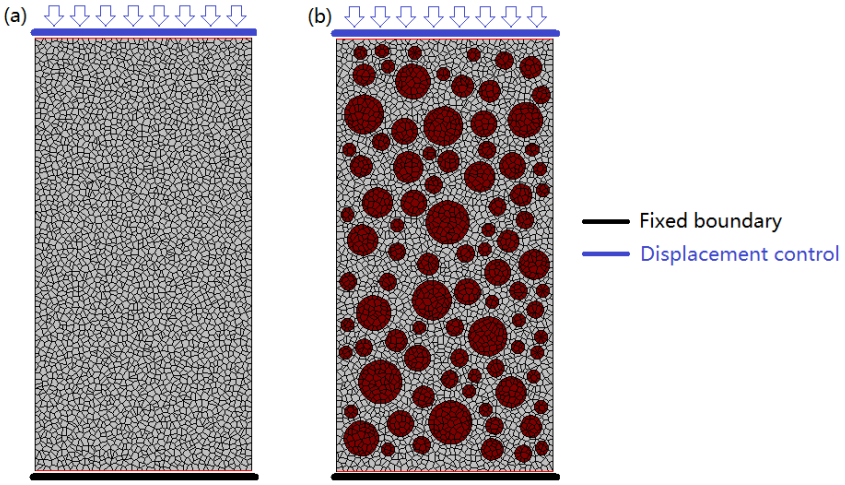

Fig. 6.23 The model and boundaries for fatigue test and combined test with FTC (a) mortar cylinder 200mm×100mm×100mm, 3278 elements; (b) concrete cylinder 200mm×100mm×100mm, 4251 elements

Table 6.3 The material properties in the fatigue simualtion

ID	w/c	f'_{cm} (MPa)	E_m (GPa)	f_{tp} (MPa)	c (MPa)	f_{ti} (MPa)	f_c (MPa)	f_t (MPa)
M1	0.5	31.91	21.164	3.35	-	-	30.96	3.326
C1	0.5	31.91	21.164	3.35	2.6	1.58	27.35	2.17

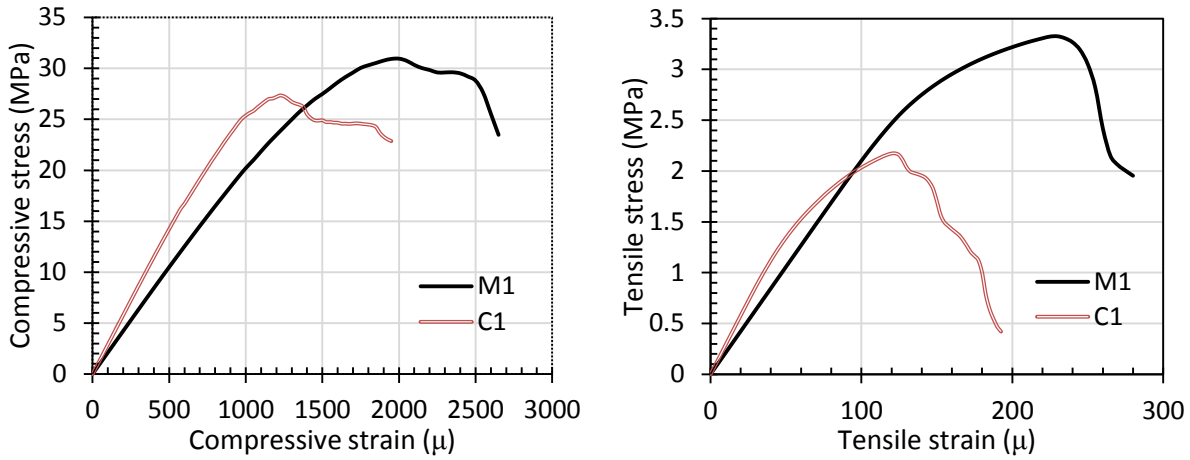

Fig. 6.24 The static strengths of mortar and concrete without FTC damage (Left: compressive. Right: uniaxial tensile)

6.3.1 The pure fatigue test

First, the pure fatigue tests are conducted on the mortar cylinder, with the same size and same input material properties as Matsumoto et al.'s simulations (2010). The globe strain history and the globe stress-strain curves in compressive and tensile fatigue are shown in Fig. 6.25. In which "C80" means the compressive stress level is 80% of the compressive strength, and also "T" means tension accordingly.

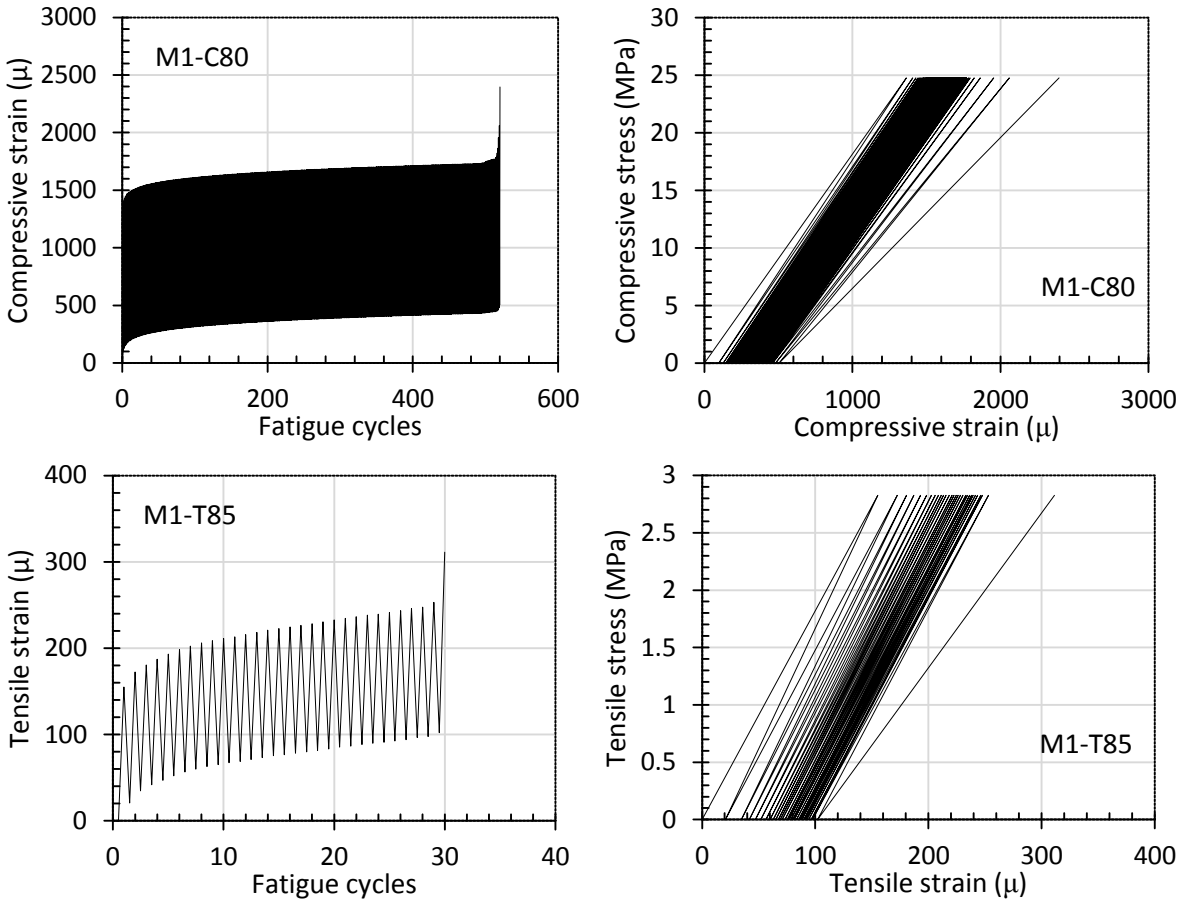

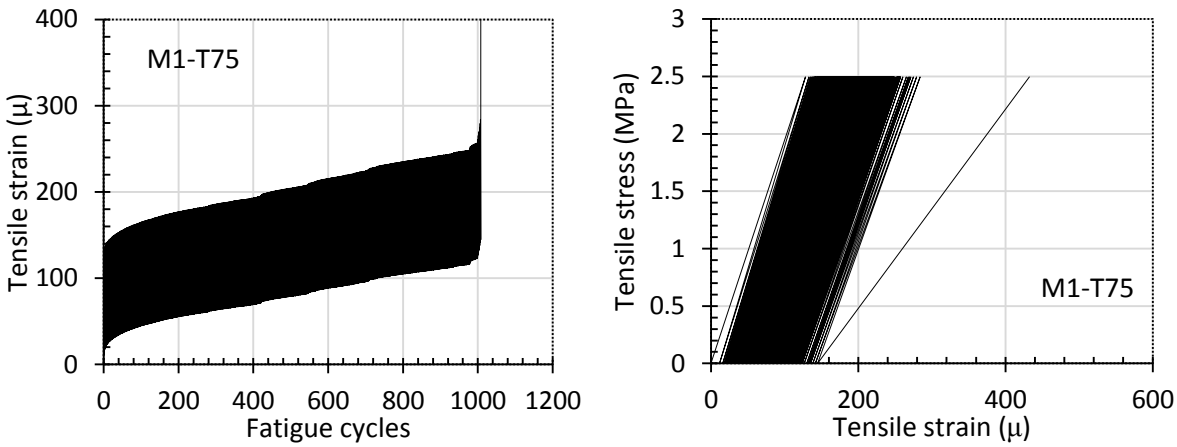

Fig. 6.25 The globe strain history and the globe stress-strain curves of the mortar in compressive and tensile fatigue

Several stress levels are selected to show the general characteristics of this simulation model. For the compressive fatigue on mortar, it can be seen that as the number of fatigue cycles increases, there is an increasing in the maximum strain and residual strain until it reaches the very end of its fatigue life. This is mainly due to creep effect rather than the damage. If just look at the mechanical model in this paper, the residual strain is only introduced to the normal spring for the tensile part. However, for the compressive failure of mortar with the boundaries fixed in the horizontal direction, the final failure is mainly controlled by the shear forces. Therefore, although the shear springs will cumulate the damage gradually during unloading and reloading, the residual deformation due to damage along the vertical axis will still not be obvious compared to the creep, until the very end of fatigue life, so the residual deformation is mainly because of the creep. On the contrary, the tensile failure is mainly depending on the normal spring, thus the gradual increasing maximum strain and residual strain contains both creep deformation and the crack opening. Nevertheless, damage cumulating and the fatigue life will mainly depend on tensile failure and shear failure, rather than the creep deformation.

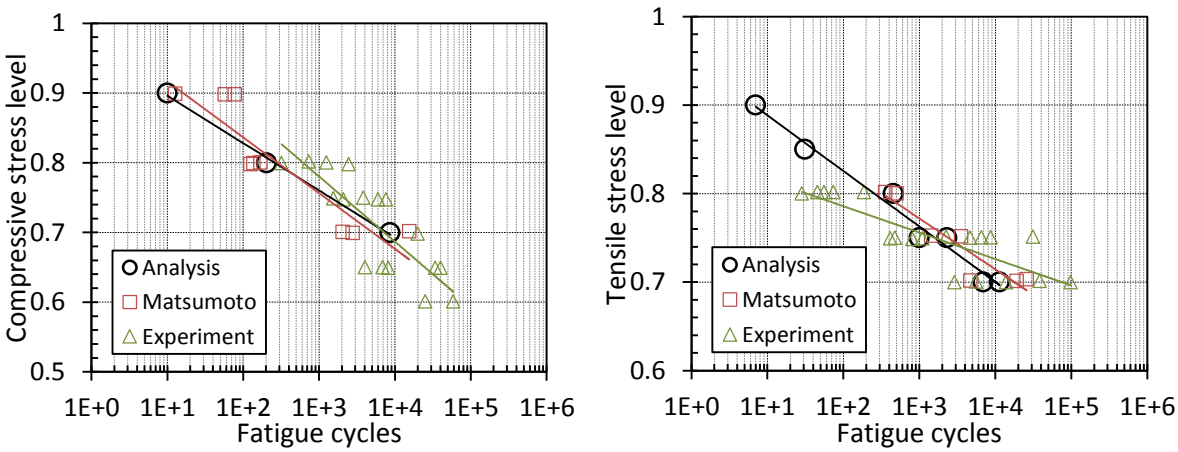

(a) (b)

Fig. 6.26 The S-N diagrams for the simplified time-independent model, with Matsumoto et al.'s analysis and Morris et al.'s data. (a) Compression; (b) Tension.

The fatigue life with different stress levels are shown in the S-N curve as presented in Fig. 6.26, and the simulation results are also compared with Matsumoto's analysis and Morris et al.'s (1981)

experimental data. It can be seen that the simulation results using the simplified model in this study agree with Matsumoto's results well, which means the time-dependent components, such as the creep, will not affect the fatigue life obviously. Thus the time-independent model proposed in this study can satisfy the accuracy but with much simpler calculating process. The simulation results also agree with the experimental data well.

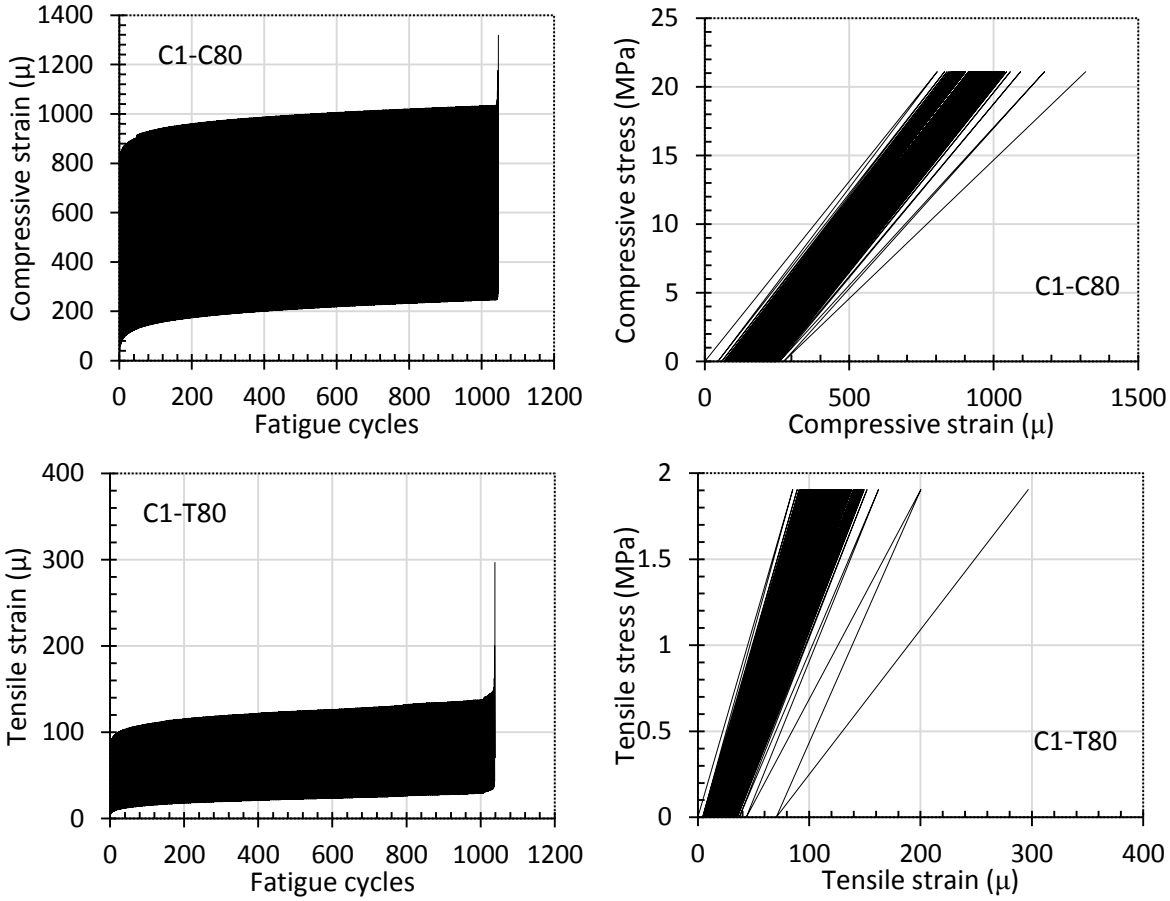

Fig. 6.27 The globe strain history and the globe stress-strain curves of the concrete in compressive and tensile fatigue

Then by introducing the similar degradation process to the mortar-aggregate interface, the fatigue failure of concrete can be simulated. In Fig. 6.27, several cases are shown with the strain development and the stress-strain curves. It can be seen that the for the compression failure, the cumulated residual deformation is still coming from the creep but with smaller values due to the existence of coarse aggregates. The tensile fatigue of concrete also becomes different compared to mortar, that is, although the increasing of the residual strain can be seen, the values are much smaller compared to pure mortar. This phenomenon is because that for the concrete under uniaxial tensile stresses, the mortar-aggregate interface will have cracks first, because it is much weaker that the mortar part. Therefore, during the most of the fatigue life, the damage cumulating will mainly occurs in the interfaces, meanwhile the mortar part may still stays within the elastic region. Then although the residual deformation at the interfaces can be very big, the global residual deformation may become much smaller. In addition, the confined effect of mortar part may also reduce the residual strain of the interfaces.

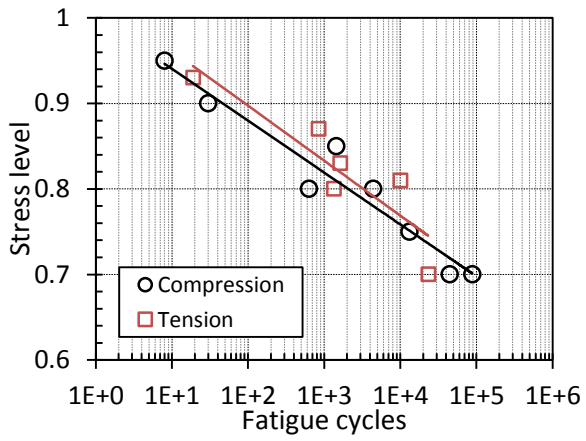

Fig. 6.28 The simulated S-N curves of compressive and tensile fatigue for concrete

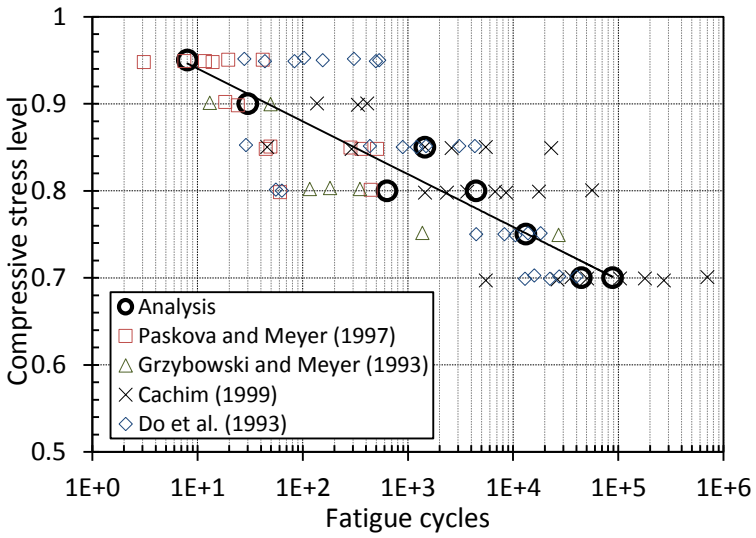

Fig. 6.29 Comparison between the simulated S-N curve for compressive fatigue and experimental data

The S-N curves of the compressive and tensile fatigue for concrete are simulated, which can be seen in Fig. 6.28. It can be seen at the two simulated S-N curves have similar shape and tendency, and the fatigue are within the same range. Since it is difficult to find some experimental data on the uniaxial tensile fatigue with load control, on only the previous data are collected from the compressive fatigue tests for the comparison purpose. The data are picked from Lee and Barr's review paper (2004), and the original data are coming from Paskova and Meyer (1997), Grzybowski and Meyer (1993), Cashim (1999) and Do et al. (1993), as shown in Fig. 6.29. Considering the big scatter in the fatigue experiments, the simulated S-N curve for concrete is within the range of previous data, and the slope of S-N curve is also in a good agreement with the average value of previous experiments.

6.3.2 Fatigue test on the FTC damaged concrete

In this section, the FTC test will be conducted first, with the increasing expansive internal stress, which is similar with the open test simulation in Section 6.1.3. Some typical FTC damage level are chosen to show the effect of FTC damage on the fatigue life, for example, 331μ, 730μ and 1795μ of residual deformation induced by FTC cycles. Before conducting the fatigue simulation, the static strengths of the FTC damage concrete should be simulated first, which is shown in Fig. 6.30. It can be seen that both the compressive and tensile strength will be reduced due to the micro cracks due to FTC

damage.

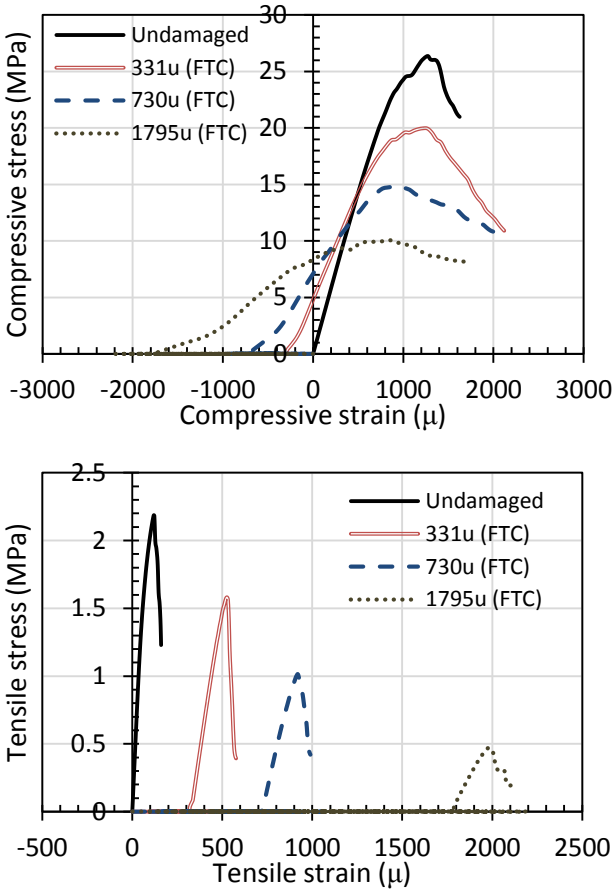

Fig. 6.30 The static compressive and tensile strengths of the FTC damaged concrete

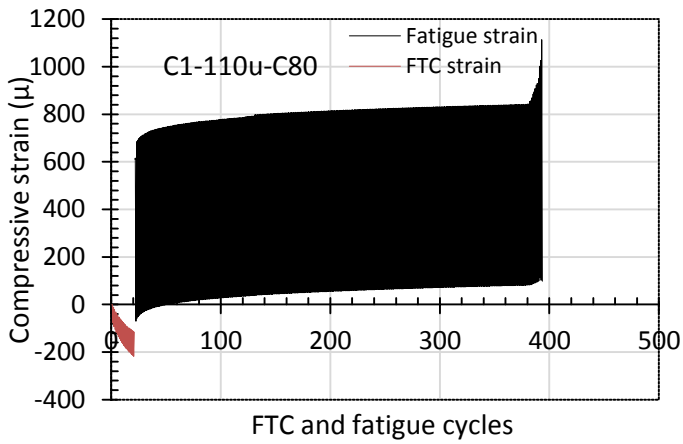

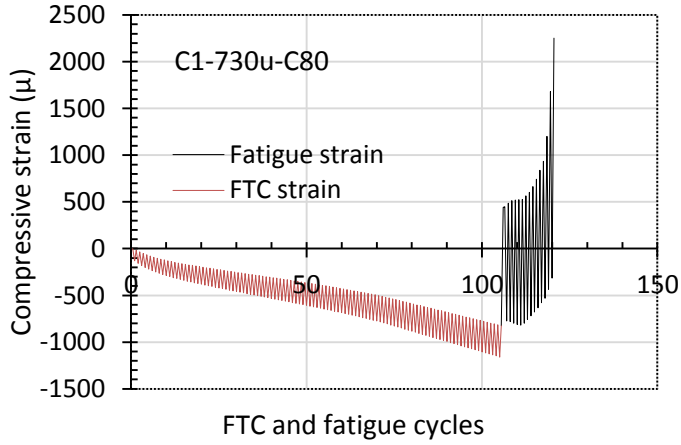

Fig. 6.31 The strain history under combined FTC and fatigue cycles

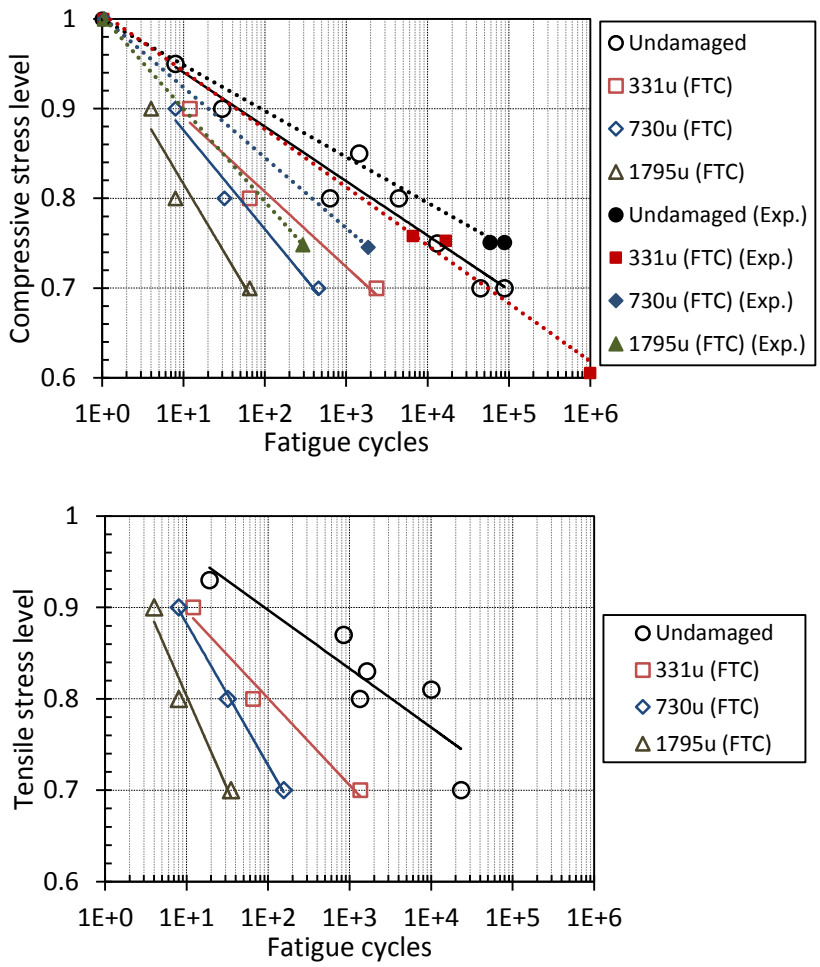

Fig. 6.32 S-N curves of compressive and tensile fatigue life for FTC damage concrete and undamaged concrete (experimental data of compressive fatigue comes from Hasan et al., 2008)

Fig. 6.31 show some examples of the strain development under the combined FTC and compressive fatigue cycles. The concrete cylinders with different residual strain of FTC damage are used and the stress level is 80%. It can be seen that the expansive freezing stress during FTC will cause continuously increasing expansion, which is reflected as negative compressive strain in Fig. 6.31. When FTC test

stops, there is a residual expansion (like 110μ and 730μ in all the directions), and this residual deformation must be recovered first when the compressive loading is applied from the top of the concrete cylinder. Therefore, the absolute deformation under fatigue loadings will be reduced. The S-N curves in Fig. 6.32 shows that the FTC damaged concrete will have a shorter fatigue life than the undamaged ones, although the static strengths have been adjusted accordingly (Fig. 6.30). This is because once expansive FTC damage is introduced before fatigue, most of the normal springs of mortar and interface will reach the softening part, then the damage cumulating during fatigue will becomes faster than undamaged concrete, therefore the fatigue life will becomes shorter. The simulated fatigue life of the compressive fatigue is compared with previous experimental data (Hasan et al., 2008), and it can be found that the tendency of the reduction in fatigue life as FTC damage increases are the same. Although the experimental data showed a systematically longer fatigue life than the usual experience.

6.4 Conclusions of this chapter

In this chapter, the simulations based on Rigid Body Spring Method (RBSM) are conducted for different freeze-thaw conditions and loading condition, from which the following conclusions are drawn:

(1) The mortar and mortar-aggregate interface are simulated under closed moisture condition with 30 freeze-thaw cycles while the concrete is simulated under open moisture condition with 300 cycles. The simulation results can show the damage cumulating, permeability change due to damage, the deformation behavior (reversing from expansion to contraction in closed test while continuously increasing in open test), crack pattern and width and so on, which agree with the experimental data well.

(2) The ice strengthened elastic modulus from the multi-phase composite model is adopted in the RBSM simulation, and the compressive, uniaxial tensile and splitting tensile tests are simulated and compared with the strength change in experiments, which also show a satisfactory agreement with the experimental data.

(3) The fatigue life simulated by the simplified time-independent model is compared with the one by the previous time-dependent model. The results show that although there are some differences in the strain development, the damage cumulating and fatigue life by the simplified model will not be affected significantly. And the fatigue simulation is extended from mortar to concrete which includes the effect of interface. The simulated concrete fatigue life matches previous experiments well.

(4) The FTC test (open moisture condition) is conducted first to obtain the internal micro cracking, then using the FTC damaged concrete, static test is simulated to obtain the residual strength while fatigue simulation is conducted to get the fatigue life. Both the residual strength and fatigue life show a significant reduction, which agrees with experimental observations well.

REFERENCES

Cachim, P. B. (1999). "Experimental and numerical analysis of the behaviour of structural concrete under fatigue loading with applications to concrete pavements."

Coussy, O., (2005). “Poromechanics of freezing materials.” *Journal of the Mechanics and Physics of Solids*, 53, 1689-1718.

Coussy, O. and Monteiro, P.J.M., (2009), “Errata to “Poroelastic model for concrete exposed to freezing temperatures” [Cement and Concrete Research 38 40-48]”, Cement and Concrete Research, 39, 371-

372.

Do, M.-T., Chaallal, O., and Aïtcin, P.-C. (1993). "Fatigue behavior of high-performance concrete." *Journal of Materials in civil Engineering*, 5(1), 96-111.

Fagerlund, G. (2002). "Mechanical damage and fatigue effects associated with freeze-thaw of materials." M. J. Setzer, R. Auberg and H. J. Keck. Eds. *Proc. 2nd International RILSM Workshop on Frost Resistant of Concrete*, Essen 18-19 April 2002. Cachan Cedex: RILEM Publications S.A.R.L., 117-132.

Filiatrault, A. and Holleran, M. (2001). "Stress-strain behavior of reinforcing steel and concrete under seismic strain rates and low temperatures." *Mater. Struct.*, 34 (5), 235-239.

Gong, F., Zhang, D., Sicat, E., and Ueda, T. (2014). "Empirical estimation of pore size distribution in cement, mortar, and concrete." *Journal of Materials in Civil Engineering*, 26(7).

Gong, F., Sicat, E., Zhang, D., and Ueda, T. (2015). "Stress Analysis for Concrete Materials under Multiple Freeze-Thaw Cycles." *Journal of Advanced Concrete Technology*, 13(3), 124-134.

Grzybowski, Miroslaw, and Christian Meyer. (1993). "Damage accumulation in concrete with and without fiber reinforcement." *ACI Materials Journal* 90.6 .

Hall, C., (1989). "Water sorptivity of mortar and concrete: A review." *Magazine of Concrete Research*, 41 (147), 51-61

Hasan, M., Okuyama, H., Sato, Y., and Ueda, T. (2004). "Stress-strain model of concrete damaged by freezing and thawing cycles." *Journal of Advanced Concrete Technology*, 2(1), 89-99.

Jacobsen, S., Gran, H. C., Sellevold, E. J., and Bakke, J. A., (1995). "High strength concrete-freeze/thaw testing and cracking." *Cem. Concr. Res.*, 25 (8), 1775–1780.

Jacobsen, S., Marchand, J., and Boisvert, L., (1996). "Effect of cracking and healing on chloride transport in OPC concrete." *Cem. Concr. Res.*, 26 (6), 869–881.

Jacobsen, S., Melandsø, F. and Nguyen, H. T., (2004) "Flow calculation and thermodynamics in wet frost exposure of cement based materials." *Proc., International RILEM Symposium on Concrete Science and Engineering: A Tribute to Arnon Bentur*, RILEM Publications SARL.

Lee, G., Shih, T., and Chang, K. (1988a). "Mechanical properties of concrete at low temperature." *Journal of cold regions engineering*, 2(1), 13-24.

Lee, G., Shih, T., and Chang, K. (1988b). "Mechanical properties of high-strength concrete at low temperature." *Journal of cold regions engineering*, 2(4), 169-178.

Lee, M., and Barr, B. (2004). "An overview of the fatigue behaviour of plain and fibre reinforced concrete." *Cement and Concrete Composites*, 26(4), 299-305.

Kasami, H., Tanaka, T., Kishima, Y. and Yamane, S. (1981). "Properties of concrete at very low temperatures." *Proc. 1st Int. Conf. on Cryogenic Concrete*. The Concrete Society, Newcastle Upon Tyne, London, 123-134.

Marshall, A.L. (1982). "Cryogenic concrete" *Cryogenics*, 22 (11), 555-565.

Matsumoto, K., Sato, Y., and Ueda, T. (2010). "Fracture mechanism and predition of deforamtion of mortar under time-dependent loads by meso-scale analysis." *Doboku Gakkai Ronbunshuu E/JSCE Journal of Materials, Concrete Structures and Pavements*, 66(4), 380-398. (In Japanese)

Montejo, L. A., Sloan, J. E., Kowalsky, M. J., and Hassan, T. (2008). "Cyclic response of reinforced concrete members at low temperatures." *Journal of Cold Regions Engineering*, 22(3), 79-102.

Morris, A., and Garrett, G. (1981). "A comparative study of the static and fatigue behaviour of plain and steel fibre reinforced mortar in compression and direct tension." *International Journal of Cement Composites and Lightweight Concrete*, 3(2), 73-91.

Nagai, K., Sato, Y., and Ueda, T. (2004). "Mesoscopic simulation of failure of mortar and concrete by 2D RBSM." *Journal of Advanced Concrete Technology*, 2(3), 359-374.

Nasser, K.W. and Evans, G.A. (1973). “Low temperature effects on hardened air entrained concrete.” *Behavior of concrete under temperature extremes*, ACI SP-39, 79-90.

Paskova, T., and Meyer, C. (1997). "Low-cycle fatigue of plain and fiber-reinforced concrete." *ACI Materials Journal*, 94(4).

Powers, T. C. (1949). "A working hypothesis for further studies of frost resistance of concrete." *Proc., ACI journal Proceedings*, ACI.

Rostasy, F., and Wiedemann, G. (1980). "Stress-strain-behaviour of concrete at extremely low temperature." *Cement and Concrete Research*, 10(4), 565-572.

Sicat, E., Gong, F., Zhang, D. and Ueda, T., (2013). “Change of the coefficient of thermal expansion of mortar due to damage by freeze thaw cycles.” *Journal of Advanced Concrete Technology*, 11, 333-346.

Sicat, E., Gong, F., Ueda, T. and Zhang D., (2014). “Experimental investigation of the deformational behavior of the interfacial transition zone (ITZ) of mortar during freezing and thawing cycles.” *Construction and Building Materials*, 65, 122-131.

Sun, Z. and Scherer, G.W. (2010), “Effect of air voids on salt scaling and internal freezing.” Cement and Concrete Research, 40, 260-270.

Yang, Z., Weiss, W.J. and Olek, J. (2006), “Water transport in concrete damaged by tensile loading and freeze-thaw cycling.” Journal of Materials in Civil Engineering, Vol. 18, No. 3, 424-434.

CHAPTER 7

7. Conclusions

The modeling and simulation of the frost damage problem, as well as the combined issues with external static and fatigue loadings are presented in this dissertation, the main conclusions of each chapter are summarized, and also the remaining tasks are discussed at last.

(1) The phase equilibrium of the moisture inside the concrete material has been discussed. Based on the thermodynamic theories, the chemical potential is introduced to determine the moisture phase transformation, which mainly depends on the relative humidity, temperature and the pore size. A 3D phase diagram is also presented to give a clearer image of the moisture condition in different size of pores under different environmental condition. Not only restricted to the cement-based materials, this tool can also be applied to all kinds of porous materials. In addition, it has been found that the total moisture content, which includes both liquid and vapor phase is mainly controlled by the relative humidity. While how much of this liquid water would turn into ice is mainly determined by the temperature. So the numerical program for this problem can be improved by reducing insignificant parameters to achieve a better balance between efficiency and accuracy. Finally the amount of ice formation, unfrozen water and dry pores can be estimated quantitatively.

(2) Based on the most well-accepted frost damage mechanisms, a more comprehensive hydraulic model is proposed. The poromechanical rules and Darcy's law are combined to calculate the hydraulic pressure, which becomes a half static and half dynamic force. The hydraulic pressure is closely depending on the permeability of the material, and might decrease gradually at the number of freeze thaw cycles increases. The total pressure is the combination of three pressures (hydraulic, crystallization and cryosuction), which will be positive at the beginning but convert to be negative later. This mechanism explains the reverse phenomenon (expansion during first few freeze-thaw cycles but converted to contraction in the following freeze-thaw cycles) of the strain during test with closed moisture condition. Poroelastic relation is assumed to estimate the strain based on the calculated total pressure, and the estimated strain is in good agreement with experiment data. In addition, the effect of the main parameters on the calculated results is also discussed. The saturation degree plays a crucial role in the super high saturation region (higher than 96%), which makes the reverse phenomenon only happens in test with closed moisture condition but not in open condition. And at last, the permeability change is a result of frost damage, but at the same time, the increased permeability will help to reduce the stress level, and finally the system will achieve an equilibrium steady state.

(3) A multi-phase composite model is proposed to estimate the macro mechanical properties of concrete material with the ice strengthening effect in which the stress concentration in pores with different phases of moisture can be taken into consideration. Based on the existing two-phase theories and the concept of composition, the freezing concrete, which is a four-phase composite, can be composed step by step by a series of two-phase problems. And by regressing of the previous data of dry and water saturated concrete, the proper value for the aspect ratio of pores with different phases of moisture can be determined. In addition, using the proposed model, the effective elastic moduli due to ice strengthening effect at different temperatures can be predicted, which are also in

a good agreement with experimental data. Therefore, the predicted elastic property change is reliable for the Rigid Body Spring Method (RBSM) simulation of the static strengths.

(4) The constitutive laws of deformation under pure freeze-thaw cycles (FTC) is developed. The nature of the internal effective stress (an average stress on the porous matrix caused by pore pressures) as well as the deformation compatibility between ice-water and pore structure can be conveniently described by a parallel spring model, and the constitutive laws for each spring is discussed. This parallel system can adjust the applied stress on the spring of porous body automatically if the strain changes. In addition, the strengthening effect by ice can be also taken into consideration. The transformation of internal effective stress to an equivalent external stress makes the numerical simulation much simpler.

(5) The ice strengthening effect under external loadings at low temperatures can be reflected by the increasing in the input stiffness in the mesoscale simulation. Since the critical strain at the tensile strength does not change, the actual tensile strength will also increase proportionally to the stiffness due to the strengthening effect.

(6) The constitutive laws under fatigue loading is also modified. In order to make the stress-strain relations of each spring much simpler, the previous model is simplified into a time-independent model which only focus on the final damage under fatigue loadings. And also the stress drop is introduced to mortar-aggregate interface similarly as pure mortar in previous studies, then by doing so, the fatigue simulation to concrete becomes possible.

(7) Finally in the mesoscale simulation using RBSM, several FTC and loading conditions are studied:
   a) Pure FTC for mortar and concrete: The mortar and mortar-aggregate interface are simulated under closed moisture condition with 30 cycles while the concrete is simulated under open moisture condition with 300 cycles. The simulation results can show the damage cumulating, permeability change due to damage, the deformation behavior (reversing from expansion to contraction in closed test while continuously increasing in open test), crack pattern and width, which agree with the experimental data well.
   b) Static loading for concrete with ice strengthening effect at low temperatures: The ice strengthened elastic modulus from the multi-phase composite model is adopted in the RBSM simulation, and the compressive, uniaxial tensile and splitting tensile tests are simulated and compared with the strength change in experiments, which also show a satisfactory agreement.
   c) Pure fatigue test for mortar and concrete: The fatigue life predicted by the simplified time-independent model is compared with the one by the previous time-dependent model (in which the creep is also considered in the constitutive law). And the fatigue simulation is extended from mortar to concrete which indicates the effect of interface. The simulated concrete fatigue life matches previous experiments well.
   d) Fatigue test for concrete with different level of FTC damage: In which the FTC test (open moisture condition) is conducted first to obtain the internal micro cracking, then using the FTC damaged concrete, static test is simulated to obtain the residual strength while fatigue simulation is conducted to get the fatigue life. Both the residual strength and fatigue life show a significant reduction, which agree with experimental observations well.

The remaining tasks

a) In Chapter 2, the thermodynamic model in this study is still an ideal one, in which the shape of pores has not been considered. For example, the large pore may have small entry, which makes the freezing point different. But it can be solved by introducing the pore shape information in this study, which will be done in the future study.
b) In Chapter 3, the relationship between stress level and permeability revealed by this model can also provide a possible way to evaluate the durability problem under a given environmental condition. That is, after a certain number of freeze thaw cycles, we can estimate the permeability according to the strain behavior (whether expansion or contraction, and also the magnitude of deformation) during that cycle. This quick method is convenient, based on the same specimen, and the permeability can be tracked during the entire test. But the reliability needs further investigation (for example, by comparing with direct permeability measurements), which will be conducted in the further work.
c) In Chapter 5, the static simulation at low temperatures analyzed at this moment has only considered the negative pore pressure due to cryosuction (when the saturation degree is not very high or there is no continuously water supply) as the pre-stress condition, so the pre-stress will not reach the tension softening part of the normal springs. However, if the pre-stress becomes the destructive expansive stress due to positive hydraulic pressure (when the saturation degree is very high and water is continuously supplied), the material will become very weak under external tensile loads, and the experimental evidences under this condition are also limited. Therefore, it is useful to study this point both experimentally and numerically in the future studies.
d) In Chapter 6, another kind of combined effect of FTC damage and fatigue is that suffering them simultaneously together. Although previous studies showed less damage than single fatigue, but that might be because there was no continuous water supply. Therefore, the simultaneous experiments as well as the mesoscale analysis should be conducted in the future studies.